

THESIS ON NATURAL AND EXACT SCIENCES B152

# **Magnetic Properties of Functional Oxides**

HIMANI KHANDURI

**TUT**  
PRESS

TALLINN UNIVERSITY OF TECHNOLOGY  
Faculty of Science  
Department of Physics

**This dissertation was accepted for the defence of the degree of Doctor of Philosophy (in Applied Physics) on April 8, 2013.**

**Supervisors:** Dr. Raivo Stern, senior research scientist,  
National Institute of Chemical Physics and Biophysics, Estonia

Professor Jüri Krustok, Department of Physics,  
Faculty of Science, Tallinn University of Technology, Estonia

**Opponents:** Dr. Arlette Trokiner, ESPCI, Paris, France

Dr. Aile Tamm, Institute of Physics,  
Faculty of Science and Technology, University of Tartu

**Defence of the thesis:** June 5, 2013

Declaration:

*Hereby I declare that this doctoral thesis, my original investigation and achievement, submitted for the doctoral degree at Tallinn University of Technology has not been submitted for any academic degree.*

/Himani Khanduri/



European Union  
European Social Fund



Investing in your future

Copyright: Himani Khanduri, 2013  
ISSN 1406-4723  
ISBN 978-9949-23-463-9 (publication)  
ISBN 978-9949-23-464-6 (PDF)

LOODUS- JA TÄPPISTEADUSED B152

# **Funktsionaalsete oksiidide magnetilised omadused**

HIMANI KHANDURI



# CONTENTS

LIST OF ORIGINAL PUBLICATIONS.....	8
LIST OF CONFERENCE PRESENTATIONS.....	10
INTRODUCTION.....	12
ABBREVIATIONS.....	14
1. LITERATURE REVIEW.....	15
1.1. Magnetic Materials.....	15
1.1.1. Magnetic quantities and Units.....	15
1.1.2. Classes of Magnetic Materials.....	16
1.1.2.1. Diamagnetism.....	17
1.1.2.2. Paramagnetism.....	17
1.1.2.3. Ferromagnetism.....	19
1.1.2.4. Antiferromagnetism.....	20
1.1.2.5. Ferrimagnetism.....	21
1.2. Ferrites.....	22
1.2.1. Hexagonal ferrites.....	23
1.2.1.1. Structural Properties.....	24
1.2.1.2. Magnetic Properties.....	26
(i) Magnetism in hexagonal ferrites.....	26
(ii) Magnetic moments and superexchange in hexagonal ferrites.....	27
(iii) Grain size dependence of magnetic properties of hexagonal ferrites.....	28
1.2.2. Y-type hexaferrite ( $Ba_2Me_2Fe_{12}O_{22}$ ).....	29
1.2.2.1. Structural Properties.....	29
1.2.2.2. Magnetic Properties.....	30
1.2.2.3. Substituted Y ferrites.....	31
1.3. Ferromagnetism in non - magnetic zirconium dioxide by transition metal and non-magnetic dopants.....	33
1.3.1. Zirconia.....	33
1.3.2. Crystal structure.....	34
1.3.2.1. Cubic Phase.....	34
1.3.2.2. Tetragonal Phase.....	34
1.3.2.3. Monoclinic Phase.....	35
1.3.2.4. Phase stabilization.....	36
1.3.3. Magnetism in non magnetic oxides.....	36
1.4. Perovskite Manganites.....	37
1.4.1. Lanthanum Manganite.....	39
1.4.1.1. $LaMnO_3$ Electronic Structure (Jahn-Teller effect).....	39
1.4.1.2. Double Exchange.....	40
1.4.1.3. Superexchange Interaction.....	42
1.4.1.4. Crystal Structure.....	43
1.4.1.5. Electronic Transport.....	44
1.4.1.6. Magnetic Properties.....	45

1.4.1.7. Colossal Magnetoresistance (CMR).....	47
2. AIMS OF THE STUDY.....	48
3. EXPERIMENTAL.....	49
3.1. Synthesis of samples.....	49
3.1.1. Polycrystalline powder samples of Y-type ( $\text{Ba}_{2-x}\text{Sr}_x\text{Mg}_2\text{Fe}_{12}\text{O}_{22}$ ) hexaferrites.....	49
3.1.2.1. Polycrystalline powder samples of $\text{Zr}_{1-x}\text{Ca}_x\text{O}_2$ and $\text{Zr}_{0.86}\text{Mg}_{0.14}\text{O}_2$ .....	49
3.1.2.2. $\text{Zr}_{1-x}\text{Ca}_x\text{O}_2$ thin films prepared by pulsed laser deposition.....	49
3.1.3.1. $\text{LaMnO}_3$ thin films prepared by atomic layer deposition.....	50
3.1.3.2. Polycrystalline powder samples of $\text{LaMnO}_3$ .....	50
3.2. Characterization techniques.....	51
3.2.1. X-ray diffraction.....	51
3.2.2. Raman spectroscopy.....	51
3.2.3. SEM micrographs and EDX spectra.....	51
3.2.4. Magnetic measurements.....	51
3.2.5. NMR measurements.....	52
3.2.6. Dielectric measurements.....	52
3.2.7. Atomic force microscopy (AFM) and magnetic force microscopy (MFM).....	52
4. RESULTS AND DISCUSSION.....	53
4.1. Structural and Microstructural Studies.....	53
4.1.1. Phase identification of Y-type $\text{Ba}_{2-x}\text{Sr}_x\text{Mg}_2\text{Fe}_{12}\text{O}_{22}$ samples.....	53
4.1.2. Phase identification of $\text{Zr}_{1-x}\text{Ca}_x\text{O}_2$ ( $x = 0$ and $0.16$ ) and $\text{Zr}_{0.86}\text{Mg}_{0.14}\text{O}_2$ samples.....	55
4.1.3.1. Phase identification of $\text{LaMnO}_3$ samples.....	58
4.1.3.2. AFM Studies of $\text{LaMnO}_3$ thin films.....	62
4.2. Magnetic Studies.....	63
4.2.1.1. Magnetic properties of Y-type $\text{Ba}_{2-x}\text{Sr}_x\text{Mg}_2\text{Fe}_{12}\text{O}_{22}$ samples.....	63
4.2.1.2. NMR measurements on $\text{Ba}_2\text{Mg}_2\text{Fe}_{12}\text{O}_{22}$ .....	67
4.2.2. Magnetic properties of $\text{Zr}_{1-x}\text{Ca}_x\text{O}_2$ ( $x = 0$ and $0.16$ ) and $\text{Zr}_{0.86}\text{Mg}_{0.14}\text{O}_2$ samples.....	68
4.2.3.1. Magnetic properties of $\text{LaMnO}_3$ samples.....	72
4.2.3.2. MFM Studies of $\text{LaMnO}_3$ thin films.....	77
4.3. Dielectric Studies of Y-type $\text{Ba}_{2-x}\text{Sr}_x\text{Mg}_2\text{Fe}_{12}\text{O}_{22}$ samples.....	78
5. CONCLUSIONS.....	80
REFERENCES.....	82
ACKNOWLEDGMENTS.....	89
ABSTRACT.....	90
KOKKUVÕTE.....	91
CURRICULUM VITAE.....	92
ELULOOKIRJELDUS.....	94
APPENDIX.....	95
PUBLICATION I.....	97

PUBLICATION II.....	107
PUBLICATION III.....	117
DISSERTATIONS DEFENDED.....	127

## LIST OF ORIGINAL PUBLICATIONS

This thesis is based on the following original publications referred to by their Roman numerals in the text and these publications are reproduced in the appendix with permission from the publishers.

- I **Khanduri, H.**; Dimri, M. Chandra; Kooskora, H.; Heinmaa, I.; Viola, G.; Ning, H.; Reece, M. J.; Krustok, J.; Stern, R. 2012. Structural, dielectric, magnetic, and nuclear magnetic resonance studies of multiferroic Y-type hexaferrites. *J. Appl. Phys.* 112, 073903.
- II Dimri, M. Chandra; **Khanduri, H.**; Kooskora, H.; Kodu, M.; Jaaniso, R.; Heinmaa, I.; Mere, A.; Krustok, J.; Stern, R. 2012. Room-temperature ferromagnetism in Ca and Mg stabilized cubic zirconia bulk samples and thin films prepared by pulsed laser deposition. *J. Phys. D: Appl. Phys.* 45, 475003.
- III **Khanduri, H.**; Dimri, M. Chandra; Vasala, S.; Leinberg, S.; Lohmus, R.; Ashworth, T. V.; Mere, A.; Krustok, J.; Karppinen, M.; Stern, R. 2013. Magnetic and structural studies of LaMnO<sub>3</sub> thin films prepared by atomic layer deposition. *J. Phys. D: Appl. Phys.* 46, 175003.

## ADDITIONAL PUBLICATIONS

- IV Dimri, M. Chandra; **Khanduri, H.**; Kooskora, H.; Subbi, J.; Heinmaa, I.; Mere, A.; Krustok, J.; Stern, R. 2012. Ferromagnetism in rare earth doped cerium oxide bulk samples. *Phys. Status Solidi A* 209, 353–358.
- V Dimri, M. Chandra; **Khanduri, H.**; Kooskora, H.; Heinmaa, I.; Joon, E.; Stern, R. 2011. Magnetic properties and <sup>57</sup>Fe NMR studies of U-type hexaferrites. *Journal of Magnetism and Magnetic Materials*, 323, 2210 - 2213.
- VI Pore, V.; Dimri, M.; **Khanduri, H.**; Stern, R.; Lu, J.; Hultman, L.; Kukli, K.; Ritala, M.; Leskelä, M. 2011. Atomic layer deposition of ferromagnetic cobalt doped titanium oxide thin films. *Thin Solid Films*, 519, 3318 - 3324.

## AUTHOR'S CONTRIBUTION TO THE PUBLICATIONS

- I In the 1st publication, the author synthesized various samples, performed experiments and analyzed the results. She interpreted the data and prepared the manuscript.

- II** The author performed Raman and magnetic measurements and helped in the synthesis of samples. She also participated in data analysis and writing the respective part of manuscript.
  
- III** The author was responsible for the study design and synthesis of the various LMO thin films by ALD method. She performed structural and magnetic measurements and responsible for the preparation of the manuscript.

## LIST OF CONFERENCE PRESENTATIONS

- I. **Khanduri, H.**; Dimri, M. Chandra; Mere, A.; Mikli, V.; Krustok, J.; Stern, R. **Magnetic, structural and magneto-resistance studies of doped LaMnO<sub>3</sub> bulk samples prepared by citrate combustion process.**  
Poster presentation at the APS March Meeting, March 2013, Baltimore, USA.
- II. Dimri M.; **Khanduri H.**; Vasala S.; Leinberg S.; Lohmus R.; Krustok J.; Karppinen M. and Stern R. **Structural, AFM, MFM and magnetic studies of LaMnO<sub>3</sub> thin films prepared by atomic layer deposition method.**  
Oral presentation at the APS March Meeting, March 2013, Baltimore, USA.
- III. Dimri, M. Chandra; **Khanduri, H.**; Mere, A.; Stern, R. **Magnetic studies on spinel ferrite nanoparticles synthesized by citrate combustion route.**  
Poster presentation at the 13th International Conference on Magnetic Fluids (ICMF-13), January 2013, New Delhi, India.
- IV. **Khanduri, H.**; Dimri, M. Chandra; Kooskora, H.; Heinmaa, I.; Viola, G.; Ning, H.; Reece, M. J.; Krustok, J.; Stern, R. **Magnetic and dielectric studies of multiferroic Y – type hexaferrites.**  
Poster presentation at the 4<sup>th</sup> WUN International Conference on Spintronics (WUN-SPIN 2012), July 2012, Sydney, Australia.
- V. Dimri, M. Chandra; **Khanduri, H.**; Kooskora, H.; Kodu, M.; Jaaniso, R.; Heinmaa, I.; Mere, A.; Krustok, J.; Stern, R. **Room temperature ferromagnetism in Ca and Mg stabilized cubic zirconia bulk samples and their thin films.**  
Oral presentation at the 4<sup>th</sup> WUN International Conference on Spintronics, (WUN-SPIN 2012), July 2012, Sydney, Australia.
- VI. **Khanduri, H.**; Dimri, M. Chandra; Kooskora, H.; Krustok, J.; Mare, A.; Stern, R. **Structural and magnetic studies on spinel ferrite nanoparticles.**  
Poster presented at the International Conference on Nanomaterials and Nanotechnology, (ICNANO 2011). December 2011, Delhi, India.
- VII. Chandra, M.; **Khanduri, H.**; Kooskora, H.; Stern, R. **Room temperature ferromagnetism in nano and bulk powders of Mn doped zirconia.**  
Poster presented at the International Conference on Nanomaterials and

Nanotechnology, (ICNANO 2011), December 2011, Delhi, India.

- VIII. Khanduri, H.;** Dimri, M. Chandra; Kooskora, H.; Heinmaa, I.; Krustok, J.; Stern, R. **Magnetic and NMR studies on multiferroic Y-type hexaferrites.**

Poster presented at ECerS XII, the 12th Conference of the European Ceramic Society, June 2011, Stockholm, Sweden.

- IX.** Dimri, M. Chandra; **Khanduri, H.;** Kooskora, H.; Joon, E.; Heinmaa, I.; Stern R. **Magnetic properties and  $^{57}\text{Fe}$  NMR studies on U-type hexaferrites.**

Poster presented at ECerS XII, the 12th Conference of the European Ceramic Society, June 2011, Stockholm, Sweden.

## INTRODUCTION

Magnetic materials and devices have a very important role in our daily life. Magnetism was probably the first natural force discovered by man, but it has only been applied widely in the last century. The emergence of many new devices/technologies driven by differing requirements, in turn, has led to a large variety of magnetic materials produced in many different geometries, shapes and sizes (Goldman, 2006).

Magnetic oxides are fascinating materials scientifically as well as technologically due to their multifunctionality. The use of magnetic oxides in electronics technology has become so common that few systems can operate effectively without some form of them making a vital contribution. Magnetic materials are components of many electromechanical and electronic devices. They are also used as components in a wide range of industrial and medical equipment. Permanent magnet materials are essential in devices for storing energy in a static magnetic field. Major applications involve the conversion of mechanical to electrical energy and vice versa, or the exertion of a force on soft ferromagnetic objects. The applications of magnetic materials in information technology are continuously growing since the last few decades. The frequencies of application of magnetic materials range from DC (Direct Current) to the highest ones at which any electronic device can function (Buschow and Boer, 2004).

Recently some of these materials, especially the perovskites ( $\text{RMnO}_3$ , where R is a rare earth element) and hexaferrites have gained large importance due to the discovery of colossal magnetoresistance (CMR) and multiferroicity (magnetoelectricity) in them, respectively. Magnetoelectric phenomena that jointly involve the magnetic and electrical conductivity properties have been discovered in some oxides/ferrites (such as, Y- and Z-type hexaferrites, etc.) those contain magnetic ions. Ferroelectricity in a Y – type hexaferrite system ( $\text{Ba}_{0.5}\text{Sr}_{1.5}\text{Zn}_2\text{Fe}_{12}\text{O}_{22}$ ) was first reported by Kimura *et al.* (Kimura *et al.*, 2005). At ambient conditions and zero magnetic field,  $\text{Ba}_{0.5}\text{Sr}_{1.5}\text{Zn}_2\text{Fe}_{12}\text{O}_{22}$  is a nonferroelectric insulator with noncollinear spin arrangement. In an applied magnetic field it undergoes several phase transitions and some of the phases exhibit ferroelectricity induced by a critical magnetic field of 0.3 – 0.8T (Kimura *et al.*, 2005; Momozawa *et al.*, 1985; Utsumi *et al.*, 2007). Ferroelectricity was also observed in  $\text{Ba}_2\text{Mg}_2\text{Fe}_{12}\text{O}_{22}$  and  $\text{Ba}_2(\text{Mg}_{1-x}\text{Zn}_x)_2\text{Fe}_{12}\text{O}_{22}$  Y - type hexaferrites, where the critical magnetic field to induce the ferroelectricity was dramatically reduced to 30 mT (Ishiwata *et al.*, 2008; Chun *et al.*, 2010). Chun and coworkers (Chun *et al.*, 2010) partially substituted Fe with Al in  $\text{Ba}_{0.5}\text{Sr}_{1.5}\text{Zn}_2(\text{Fe}_{1-x}\text{Al}_x)_{12}\text{O}_{22}$  and successfully induced the ferroelectric phase at 1 mT.

Manganites have also been studied much in last two decades due to their interesting properties and colossal magnetoresistance (CMR). The physical properties in manganese perovskites are thought to arise from the strong competition between a ferromagnetic double-exchange interaction, an

antiferromagnetic super-exchange interaction and the spin-phonon coupling (Hagaza *et al.*, 2009). The presence of mixed Mn ions gives rise to a double-exchange mechanism, increasing drastically electric conductivity and inducing ferromagnetic like behaviour with reentrant spin glass character (De Silva *et al.*, 1998; Ghivelder *et al.*, 1999). From the magnetic point of view pure LaMnO<sub>3</sub> is an *A*-type antiferromagnet with  $T_N^{x=0}=139.5$  K (where  $x$  is the Mn<sup>4+</sup> concentration) and a small spin canting due to the antisymmetric Dzialoshinski-Moriya interaction, giving rise to a weak ferromagnetic behavior with a saturation moment of  $\mu = 0.16 \mu_B/\text{Mn}$  (Skumryev *et al.*, 1999). In the *A*-type AF phase the spins in the *a-b* plane are ferromagnetically ordered. The ferromagnetic planes are stacked antiferromagnetically along the *c* axis (Chatterji *et al.*, 2008).

High quality thin films of materials are required for the device application although they have certain limitations due to their thickness and different properties as compared to bulk materials. In the case of thin films, studies to probe the physical phenomenon are complicated by the small sample and the elastic strain imposed by the substrate. LaMnO<sub>3</sub> thin films are typically found to be ferromagnetic due to their nonstoichiometry (Murugavel *et al.*, 2003; Choi *et al.*, 2009; Gupta *et al.*, 1995). The self doping owing to cation vacancies causes mixed Mn (Mn<sup>3+</sup>, Mn<sup>4+</sup>) valence to fulfil charge neutrality. As a result, ferromagnetic double-exchange (DE) and antiferromagnetic super-exchange (SE) mechanism coexist (Kleine *et al.*, 2006).

A lot of interests have grown in spintronic materials in last decade including dilute magnetic semiconductors and dielectrics such as transition metal doped oxide systems, e.g. ZnO, TiO<sub>2</sub>, HfO<sub>2</sub>, CeO<sub>2</sub>, SnO<sub>2</sub> etc. A key factor for application of these materials in spintronics devices is to have their Curie temperature much above room temperature. Oxide materials usually considered for this are non magnetic oxides having the magnetic impurity such as Fe, Ni or Mn etc. However, the experimental search for ferromagnetism in TM doped oxide materials did not result in reproducible and homogeneous magnetic materials. It has been reported several times that ferromagnetism can also be observed in materials which do not contain such magnetic impurities (ZrO<sub>2</sub>, HfO<sub>2</sub> etc.) and even doping with non magnetic ions (Bouzerar and Ziman, 2006; Maca *et al.*, 2008).

The general objectives of present thesis work were to synthesize different functional oxides in polycrystalline bulk and thin film forms, and to investigate their structural and magnetic properties for application in spintronics and multiferroics. Ba<sub>1-x</sub>Sr<sub>x</sub>Mg<sub>2</sub>Fe<sub>12</sub>O<sub>22</sub> (Y-type hexaferrites as multiferroic), perovskite LaMnO<sub>3</sub> and Mg, Ca doped ZrO<sub>2</sub> bulk samples were prepared by chemical solution method. Some of the representative thin films were also prepared by pulsed laser deposition (PLD) and atomic layer deposition (ALD) techniques, to compare their results with bulk samples. Results obtained on various samples of these oxides synthesized in bulk and thin films are presented in this thesis.

## ABBREVIATIONS

AF	Anti-ferromagnetic
AFM	Atomic force microscopy
ALD	Atomic layer deposition
B	Magnetic induction or magnetic flux density
$\chi$	Susceptibility
EDS	Energy dispersive spectroscopy
H	Magnetic field intensity
H <sub>A</sub>	Crystalline anisotropy
H <sub>C</sub>	Coercivity
LCMO	Lanthanum calcium manganese oxide
LMO	Lanthanum manganese oxide, (LaMnO <sub>3</sub> )
LSMO	Lanthanum strontium manganese oxide
M	Magnetization
M <sub>r</sub>	Remanent magnetization
M <sub>s</sub>	Saturation magnetization
MCA	Magneto-crystalline anisotropy
ME	Magnetoelectric
MFM	Magnetic force microscopy
NMR	Nuclear magnetic resonance
PLD	Pulsed laser deposition
SEM	Scanning electron microscopy
T <sub>C</sub>	Curie temperature
TM	Transition metal
VSM	Vibrating sample magnetometer

# 1. LITERATURE REVIEW

## 1.1. Magnetic Materials

Magnetism was observed as early as 800 BC in a naturally occurring material called load stone which was used for navigation purposes (Puri *et al.*, 1997). A loadstone is a naturally magnetized piece of the mineral magnetite ( $\text{Fe}_3\text{O}_4$ ). The word *magnet* derives from Magnesia, a Greek town and province in Asia Minor, the etymological origin of the word “magnet” meaning “the stone from Magnesia” (Cullity *et al.* 2009; Buschow *et al.* 2004). In the modern concept, all materials, viz., metals, semiconductors and insulators, are said to exhibit magnetism, though of different nature.

### 1.1.1. Magnetic quantities and Units

A magnet creates a magnetic field in the space around it, a magnetic field can also be created by an electric current. When a solid is placed in a magnetic field, it gets magnetized. The magnetic moment per unit volume developed inside a solid is called magnetization and is denoted by  $\mathbf{M}$ . The measure of the magnetic response of a medium to the action of a magnetic field is given by its *magnetic susceptibility*,  $\chi$ . The magnetic susceptibility is defined as the magnetization produced per unit applied field, i.e.,

$$\chi = \mathbf{M}/\mathbf{H} \quad (1.1.1)$$

where  $\mathbf{H}$  is the strength of the applied magnetic field also referred as *magnetic field intensity*. Both  $\mathbf{M}$  and  $\mathbf{H}$  are measured in amperes per meter ( $\text{A m}^{-1}$ ) or webers per square meter ( $\text{Wb m}^{-2}$ ) in the SI (abbreviated SI from French: *Système international d'unités*) system, and in oersteds (Oe) in the CGS (centimeter-gram-second) system, hence  $\chi$  is dimensionless quantity. The mass susceptibility (or specific susceptibility)  $\chi_g$  is the total magnetic moment divided by the field  $H$ , divided by the mass, and is measured in cubic meters per kilogram, it is related to the volume susceptibility through  $\chi_g = \chi / \rho$ , where  $\rho$  is the density. If  $\mathbf{M}$  refers to a gram molecule of a substance, the susceptibility is termed the molar susceptibility ( $\chi_m$ ).

The physical quantity that describes the effect of a magnet or current in its neighbourhood is the magnetic induction or magnetic flux density  $\mathbf{B}$ . A measure of magnetic induction may be given by Lorentz force, the force on a charge  $q$  in motion. The Lorentz force acting on a charge that moves with a velocity  $\mathbf{v}$  is given by

$$\mathbf{F} = q\mathbf{v} \times \mathbf{B} \quad (1.1.2)$$

The unit of magnetic induction in the SI system of units is tesla (T), defined as the magnetic induction that produces a force of 1 newton on a charge of 1 coulomb, moving with a velocity  $1 \text{ m s}^{-1}$  in the direction perpendicular to the

that of  $\mathbf{B}$ . The unit of  $\mathbf{B}$  in the CGS system is gauss (G), which corresponds to  $10^{-4}$  T.

The magnetic induction or magnetic flux density  $\mathbf{B}$  produced inside the medium as a consequence of the applied magnetic field  $\mathbf{H}$  is given by

$$\mathbf{B} = \mu_0 (\mathbf{H} + \mathbf{M}) \quad (1.1.3)$$

where  $\mu_0$  is the vacuum permeability and is equal to  $4\pi \times 10^{-7}$  Henry per metre ( $\text{Hm}^{-1}$ ) in SI system. In the CGS system,  $\mu_0$  has a value of 1 gauss per oersted. From Eq. (1.1.1) and (1.1.3), we obtain

$$\mathbf{B} = \mu_0(1 + \chi) \mathbf{H} \quad (1.1.4)$$

or 
$$\mathbf{B} = \mu \mathbf{H} \quad (1.1.5)$$

Where  $\mu$  is the magnetic permeability. A more general definition of  $\mu$  is given by  $\mu = \mathbf{B} / \mathbf{H}$ . The magnetic permeability of a material is in general not a constant, but depends on the value of the field  $\mathbf{H}$ . In anisotropic media,  $\mu$  and also  $\chi$ , depend on the direction of the applied field, and are second-rank tensors, however, in isotropic media  $\mu$  and  $\chi$  represent scalar quantities.

It is more convenient to introduce a dimensionless parameter  $\mu_r$  which is called the relative permeability of the medium and is given by

$$\mu = \mu_0 \mu_r \quad (1.1.6)$$

Thus, Eq. (1.1.5) becomes

$$\mathbf{B} = \mu_0 \mu_r \mathbf{H} \quad (1.1.7)$$

From Eq. (1.1.4) and Eq. (1.1.7), we get

$$\mu_r = (1 + \chi) \quad (1.1.8)$$

For the free space, i.e., in the absence of any material medium,  $\mathbf{M} = 0$ ,  $\chi = 0$ ,  $\mu = \mu_0$  and  $\mu_r = 1$ , and from the above relations, we obtain

$$\mathbf{B} = \mu_0 \mathbf{H} \quad (1.1.9)$$

(Guimarães, 1998; Puri *et al.*, 1997).

### 1.1.2. Classes of Magnetic Materials

The origin of magnetism lies in the orbital and spin motions of electrons and how the electrons interact with one another. The motion of electrons is equivalent to an electric current which produces the magnetic effects. The major contribution comes from the spin of unpaired valence electrons which produces permanent electronic magnetic moments. A number of such magnetic moments may align themselves in different directions to generate a net non-zero magnetic moment. Materials exhibit different behaviours in the presence of magnetic field. The main distinction is that in some materials there is no collective interaction of atomic magnetic moments, whereas in other materials there is a very strong interaction between atomic moments.

The magnetic behavior of materials can be classified into the following five major groups:

1. Diamagnetism
2. Paramagnetism
3. Ferromagnetism
4. Antiferromagnetism
5. Ferrimagnetism

Materials in the first two groups are those that exhibit no collective magnetic interactions and are not magnetically ordered. Materials in the last three groups exhibit long-range magnetic order below a certain critical temperature. Ferromagnetic and ferrimagnetic materials are usually what we consider as being magnetic (i.e., behaving like iron).

#### *1.1.2.1. Diamagnetism*

Diamagnetism is a fundamental property of all matter, although it is usually very weak. Diamagnetic substances are composed of atoms which have no net magnetic moments (i.e., all the orbital shells are filled and there are no unpaired electrons). However, when exposed to a field, a negative magnetization is produced.

Diamagnetism in a material arises due to changes in the atomic orbital states induced by the applied magnetic field. An electron revolving in an orbit constitutes an electric current. When a magnetic flux linked with such an electric circuit is changed, an induced current is set up in such a direction as to oppose the change in flux in accordance with the Lenz's law. The magnetic field of the induced current is opposite to the applied field and produces the diamagnetic effect. This type of magnetism is characterized by a small and negative susceptibility, independent of temperature (fig. 1.1.1). Examples of diamagnetic substances are sodium chloride (NaCl), Quartz (SiO<sub>2</sub>) and water (H<sub>2</sub>O).

#### *1.1.2.2. Paramagnetism*

Paramagnetism occurs in those atoms, ions and molecules which have permanent magnetic moments, due to unpaired electrons in partially filled orbitals. However, the individual magnetic moments do not interact magnetically, and like diamagnetism, the magnetization is zero when the field is removed. When a magnetic field is applied, these moments orient themselves in the direction of the field which results in some net magnetization parallel to the applied field.

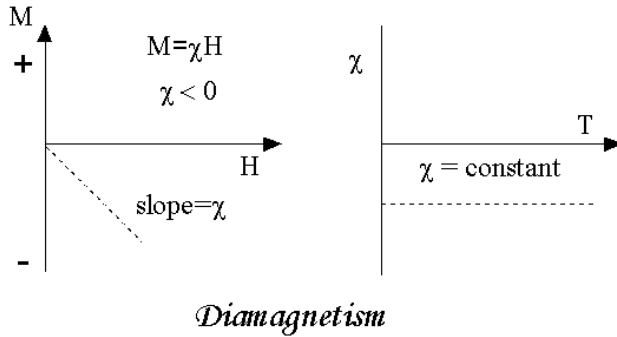


Figure 1.1.1. Susceptibility ( $\chi$ ) of diamagnetic materials

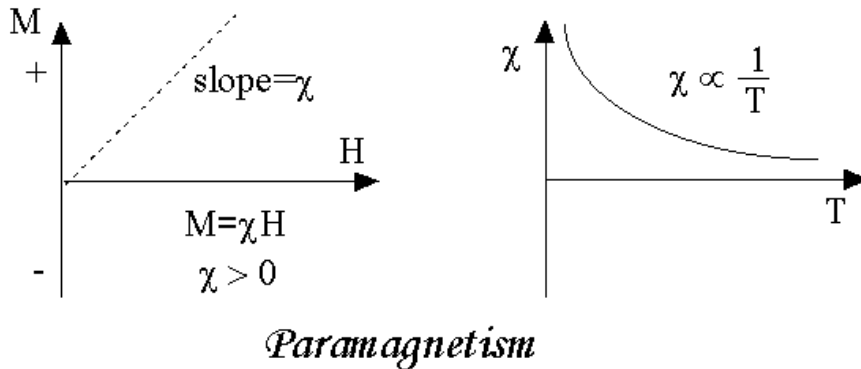


Figure 1.1.2. Susceptibility ( $\chi$ ) of paramagnetic materials

Paramagnetism characterized by a positive susceptibility whose inverse varies linearly with temperature (fig. 1.1.2). This type of temperature dependence (called the Curie law) is found at any temperature in the paramagnetic materials, or above a certain temperature of magnetic order, in ferromagnetic and antiferromagnetic materials (called in these cases the Curie-Weiss law). The fall in the susceptibility with temperature originates the increase in the ratio of thermal energy to the energy of the atomic magnetic moments in the presence of the external magnetic field. One type of paramagnetism 'Pauli paramagnetism' is due to the magnetic moments of the conduction electrons and in this case the susceptibility is practically constant with temperature. Examples of paramagnetic substances are Montmorillonite

(clay), Nontronite (Fe-rich clay), Pyrite (sulfide), Siderite (carbonate) and Biotite (silicate).

### 1.1.2.3. Ferromagnetism

This type of magnetism is characterized by a spontaneous parallel alignment of atomic magnetic moments, with long range order (fig. 1.1.3 (a)). Like paramagnetism, ferromagnetism is also associated with the presence of permanent magnetic dipoles, but unlike paramagnetism, the magnetic moments of adjacent atoms in this case are aligned in a particular direction even in the absence of the applied magnetic field. Thus a ferromagnetic material exhibits a magnetic moment in the absence of a magnetic field.

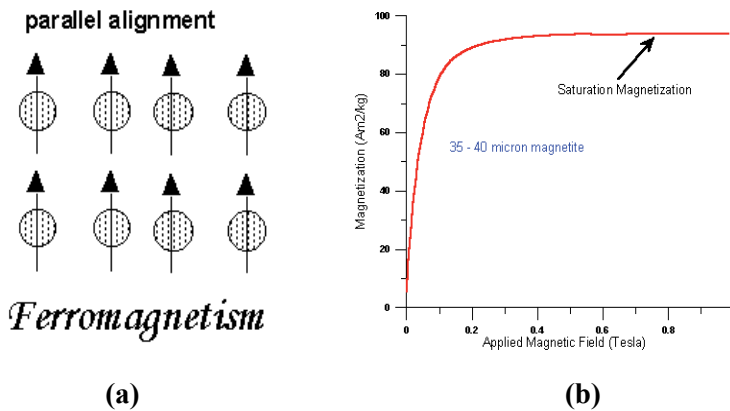


Figure 1.1.3. (a) Spin arrangement in ferromagnetic materials, (b) Magnetization versus magnetic field plot

The magnetization existing in a ferromagnetic material in the absence of an applied magnetic field is called the spontaneous magnetization. It exists below a certain critical temperature called the Curie temperature,  $T_c$  (fig. 1.1.4 (b)). Below the Curie temperature the alignment of magnetic moments is due to the exchange interaction between the magnetic ions. Above the Curie temperature, the thermal effects offset the spin alignment and the ferromagnetic substance becomes paramagnetic. The ferromagnetic substances acquire a large magnetization in the presence of even a weak external magnetic field (fig. 1.1.3 (b)). They possess a large and positive value of susceptibility which, in general, is not constant but varies with field strength. The variation of magnetization with field strength exhibits the well-known hysteresis curve (fig. 1.1.4 (a)). The elements Fe, Ni, and Co and a number of alloys and oxides such as MnBi, MnAs,  $\text{CrO}_2$ ,  $\text{Fe}_3\text{O}_4$ , etc. are typical ferromagnetic materials.

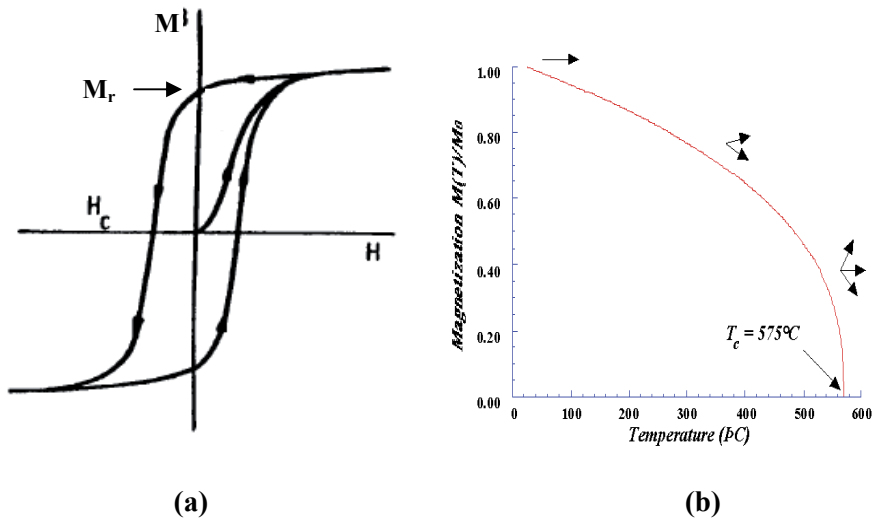


Figure 1.1.4. (a) Hysteresis curve of ferromagnetic material, (b) Dependence of magnetization on temperature

#### 1.1.2.4. Antiferromagnetism

Antiferromagnetism is the magnetism in which the atomic moments align antiparallel, with zero resulting magnetization (fig. 1.1.5 (a)). A crystal exhibiting antiferromagnetism may be considered to be consisting of two interpenetrating sublattices A and B, one of which is spontaneously magnetized in one direction and the other is spontaneously magnetized in the opposite direction. This type of magnetism was first observed in the crystal of MnO. In the absence of an external magnetic field, the neighbouring magnetic moments cancel out each other and the material as a whole exhibits no magnetization. In the presence of a magnetic field, a small magnetization appears in the direction of the field which increases further with temperature. This kind of behaviour is typical of an antiferromagnetic material. The magnetization becomes the maximum at a critical temperature  $T_N$ , called the Neel temperature, which is analogous to the Curie temperature in the paramagnetic or ferromagnetic substances. Above  $T_N$ , the susceptibility obeys the Curie-Weiss law for paramagnets but with a negative intercept indicating negative exchange interactions. The variation of susceptibility ( $\chi$ ) and inverse of susceptibility ( $1/\chi$ ) with temperature is shown in fig. 1.1.5 (b). Examples of antiferromagnetic substances are FeO and  $\text{Fe}_3\text{Mn}$ .

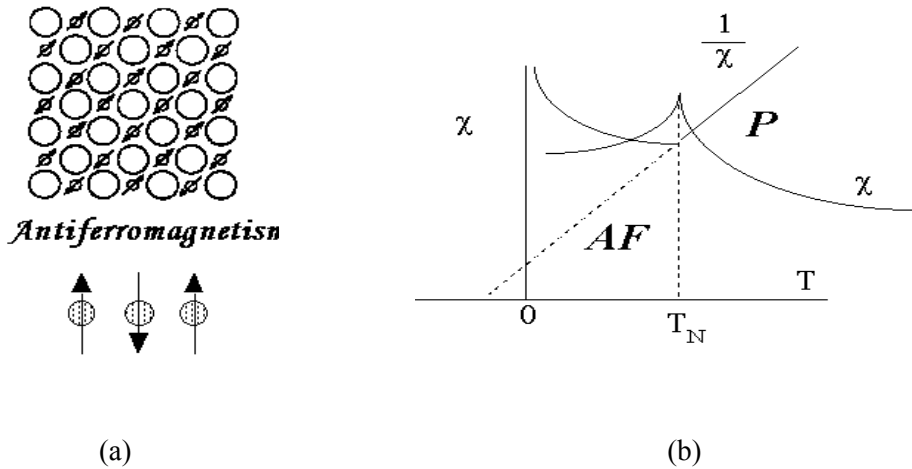


Figure 1.1.5. (a) Antiferromagnetic spin, (b) Temperature dependence of susceptibility ( $\chi$ ) and inverse susceptibility ( $1/\chi$ )

#### 1.1.2.5. Ferrimagnetism

Ferrimagnetism is identical to antiferromagnetism except that the magnetization of the two sublattices have different magnitudes which result in a non zero value of net magnetization. This type of magnetism occurs in materials such as ferrites which are basically the oxides of various metal elements. A simple representation of the magnetic spins in a ferrimagnetic oxide is shown in fig. 1.1.6. The magnetic structure is composed of two magnetic sublattices (called A and B) separated by oxygens. The exchange interactions are mediated by the oxygen anions. When this happens, the interactions are called indirect or superexchange interactions. The strongest superexchange interactions result in an antiparallel alignment of spins between the A and B sublattices. In ferrimagnets, the magnetic moments of the A and B sublattices are not equal and result in a net magnetic moment. Ferrimagnetism is therefore similar to ferromagnetism. It exhibits all the magnetic properties of ferromagnetic substances - spontaneous magnetization, Curie temperature, hysteresis, and remanence. However, ferro- and ferrimagnets have very different magnetic ordering. The most common example of ferrimagnetic substance is magnetite or ferrous ferrite,  $\text{Fe}_3\text{O}_4$  or  $\text{FeO}\cdot\text{Fe}_2\text{O}_3$ . It has been found

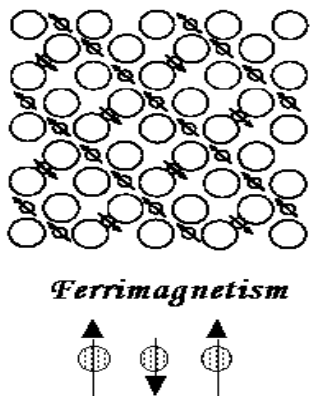


Figure 1.1.6. Spin in ferromagnetic materials

that for this particular ferrite, one  $\text{Fe}^{3+}$  ion occupies the tetrahedral or A-site, i.e., it is tetrahedrally coordinated to four oxygen anions while the other  $\text{Fe}^{3+}$  ion and the  $\text{Fe}^{2+}$  ion occupy the octahedral or B-sites, each being octahedrally coordinated to six oxygen anions. The ions present at A and B sites constitute A and B sublattices respectively and have opposite types of magnetizations. The net magnetization of a formula unit of  $\text{Fe}_3\text{O}_4$  is, therefore, equal to the magnetization of the single  $\text{Fe}^{2+}$  ion. However, one unit cell of magnetite having the spinel structure contains eight formula units of  $\text{Fe}_3\text{O}_4$  in it and according to the net magnetization of a unit cell is equal to the sum of the magnetizations of eight  $\text{Fe}^{2+}$  ions. Neel attributed the antiparallel arrangement of spins of A and B sites to the negative AB interaction. Besides this, there also exist the negative AA and BB interactions which are much weaker than AB interaction. Above the Curie temperature, the magnetization at both the sites obeys the Curie-Weiss law, whereas below this temperature the saturation effects come into existence.

## 1.2. Ferrites

Ferrites are chemical compounds consisting of ceramic materials with iron (III) oxide ( $\text{Fe}_2\text{O}_3$ ) as their principal component (Carter *et al.*, 2007). Many of them are magnetic materials and they are used to make permanent magnets, ferrite cores for transformers and in various other applications. Microwave ferrites are magnetic ceramic materials that refer to the entire family of iron oxides which includes spinels, garnets, orthoferrites, and hexaferrites (Smith *et al.*, 1959; Aulock *et al.*, 1965; Valenzuela, 1994; Goldman, 2006). Spinel structure materials are cubic and have the form  $\text{AB}_2\text{O}_4$  where A represents divalent cations and B trivalent cations of Fe. The exchange interaction between A and B sites is negative and strongest among the cations so that the net magnetization comes from the difference in magnetic moment between A and B sites. The garnets, like the spinels, also have a cubic structure but with trivalent cations (including rare earths and  $\text{Fe}^{3+}$ ) occupying tetrahedral (A), octahedral (B), or dodecahedral (C) sites. The interaction between tetrahedral and octahedral sites is antiparallel to the rare earth ions on the C sites. Specifically the chemical formula for garnets is  $3\text{Me}_2\text{O}_3 \cdot 5\text{Fe}_2\text{O}_3$  [alternatively dividing all by two -  $\text{Me}_3\text{Fe}_2(\text{FeO}_4)_3$ ] where Me represents the trivalent rare earth such as non magnetic yttrium or a magnetic rare earth such as from lanthanum through ytterbium. Rare earth orthoferrites are also classified as ferrites, although they are canted antiferromagnets. They have an orthorhombic crystal structure and the general chemical formula is  $\text{AFeO}_3$  where A is yttrium or a rare earth. The magnetic structure inside of a sublattice is usually collinear ferromagnetic, but the different sublattices are coupled antiferromagnetically. Due to the different sublattices, there is a net resulting magnetic moment, giving rise to ferrimagnetism. The nature of superexchange interaction depends not only on the type of magnetic ion, but rather strongly on the bond length and bonding angle. This makes it possible to change the strength and type of the

superexchange interaction, i.e. the magnetization and Neel point, by chemical substitutions of different size ions. Hexagonal ferrites, or hexaferrites, have an even more complicated crystal structure. There are different types of hexaferrites in terms of their composition. However, all of them share a similar crystal structure. The Fe cations are the sole source of magnetic moment and can be found on any of the three crystallographically different sites making up the hexaferrites: tetrahedral, octahedral, and hexahedral sites (Özgur *et al.*, 2009).

### 1.2.1. Hexagonal ferrites

There has been an increasing degree of interest in the hexagonal ferrites since their discovery in the 1950s, which is still growing exponentially today. These have become massively important materials commercially and technologically, accounting for the bulk of the total magnetic materials manufactured globally, and they have a multitude of uses and applications. As well as their use as permanent magnets, common applications are as magnetic recording and data storage materials, and as components in electrical devices, particularly those operating at microwave/GHz frequencies. The important members of the hexaferrite family are shown below, where Me is a small divalent ion such as cobalt, nickel or zinc, and Ba can be substituted by Sr:

- M-type ferrites, such as  $\text{BaFe}_{12}\text{O}_{19}$  (BaM or barium ferrite),  $\text{SrFe}_{12}\text{O}_{19}$  (SrM or strontium ferrite), and cobalt–titanium substituted M ferrite, Sr- or  $\text{BaFe}_{12-2x}\text{Co}_x\text{Ti}_x\text{O}_{19}$  (CoTiM).
- Z-type ferrites ( $\text{Ba}_3\text{Me}_2\text{Fe}_{24}\text{O}_{41}$ ), such as  $\text{Ba}_3\text{Co}_2\text{Fe}_{24}\text{O}_{41}$ , or  $\text{Co}_2\text{Z}$ .
- Y-type ferrites ( $\text{Ba}_2\text{Me}_2\text{Fe}_{12}\text{O}_{22}$ ), such as  $\text{Ba}_2\text{Co}_2\text{Fe}_{12}\text{O}_{22}$ , or  $\text{Co}_2\text{Y}$ .
- W-type ferrites ( $\text{BaMe}_2\text{Fe}_{16}\text{O}_{27}$ ), such as  $\text{BaCo}_2\text{Fe}_{16}\text{O}_{27}$ , or  $\text{Co}_2\text{W}$ .
- X-type ferrites ( $\text{Ba}_2\text{Me}_2\text{Fe}_{28}\text{O}_{46}$ ), such as  $\text{Ba}_2\text{Co}_2\text{Fe}_{28}\text{O}_{46}$ , or  $\text{Co}_2\text{X}$ .
- U-type ferrites ( $\text{Ba}_4\text{Me}_2\text{Fe}_{36}\text{O}_{60}$ ), such as  $\text{Ba}_4\text{Co}_2\text{Fe}_{36}\text{O}_{60}$ , or  $\text{Co}_2\text{U}$ . (Pullar, 2012)

The hexagonal ferrites are ferrimagnetic materials, and their magnetic properties are intrinsically linked to their crystalline structures. They all have magnetocrystalline anisotropy (MCA) that is the induced magnetization has a preferred orientation within the crystal structure. They can be divided into two main groups: those with an easy axis of magnetization, the uniaxial hexaferrites, and those with an easy plane (or cone) of magnetization, known as the ferroxplana or hexaplana ferrites. The best example of hexaferrites is Barium hexaferrite ( $\text{BaO}\cdot 6\text{Fe}_2\text{O}_3$  or  $\text{BaFe}_{12}\text{O}_{19}$ ) (Went *et al.*, 1952), the trade names for which are Ferroxdure and Indox (Wijn, 1952; Braun, 1952).

### 1.2.1.1. Structural Properties

Several related ferromagnetic oxides are also available all of which can be derived by combining the ferrite spinel ( $\text{MeO} \cdot \text{Fe}_2\text{O}_3$ ) and ferroxdure ( $\text{BaO} \cdot 6\text{Fe}_2\text{O}_3$ ) using the chemical composition diagram shown in fig. 1.2.1.

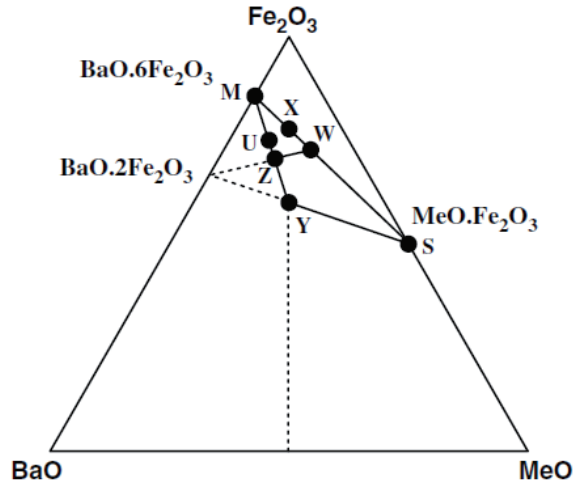


Figure 1.2.1. Chemical composition diagram showing how the hexagonal ferrites are derived from the spinel  $\text{MeO} \cdot \text{Fe}_2\text{O}_3$  structure (Özgür *et al.*, 2009)

As might be discerned from table 1.2.1 the crystalline and magnetic structures of the different types of hexaferrites are remarkably complex, but all types are interrelated. To elaborate further, utilizing the spinel structure  $\text{S} = 2\text{Me}^{2+}\text{Fe}_2\text{O}_4$  or  $2\text{MeO} \cdot 2\text{Fe}_2\text{O}_3$ , (where Me is Fe, Co, Mn, Ni, Cu, Mg, Zn) and  $\text{M} = \text{BaFe}_{12}\text{O}_{19}$  or  $\text{BaO} \cdot 6\text{Fe}_2\text{O}_3$ , the W-type hexaferrite with chemical formula of  $\text{BaMe}_2\text{Fe}_{16}\text{O}_{27}$  can be represented as  $\text{W} = \text{M} + \text{S}$ . The Y-type hexaferrite,  $\text{Y} = \text{Ba}_2\text{Me}_2\text{Fe}_{12}\text{O}_{22}$ , is a planar hexaferrite, and  $\text{Mg}_2\text{Y}$  is known as Ferroplana. Another planar hexaferrite,  $3\text{BaO} \cdot 2\text{MeO} \cdot 12\text{Fe}_2\text{O}_3$ , can be constructed by  $\text{Z} = \text{M} + \text{Y}$ . The X-type hexaferrite,  $\text{X} = 2\text{M} + \text{S}$ , is formed by stacking of R- and S-blocks along the hexagonal c-axis using the model  $\text{RSR}^*\text{S}^*\text{S}^*$ , where R is a hexagonal three-oxygen-layer block with composition  $\text{BaFe}_6\text{O}_{11}$ , and the asterisk indicates that the corresponding block is rotated  $180^\circ$  around the hexagonal axis. The structure of X-type compound is closely related to that of M- and W-type. The U-type hexaferrite can be constructed by  $\text{U} = 2\text{M} + \text{Y}$  as seen from the phase diagram in fig. 1.2.1.

There has been an explosion of interest in hexaferrites in the last decade for more exotic applications. This is particularly true for electronic components of mobile and wireless communications at microwave/GHz frequencies, electromagnetic wave absorbers for EMC, RAM and stealth technologies (especially the X and U ferrites), and composite materials. There is also a clear recent interest in nanotechnology, the development of nanofibres and fibre

orientation and alignment effects in hexaferrite fibres, and composites with carbon nanotubes (CNT). One of the most exciting developments has been the discovery of single phase magnetoelectric/multiferroic hexaferrites, firstly  $\text{Ba}_2\text{Mg}_2\text{Fe}_{12}\text{O}_{22}$  Y ferrite at cryogenic temperatures, and now  $\text{Sr}_3\text{Co}_2\text{Fe}_{24}\text{O}_{41}$  Z ferrite at room temperature. Several M, Y, Z and U ferrites have now been characterized as room temperature multiferroics (Pullar, 2012).

Table 1.2.1. Chemical composition and interrelation of hexagonal ferrites (Umit Özgür *et al.*, 2009)

Hexaferrite type	Composition (Chemical formula)	Stacking order <sup>a</sup>	Interrelation
S-spinel	$2\text{Me}^{2+} \cdot 2\text{Fe}_2\text{O}_4$ or $2\text{MeO} \cdot 2\text{Fe}_2\text{O}_3$		S
M	$\text{Ba}^{2+}\text{Fe}_{12}\text{O}_{19}$ or $\text{BaO} \cdot 6\text{Fe}_2\text{O}_3$	RSR*S*	M
W	$\text{Ba}^{2+}\text{Me}_2^{2+}\text{Fe}_{16}\text{O}_{27}$ $\text{BaO} \cdot 2\text{MeO} \cdot 8\text{Fe}_2\text{O}_3$	or RSSR*S*S*	M + S
Y	$\text{Ba}^{2+}\text{Me}_2^{2+}\text{Fe}_{12}\text{O}_{22}$ $\text{BaO} \cdot 2\text{MeO} \cdot 8\text{Fe}_2\text{O}_3$	or TSTSTS	Y
Z	$\text{Ba}_3^{2+}\text{Me}_2^{2+}\text{Fe}_{24}\text{O}_{41}$ $3\text{BaO} \cdot 2\text{MeO} \cdot 12\text{Fe}_2\text{O}_3$	or RSTSR*S*T*S*	M + Y
U	$\text{Ba}_4^{2+}\text{Me}_2^{2+}\text{Fe}_{36}\text{O}_{60}$ $4\text{BaO} \cdot 2\text{MeO} \cdot 18\text{Fe}_2\text{O}_3$	or RSR*S*T*S*	2M + Y
X	$\text{Ba}_2^{2+}\text{Me}_2^{2+}\text{Fe}_{28}\text{O}_{46}$ $2\text{BaO} \cdot 2\text{MeO} \cdot 14\text{Fe}_2\text{O}_3$	or RSR*S*S*	2M + S

<sup>a</sup> Sub-units for stacking order, using Me = Fe: S =  $\text{Fe}_6\text{O}_8$  (spinel), R =  $\text{BaFe}_6\text{O}_{11}$  (hexagonal), and T =  $\text{Ba}_2\text{Fe}_8\text{O}_{14}$  (hexagonal). The asterisk (\*) indicates that the corresponding sub-unit is rotated 180° around the hexagonal axis.

The crystalline structure of the hexagonal ferrites is the result of a close packing of oxygen ion layers. The divalent and trivalent metallic cations are located in interstitial sites of the structure, while the heavy Ba or Sr ions enter substitutionally the oxygen layers. All the known hexagonal ferrites have a crystalline structure which can be described as a superposition of three fundamental structural blocks: the so called S, R and T blocks (fig. 1.2.2). The S

block results from a cubic close packing of two oxygen layers giving rise to the typical spinel structure. The R and T blocks instead result from a hexagonal close packing of three and four oxygen layers respectively with part of the oxygen substituted by barium. The metallic cations are distributed among several lattice sites, up to ten or more, different both from the crystallographic and the magnetic point of view and therefore play different roles in determining the magnetic properties of the hexagonal ferrites (Albanese, 1977).

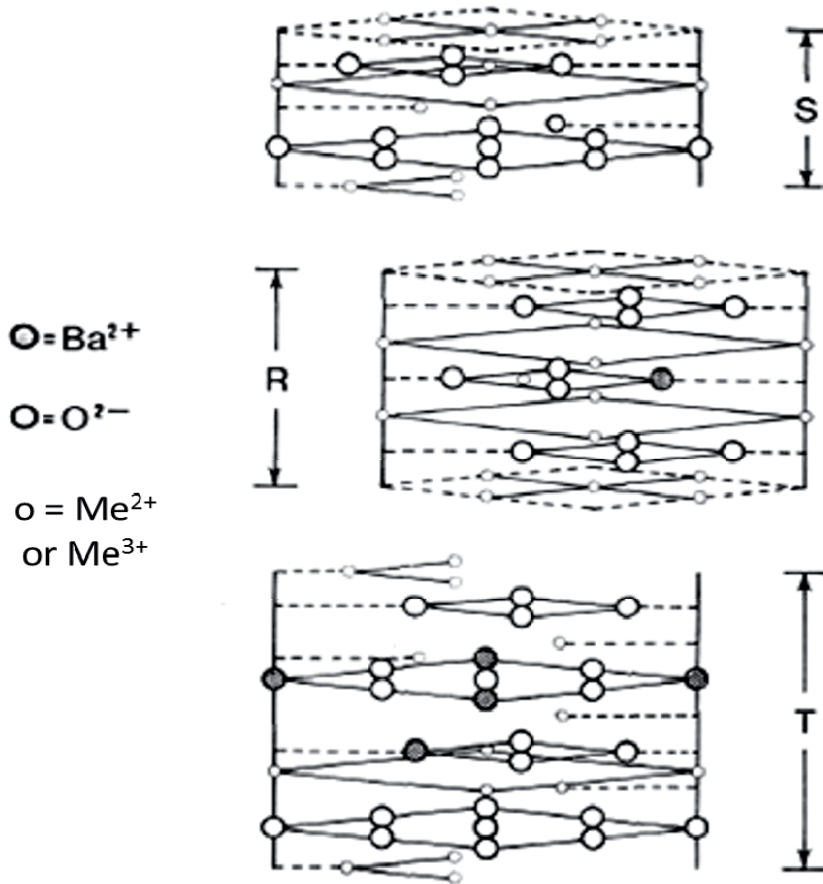


Figure 1.2.2. The three fundamental structural blocks S, R and T of the hexagonal ferrites (Albanese, 1977)

### 1.2.1.2. Magnetic Properties

#### (i) Magnetism in hexagonal ferrites

All hexagonal ferrites contain at least one large metal 2+ ion (usually  $\text{Ba}^{2+}$  or  $\text{Sr}^{2+}$ ), which causes a slight perturbation in the lattice due to size differences,

and is responsible for the magnetocrystalline anisotropy (MCA) in hexaferrites. The most common hexagonal ferrites have a preferred axis of magnetization along the c-axis, so loose crystals in an applied field will align themselves with the c-axis parallel to the field, showing a different XRD pattern to randomly oriented samples. The magnetic properties are different if measured in the direction of alignment,  $M_s$  saturates at a lower applied field and  $H_c$  is larger if the field is applied parallel to the c-axis, compared to if a field is applied perpendicular to this “easy” axis. The ratio of  $M_r/M_s$  for isotropic unaligned samples is around half that for well oriented samples (Smith and Wijn, 1959), and  $T_c$  is also higher in the direction of the c-axis in oriented samples (Belov *et al.*, 1965). The degree of this MCA is given by the crystalline anisotropy,  $H_A$ , in  $\text{Am}^{-1}$ , and the anisotropy constant  $K_1$  is a measure of the difficulty to move the magnetization out of that direction in the crystal lattice. MCA is connected to the energy needed to turn a magnetization vector from the preferred low energy, or easy direction, to a difficult, higher energy orientation, represented by the anisotropy constants  $K_1$  and  $K_2$ . For single hexagonal crystals the total anisotropy energy is given by the sum  $\sum_K = K_0 + K_1 \sin^2\phi + K_2 \sin^4\phi + \dots$ , where  $K_0$  is the energy to magnetize the easy axis, and  $\phi$  is the angle between the direction of magnetization and the c-axis (Heck, 1974). The higher order terms are not usually necessary for uniaxial ferrites,  $K_0$  has a low value as the easy axis is a low energy orientation, and often even the second order term is not required.

(ii) Magnetic moments and superexchange in hexagonal ferrites

Each S block consists of two layers of four oxygen atoms with three cations between each layer, in octahedral and tetrahedral sites having opposing magnetic spins. There are four octahedral magnetic moments and two opposing tetrahedral moments, giving a net total of two moments. The R block has five octahedral moments, but due to the effects of the large barium atom two of them are really distorted tetrahedral sites and so they oppose the other three octahedral sites. The moment of the five-coordinate trigonal bipyramidal site is aligned with three of the octahedral moments as it is a distorted octahedral site, and so the total also results in a net of two moments. The T section has six octahedral and two tetrahedral moments, but again two of the octahedral moments are aligned with the tetrahedral, giving a net of zero magnetic moments. The tetrahedral sites are formed by the two barium atoms distorting two trigonal bipyramidal sites (Smith and Wijn, 1959).

Table 1.2.2. Magnetic spin in different lattice sites of S, R and T blocks

---

S block = 2↓ tetrahedral and 4↑ octahedral = 2↑
R block = 1↑ trigonal bipyramidal and 3↑ 2↓ octahedral = 2↑
T block = 2↓ tetrahedral and 4↑ 2↓ octahedral = 0

---

These net values are only true if all the cations are  $\text{Fe}^{3+}$ , which has a magnetic moment of  $5 \mu_B$ . For example in BaM, which consists of S + R, and therefore has a net magnetic moment of  $4\uparrow = 20 \mu_B$  (Smith and Wijn, 1959). In ferrites other than M, and in doped M ferrites, some of the cations are other metals with different magnetic moments, which may occupy different sites depending upon composition and temperature, and may occupy on a fraction of the total number of a certain site. The opposing spins of the T block, which is antiferromagnetic if all the ions are identical, lead to the lower magnetic saturation values for the Y ferrites compared to the other hexagonal ferrites. This explains the many variations seen in the magnetic properties of the hexagonal ferrites with temperature and composition, but it also means that to calculate the magnetic moment of a compound the exact positions of all the cations must first be known.

In metals the spins are linked by exchange interactions between the magnetic moments of directly neighbouring atoms, and this short range interaction is negligible over longer distances. However, in ferrimagnetic ferrites the magnetic ions are separated from one another by oxygen atoms making them too far apart for direct exchange, and there are also shielding effects from the oxygen lattice. In 1948 the idea of superexchange was suggested, which involves the non-magnetic oxygen atoms in the interactions (Neel, 1948). The spins of opposing neighbouring ions are linked by interactions which take place via the intermediate oxygen atom ( $\text{Me}_1\text{-O-Me}_2$ ), and this process is called superexchange. The magnitude of the exchange can be estimated from the  $\text{Me}_1\text{-O-Me}_2$  distance and the angle formed by this, with a shorter distance and a larger angle strengthening the interaction. An angle of  $180^\circ$  gives the largest interaction and an angle of  $90^\circ$  the smallest, and the effect decreases rapidly with distance, becoming negligible over a Me-O distance of  $3 \text{ \AA}$  (Anderson, 1950).

### (iii) Grain size dependence of magnetic properties of hexagonal ferrites

A better sintered, and therefore denser, ferrite has more magnetic moments per unit volume and hence a higher  $M_s$ , but the heat treatment needed to maximize densification also usually results in grain growth giving a multi-domain particle with a lowered coercivity as some of the domains will oppose one another. Therefore, the optimization of magnetic properties in hexagonal ferrites is dependant upon the particle size of the starting material and the sintering conditions employed (Richter, 1968). A material with high  $M_r$  and  $H_c$  can be made by mixing nanosized powders of a high  $M_r$  magnet such as  $\alpha$ -iron and a high coercivity magnet such as  $\text{Nd}_2\text{Fe}_{14}\text{B}$  together, to form a composite magnet (Fischer and Kronmuller, 1998), and this would also work with ferrites. Clearly reducing the grain size to, or below, the domain size will raise the coercivity, but a material with magnetically aligned domains will also have a higher coercivity, and oriented single crystal materials will approach the theoretical maximum values permitted. The magnetization process under an applied field

depends upon the size and shape of the ferrite particles. If it consists of plates under 5  $\mu\text{m}$  the material is magnetically conditioned by rotational processes, with grain over 10  $\mu\text{m}$  wall movement dominates, with the critical grain size falling at temperatures below room temperature (Sixtus *et al.*, 1956).

### 1.2.2. Y-type hexaferrite ( $\text{Ba}_2\text{Me}_2\text{Fe}_{12}\text{O}_{22}$ )

#### 1.2.2.1. Structural Properties

The molecular unit of Y ferrite is one S and one T unit, with a total of six layers, the unit cell consists of three of these units, with the length of the c-axis being 43.56 Å, and is a member of the space group R3m (Braun, 1957). The T block does not have a mirror plane, and therefore a series of three T blocks is required to accommodate the overlap of hexagonal and cubic close packed layers, with the relative positions of the barium atoms repeating every three T blocks. This gives the unit cell formula as simply 3(ST), and the structure is shown in fig. 1.2.3 (a).

The metallic cations are distributed among six sublattices as reported in table 2 where the basic spin orientation is also indicated. It is worth noting that inside the T block, three octahedral ions, belonging to  $6c_{\text{VI}}$  and  $3b_{\text{VI}}$ , sublattices, lies on a vertical threefold axis, the central  $3b_{\text{VI}}$ , ion sharing two faces of its coordination figure with the adjacent  $6c_{\text{VI}}$  ions. Such a configuration, as already pointed out, is responsible for a higher potential energy of the structure due to a stronger electrostatic repulsion between the cations; therefore such sites are likely to be preferred by low charge ions. As a consequence a non-magnetic  $\text{Me}^{2+}$  ions with a marked preference for the octahedral coordination may cause drastic changes in the magnetic configuration with respect to the usual Gorter scheme; indeed the occupation of either  $6c_{\text{VI}}$ , or  $3b_{\text{VI}}$ , by non-magnetic ions leads to the cancellation of the antiferromagnetic  $b_{\text{VI}}\text{-}c_{\text{IV}}^*$ , interaction which is the strongest one in the Y-structure (Albanese, 1977).

Table 1.2.3. Number of ions per unit formula, coordination and spin orientation for the various metallic sublattices of Y-structure (Albanese, 1977)

Sublattice	Coordination	Block	Number of ions per unit cell	Spin
<b>6 <math>c_{\text{IV}}</math></b>	tetrahedral	S	6	down
<b>3 <math>a_{\text{VI}}</math></b>	octahedral	S	3	up
<b>18 <math>h_{\text{VI}}</math></b>	octahedral	S-T	18	up
<b>6 <math>c_{\text{VI}}</math></b>	octahedral	T	6	down
<b>6 <math>c_{\text{IV}}^*</math></b>	tetrahedral	T	6	down
<b>3 <math>b_{\text{VI}}</math></b>	octahedral	T	3	up

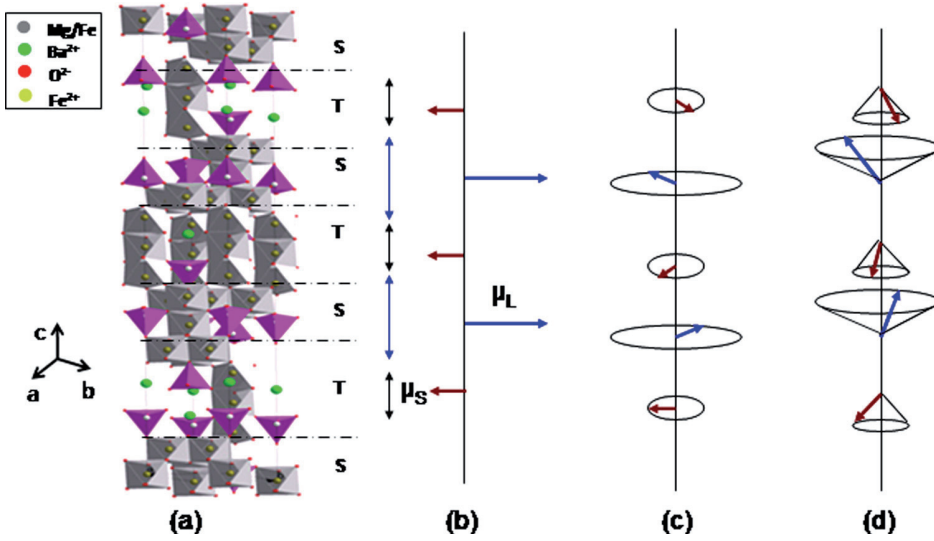


Figure 1.2.3. (a) Schematic crystal structure of Y-type hexaferrite, (b) the ferromagnetic structure consists of alternate stacks of two spin blocks with  $\mu_L$  (larger magnetic moments) and  $\mu_S$  (small magnetic moments) along c-axis, (c) and (d) represent the proper screw structure and longitudinal conical spin order states respectively exhibited at lower temperatures (Ishiwata *et al.*, 2008; Ishiwata *et al.*, 2009)

### 1.2.2.2. Magnetic Properties

The Y ferrites all have lower magnetization than the M ferrites, the highest being for  $Zn_2Y$  ( $18.4 \mu_B$ ,  $M_s = 72 \text{ A m}^2 \text{ kg}^{-1}$  at 0 K) (Smith and Wijn, 1959), and getting lower in the sequence  $Zn > Mn > Co > Ni$  (Slovak *et al.*, 1977). At room temperature,  $Zn_2Y$  has  $M_s = 42 \text{ A m}^2 \text{ kg}^{-1}$ , but the Curie point of  $Zn_2Y$  is only  $130 \text{ }^\circ\text{C}$ , and it has a low crystalline anisotropy of only  $716 \text{ kA m}^{-1}$  (9 kOe) (Smith and Wijn, 1959).  $Ni_2Y$  made by Sudakar *et al.* at only  $950 \text{ }^\circ\text{C}$  was a very soft ferrite, with  $M_s = 25.5 \text{ A m}^2 \text{ kg}^{-1}$ ,  $H_c = 16 \text{ kA m}^{-1}$  and a  $T_C$  of  $387 \text{ }^\circ\text{C}$  (Sudakar *et al.*, 2003), and it has a higher  $H_A$  of  $1100 \text{ kA m}^{-1}$  (14 kOe) (Smith and Wijn, 1959).

Most Y ferrites and all the  $Co_2$  ferrites are ferroplana (Jonker *et al.*, 1956, Lotgering *et al.*, 1961), with a preferred direction of magnetization either in the hexagonal basal plane, or in a cone at an angle to the c-axis. As in the uniaxial ferrites the magnetization is locked rigidly in this orientation, but in the ferroplana ferrites it can rotate within the plane or cone of magnetization. The first order anisotropy constant,  $K_1$ , is positive for the uniaxial ferrites, but negative for the ferroplana ferrites, indicating that the magnetization is out of the c-axis. However, the second and third order constants  $K_2$  and  $K_3$  become more important and often must be considered with the ferroplana ferrites. The  $K_2$  constant is positive and relatively large (but  $< -K_1$ ) in ferroplana ferrites with the easy axis in the basal plane and therefore reduces the total anisotropy effect when added to a negative  $K_1$  and with planar ferrites the anisotropy field

in the basal plane,  $H_A$ , is proportional to  $-(K_1 + 2 K_2)$ . In ferroxplana ferrites with an easy cone of magnetization, although the third order constant,  $K_3$  is positive, it is  $\sim 10^{-3}$  of the magnitude of  $K_1$ . Therefore, the negative  $K_1$  usually still dominates in ferroxplana ferrites, indicating an easy plane of magnetization.

To understand magnetic structures of the hexaferrite system, it is convenient to consider two kinds of structural blocks that are different from the T and S blocks mentioned above. One is the L block with large spin moments ( $\mu_L$ ), and the other is the S block having small spin moments ( $\mu_S$ ), as seen in fig. 1.2.3. Thus, the Y-type hexaferrite can be viewed as alternate stacks of the L and S blocks along the hexagonal c-axis. Within the respective blocks, the magnetic moments on Fe (and Me) sites lying in the ab plane are collinear and form a ferrimagnetic structure. The boundary of these blocks is located between the fourth [Fe(4)] and fifth [Fe(5)] layers. The number in parentheses is the layer number of ions (for example, Fe(4) means Fe at the fourth layer). The superexchange interaction across the boundary of these blocks, Fe(4)-O(2)-Fe(5), is reinforced by replacing Ba with Sr (Pollert, 1985; Kimura, 2012).

#### 1.2.2.3. Substituted Y ferrites

$\text{Sr}_2\text{Zn}_2\text{Y}$  showed a strange, non-collinear magnetic structuring due to the  $\text{Sr}^{2+}$  ion distorting the lattice (Perekalina *et al.*, 1970), and therefore the replacement of barium with strontium in Y ferrites steadily reduced the permeability, but a 50% substitution of lead increased it dramatically (Castelliz *et al.*, 1969). Kimura *et al.* reported in 2005 (Kimura *et al.*, 2005) that single crystals of  $\text{Ba}_{2-x}\text{Sr}_x\text{Zn}_2\text{Y}$  form a non-collinear helical spin structure for values of  $x$  between 1.0 – 1.6, which is modulated by applied magnetic field, producing a Y ferrite with exciting ME properties near room temperature when a field of 1 – 1.5 T is applied ( $x = 1.5$ ). This step wise change in  $M_s$  with applied magnetic field in a pure phase hexaplana ferrite appears to be an indication of such a change in magnetic structure, and signals it out as of interest for future investigation. Ferroelectricity was also observed in  $\text{Ba}_2\text{Mg}_2\text{Fe}_{12}\text{O}_{22}$  and  $\text{Ba}_2(\text{Mg}_{1-x}\text{Zn}_x)_2\text{Fe}_{12}\text{O}_{22}$  Y-type hexaferrites, where the critical magnetic field to induce the ferroelectricity was dramatically reduced to 30 mT (Ishiwata *et al.*, 2008; Chun *et al.*, 2010). Chun and coworkers (2010) partially substituted Fe with Al in  $\text{Ba}_{0.5}\text{Sr}_{1.5}\text{Zn}_2(\text{Fe}_{1-x}\text{Al}_x)_{12}\text{O}_{22}$  and successfully induced the ferroelectric phase at 1 mT.

Because Ba (or Sr) ions are situated near two Fe sites (Fe(4) and Fe(5)), the substitution of small Sr for large Ba causes the change in the Fe(4)-O(2)-Fe(5) bond angle. For example, the Fe(4)-O(2)-Fe(5) bond angles in Sr-free  $\text{Ba}_2\text{Zn}_2\text{Fe}_{12}\text{O}_{22}$  and  $\text{Ba}_{2-x}\text{Sr}_x\text{Zn}_2\text{Fe}_{12}\text{O}_{22}$  ( $x = 1.5$ ) are  $113^\circ$  and  $118^\circ$ , respectively (Utsumi *et al.*, 2007). The Sr-free crystal shows a collinearly ferrimagnetic order at  $T_N = 392$  K with the parallel arrangement of the Fe(4) and Fe(5) moments (Gorter, 1957), whereas in the Sr-rich ( $x > 1.0$ ) samples the angle between Fe(4) and Fe(5) moments ( $\phi/2$ ) becomes finite at room temperature,

then the system shows a proper-screw magnetic structure consisting of the L and S blocks (Momozawa *et al.*, 1985; Momozawa, 1986) at the ground state, as illustrated in fig. 1.2.3 (b). For example, the  $\phi$ , i.e., turn angle of helix, in an  $x = 1.5$  single crystal ( $T_N \approx 330$  K) is  $83.4^\circ$  at 8 K (Momozawa and Yamaguchi, 1993). Thus, the increase of the bond angle causes the magnetic frustration at the boundary between the L and S blocks, and then stabilizes a noncollinear screw magnetic structure. It is interesting to note that the T block, which contains the Fe(4)-O(2)-Fe(5) bonds, is key to producing the noncollinear screw structure in the Y-type hexaferrite. This screw magnetic structure in Sr-rich  $\text{Ba}_{2-x}\text{Sr}_x\text{Zn}_2\text{Fe}_{12}\text{O}_{22}$  does not allow magnetically induced polarization due to the inverse DM mechanism. The inverse effect of the antisymmetric DM interaction (Dzyaloshinskii, 1958; Moriya, 1960) is that in which two noncollinearly coupled magnetic moments displace the ligand intervening between them through the electron-lattice interaction (Sergienko and Dagotto, 2006). However, by the application of a magnetic field perpendicular to the  $c$  axis, the system undergoes successive metamagnetic transitions (Momozawa and Yamaguchi, 1993; Momozawa *et al.*, 1985) and shows concomitant magnetically induced polarization in some of the magnetic field-induced phases (Kimura *et al.*, 2005).

In substitutions of Co with Zn to give the compound  $\text{Co}_{1-x}\text{Zn}_x\text{Y}$  fired at  $1000^\circ\text{C}/10$  h,  $T_C$  falls linearly from  $340^\circ\text{C}$  ( $x = 0$ ) to  $100^\circ\text{C}$  ( $x = 1$ ). The  $M_s$  values increased with addition, but they were lower than expected with  $M_s = 26.6$  (instead of 34) and  $32.9$  (instead of 42)  $\text{A m}^2 \text{kg}^{-1}$  for  $x = 0$  and 1 respectively (Lee *et al.*, 1996). Zinc weakens the super interactions and lowers  $T_c$ , but there is no change in the spin directions so the net magnetic moment increases with addition.  $M_s$  showed a peak of  $34.9$   $\text{e A m}^2 \text{kg}^{-1}$  at  $x = 0.75$ , but this was attributed to thermal agitation of the  $x = 1$  compound at room temperature as  $M_s$  showed a steady increase when measured at 77 K. The low  $M_s$  and  $T_c$  values also suggest that perhaps the material was not single phase Y. When made from the coprecipitation of superparamagnetic  $\delta\text{-FeOOH}$  and heated to  $1200^\circ\text{C}$ ,  $\text{Zn}_2\text{Y}$  was produced in which the grain size =  $2 \mu\text{m}$ ,  $M_s = 32.7$   $\text{A m}^2 \text{kg}^{-1}$  and  $M_r/M_s = 0.06$  (Kim *et al.*, 1992). Other studies of the  $\text{Co}_{1-x}\text{Zn}_x\text{Y}$  system showed similar trends in  $M_s$  values, and  $H_c$  values decreasing steadily with  $x$  from  $\sim 12.7$   $\text{kA m}^{-1}$  for  $\text{Co}_2\text{Y}$  to  $< 4$   $\text{kA m}^{-1}$  for  $\text{Zn}_2\text{Y}$  (Bai *et al.*, 2003).  $\text{Zn}_{1.2}\text{Cu}_{0.8}\text{Y}$  sintered at  $1050^\circ\text{C}$  ( $\rho = 5.12$   $\text{g cm}^{-3}$ ) was reported has having  $M_s = 34.5$   $\text{A m}^2 \text{kg}^{-1}$ ,  $M_r = 4.05$   $\text{A m}^2 \text{kg}^{-1}$  and  $H_c = 6.8$   $\text{kA m}^{-1}$ , and in  $\text{Zn}_{1.2-2x}\text{Co}_{2x}\text{Cu}_{0.8}\text{Y}$  these values increased slightly with a small addition of  $\text{Co}^{2+}$  up to  $x = 0.1$ , as did the density (Bai *et al.*, 2004).

$\text{ZnMnY}$  was found to have a volume magnetization of  $183$   $\text{kA m}^{-1}$ ,  $H_A = 756$   $\text{kA m}^{-1}$  and  $H_c = 1.43$   $\text{kA m}^{-1}$  (Obol and Vittoria, 2003). Other substituted Y ferrites reported by the same authors, made by the flux melt method in  $\text{BaCO}_3/\text{B}_2\text{O}_3$  glass at  $1200^\circ\text{C}$ , include  $\text{Co}_{0.25}\text{Zn}_{1.75}\text{Y}$  ( $H_A = 1151$   $\text{kA m}^{-1}$ , volume magnetization of  $159$   $\text{kA m}^{-1}$ , and  $H_c = 0.318$   $\text{kA m}^{-1}$ ) and  $\text{Mn}_{0.25}\text{Co}_{0.75}\text{ZnY}$  ( $H_A = 1958$   $\text{kA m}^{-1}$ , volume magnetization of  $159$   $\text{kA m}^{-1}$ , and  $H_c = 318$   $\text{kA m}^{-1}$ ), very soft ferrites with extremely small  $H_c$  values (Obol and Vittoria, 2003).

Although magnetic ordering temperatures of these Y-type hexaferrites are above room temperature, their ME effects can be observed only up to ~110 K (Kimura *et al.*, 2005). This is mainly because these hexaferrites are not sufficiently insulating to sustain a substantial macroscopic ferroelectric polarization above ~130 K. Related to this conductive nature, the relative dielectric constant and loss tangent of the Y-type hexaferrite significantly increase with increasing temperature. It has been reported that a postannealing procedure in an oxygen atmosphere enhances the electrical resistivity of the Y-type hexaferrite (Chai *et al.*, 2009). Nevertheless, the annealed sample is not still sufficiently insulating to sustain a substantial electric polarization at higher temperatures (Kimura *et al.*, 2012).

### **1.3. Ferromagnetism in non-magnetic zirconium dioxide by transition metal and non-magnetic dopants**

#### *1.3.1. Zirconia*

Zirconium dioxide ( $ZrO_2$ ) also known as zirconia, is a white crystalline oxide of zirconium and a non magnetic material. Its most naturally occurring form with a monoclinic crystalline structure is the mineral baddeleyite. At atmospheric pressure pure zirconia may exist as one of three phases: cubic, tetragonal and monoclinic (Ruff and Ebert, 1929; Murray and Allison, 1954; Lynch *et al.*, 1961; Patil and Rao, 1970; Maiti *et al.*, 1972; Hueur and Riihle, 1984). A high-pressure allotropic form of zirconia (orthorhombic) has also been reported; this phase is metastable at atmospheric pressure and reverts to the monoclinic form by such a mild treatment as grinding in a mortar (Suyama *et al.*, 1985). Pure zirconia undergoes a number of reversible phase transitions during heat treatment. Control over the stability is achieved by doping zirconia with one or more of the fluorite stabilizer oxides (Mustafa, 1997), CaO (Kumar *et al.*, 1995), MgO (Hughan and Hannink, 1986),  $Y_2O_3$  (Luo and Stevens, 1999) and  $CeO_2$  (Yin *et al.*, 1999) are used to achieve either fully or partially stabilized zirconia. The very high melting temperature of zirconia makes it a prime candidate for refractory applications. Zirconia is a candidate material for components that are subjected to high thermal shock resistance, high temperature and corrosive environments. Zirconia has been utilized in seals, engines, cutting tools, sensors, and thermal barrier coatings (Schwartz, 1992). Stabilized zirconia is used in oxygen sensors and fuel cell membranes because it has the ability to allow oxygen ions to move freely through the crystal structure at high temperatures. This high ionic conductivity (and a low electronic conductivity) makes it one of the most useful electroceramics (Nielsen, 2005).

### 1.3.2. Crystal structure

The three well-known structural forms of zirconia are monoclinic, tetragonal, and cubic phase, which are discussed below.

#### 1.3.2.1. Cubic Phase

The Cubic phase,  $c\text{-ZrO}_2$ , is the simplest structure formed by pure zirconia and is stable from the melting point at 2710 °C to 2380 °C (Baker, 1992). The structure is based on the fluorite ( $\text{CaF}_2$ ) structure, in which each zirconium atom is coordinated by 8 equidistant oxygen atoms. This can be visualized by cations occupying FCC positions in a cubic lattice, with eight interstitial oxygen atoms and a large vacancy in the centre, as shown in fig. 1.3.1 (a). The space group of this structure is  $Fm\text{-}3m$  (No. 225), with Zr and O located at  $0\ 0\ 0$  and  $\frac{1}{4}\ \frac{1}{4}\ \frac{1}{4}$  positions respectively. The lattice parameter 'a' is approximately 5.15 Å, which when extrapolated to room temperature, becomes approximately 5.12 Å (Kisi and Howard, 1998).

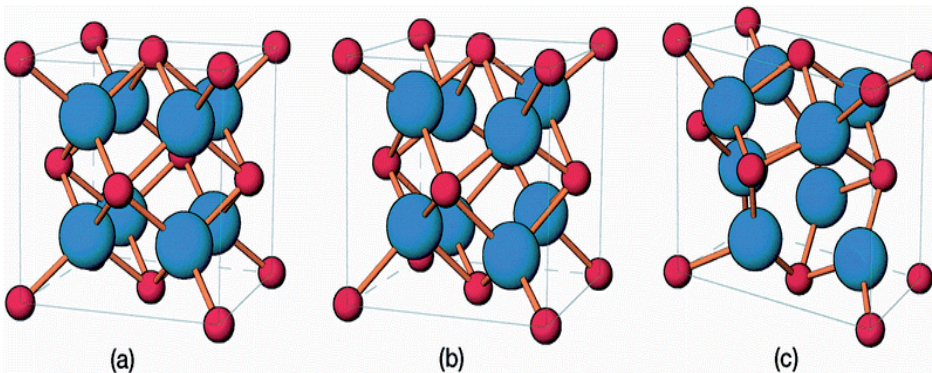


Figure 1.3.1. Unit cell of (a) cubic, (b) tetragonal, (c) monoclinic phase zirconia, (Zirconium atoms are red, oxygen atoms are blue)

#### 1.3.2.2. Tetragonal Phase

The tetragonal phase,  $t\text{-ZrO}_2$ , is thermodynamically stable in bulk zirconia from 2380 °C to approximately 1100 °C. It is closely related to the cubic structure, as shown in fig. 1.3.1 (b), but differs in two respects. Firstly, there is a distortion in the lattice, corresponding to a slight elongation along the c-axis. Secondly, there is a displacement of columns of oxygen atoms alternately up or down the c-axis. The effect is to move four oxygen neighbours closer to the zirconium atom, and the other four oxygen neighbours away from it. The interdependent distortions are required to prevent O-O contact (Kisi and Howard, 1998). Each zirconium atom maintains its eight-fold coordination of oxygen: four oxygen atoms at a distance of  $\sim 2.1$  Å and four at a distance of  $\sim 2.3$  Å. It is important to note that

the outer oxygen neighbours for one zirconium atom, are also the inner neighbours for neighbouring zirconium atoms.

The space group of the body-centered primitive unit cell is  $P4_2/nmc$  (No. 137), with approximate dimensions  $a = 3.6 \text{ \AA}$  and  $c = 5.2 \text{ \AA}$ , and the assignment of diffraction peaks etc., is generally made using this unit cell. The tetragonal phase can also be indexed to a higher symmetry face-centered supercell has a parallel c-axis and the same c value as the primitive unit cell, and a and b axes at  $45^\circ$  to those of the primitive unit cell.

The positions of the zirconium and oxygen atoms in the primitive unit cell are table 1.3.1. The zirconium atoms are fixed with respect to their unit cell positions, while the position of the oxygen atoms in the c-axis, z, can vary. The oxygen atoms in the undistorted cubic structure have an equivalent position of  $z = \frac{1}{4}$ , so the above-mentioned displacement of the oxygen atoms along the c-axis can be defined as  $\delta = \frac{1}{4} - z$  (Kisi and Howard, 1998).

Table 1.3.1. Position of atom in unit cell of  $ZrO_2$

Atom	Wyckoff letter	Positions in unit cell
Zr	a	$0, 0, 0; \frac{1}{2}, \frac{1}{2}, \frac{1}{2}$
O	d	$0, \frac{1}{2}, z; \frac{1}{2}, 0, -z; 0, \frac{1}{2} + z; \frac{1}{2}, 0, -z$

The diffraction pattern of the tetragonal phase is almost identical to that of the cubic phase, except for the ‘splitting’ of a number of peaks to form doublets, caused by the slight elongation of the c-axis. When the peaks are broad, for instance due to small crystal size, it can be difficult to distinguish the diffraction patterns of the two phases unless the high-angle peaks are examined (Nishizawa *et al.*, 1982; Yashima *et al.*, 1996) or vibrational spectroscopy is used (Srinivasan *et al.*, 1991).

### 1.3.2.3. Monoclinic Phase

The monoclinic phase (m) is thermodynamically stable in bulk zirconia at temperatures below approximately  $1100 \text{ }^\circ\text{C}$ . The unit cell (fig. 1.3.1 (c)) can be described as a distorted cubic cell, although the structure is significantly more complex than that of the cubic and tetragonal phases. Unlike the simpler phases, each zirconium atom in the monoclinic structure is coordinated by 7 oxygen atoms, with bond lengths varying from  $2.04 - 2.26 \text{ \AA}$ , and with a range of O-Zr-O bond angles (Smith and Newkirk, 1965). The oxygen atoms are arranged in two parallel (1 0 0) planes, separated by layers of zirconium atoms. The structure is indexed with the space group  $P2_1/c$  (Yoshimura, 1988). The unit cell parameters at room temperature vary somewhat between studies (Smith and Newkirk, 1965; Hill and Cranswick, 1994; Howard *et al.*, 1988; Hann *et al.*, 1985; Adam and Rogers, 1959). The value treated as authoritative for a recent

round-robin on powder diffraction (Hill and Cranswick, 1994) are listed in table 1.3.2.

Table 1.3.2. The unit cell parameters of  $ZrO_2$  at room temperature in monoclinic phase

---

a	5.1454 (5) Å
b	5.2075 (5) Å
c	5.3107 (5) Å
$\beta$	99.23 (8)°

---

#### 1.3.2.4. Phase stabilization

It is well known that the addition of relatively small amount of certain other oxides into zirconia will drastically alter the relative stability of the phases (Kisi and Howard, 1998; Yoshimura, 1988; Heuer *et al.*, 1988; Garvie, 1988). The transformation temperature lowered and the tetragonal or cubic phases may become stable or metastable at ambient temperature. The dopant oxides that achieve this effect are usually oxides of divalent or trivalent metals, such as MgO, CaO,  $Y_2O_3$  or lanthanide oxides. Zirconia that is partially stabilized (PSZ), containing a mixture of phases, is an important engineering ceramic with a high toughness. This toughness is derived from the transformation of metastable tetragonal crystal into the monoclinic phase (Kisi and Howard, 1998; Butler, 1985).

The mechanism for stabilization is generally associated with the presence of oxygen vacancies in the lattice. These are created to balance the charge of the di- or trivalent cations which are substituted on the  $Zr^{4+}$  sites. The anion vacancy sites are, in effect, positively charged, so that neighbouring oxygen anions move closer to the vacancy and cations are displaced outward, permitting relaxation of the lattice structure. Although it is generally thought that this mechanism is largely responsible for the stabilization of the cubic phase (Kisi and Howard, 1998; Withers *et al.*, 1995), it remains uncertain what role oxygen vacancies play in the stabilization of the tetragonal phase (Kisi and Howard, 1998; Lu *et al.*, 1997). Other critical factors include the size of the stabilizing cation and the crystal structure of the stabilizing oxide (Kisi and Howard, 1998; Yoshimura, 1988; Howard *et al.*, 1998; Kim, 1997).

#### 1.3.3. Magnetism in non magnetic oxides

Dilute magnetic semiconductors (DMS) have attracted vast interest in the last decade because of the possibility of assembling charge and spin degrees of freedom in a single substance. That makes them promising candidates for technological applications in spintronic devices, utilizing both the electronic

charge as well as their spins (Ohno, 1998; Dietl *et al.*, 2000; Matsumoto *et al.*, 2001). With this hope to realize spintronic devices such as spin valves, spin transistors, spin light-emitting diodes (LEDs), ultrafast optical switches, etc, a significant amount of research effort has been focused on discovering materials suitable for these applications. A large number of transition metal (TM) doped oxides have been examined since the first prediction of ferromagnetism in Mn-doped ZnO by Dietl *et al.* in 2000 (Dietl *et al.*, 2000). A remarkable amount of research has been carried out to understand the nature of magnetism in TM-doped oxide systems, such as ZnO, TiO<sub>2</sub>, HfO<sub>2</sub>, CeO<sub>2</sub>, SnO<sub>2</sub> and In<sub>2</sub>O<sub>3</sub> (Sharma *et al.*, 2003; Bryan *et al.*, 2004; Coey, *et al.*, 2005; Wen *et al.*, 2007; Ogale *et al.*, 2003; Philip *et al.*, 2004). However, the experimental search for ferromagnetism in TM-doped oxide materials has not yet resulted in reproducible and homogeneous magnetic materials.

Interestingly, ferromagnetism has been suggested to be possible even in systems that do not contain magnetic impurities, materials often referred to as *d0* or intrinsic ferromagnets (Bouzerar and Ziman, 2006; M'aca *et al.*, 2008). Experimentally, it has been shown that thin films of HfO<sub>2</sub> and ZnO (Venkatesan *et al.*, 2004; Venkatesan *et al.*, 2004) exhibit such type of ferromagnetism with a rather high Curie temperature ( $T_c$ ). The ferromagnetism with high Curie temperature was also proposed by substitution of the four-valent cation  $A^{4+}$  in dioxides such as  $AO_2$  ( $A = \text{Ti, Zr, or Hf}$ ) by a monovalent cation of group 1A of the periodic table (M'aca *et al.*, 2008). HfO<sub>2</sub> and ZrO<sub>2</sub> are both wide-band insulating materials with a high dielectric constant; the possibility of making them ferromagnetic could widen their possible application in the emerging field of spintronics.

Recent theoretical studies also predicted high-temperature ferromagnetism in TM-doped cubic zirconia (Ostanin *et al.*, 2007) and K-doped ZrO<sub>2</sub> (M'aca *et al.*, 2008). However, doping with Cu (Dutta *et al.*, 2008), Cr (Ostanin *et al.*, 2007) or Ca (M'aca *et al.*, 2008) in ZrO<sub>2</sub> can result in paramagnetism, antiferromagnetic or non-magnetic ground states, respectively. According to these theories, single oxygen vacancy induces local magnetic moments on the neighbouring oxygen atoms, which then interact with extended exchange coupling. Motivated by these promising theoretical predictions of ferromagnetism in doped ZrO<sub>2</sub>, a few experimental works have been carried out to confirm the room-temperature ferromagnetism in  $Zr_{1-x}Mn_xO_2$  (Yu *et al.*, 2008; Dimri *et al.*, 2011; Hong *et al.*, 2012) and  $Zr_{1-x}Fe_xO_2$  (Clavel *et al.*, 2008). However, experimental results were controversial in these studies, and ferromagnetism was not shown up to the level, which has been predicted.

#### 1.4. Perovskite Manganites

The perovskite manganites have been extensively studied for their novel properties and potential applications (Millis, 1998). Perovskite is a group of materials that represents similar crystal structure as its prototype calcium

titanium oxide,  $\text{CaTiO}_3$ . Perovskite minerals were first discovered in Ural Mountains of Russia and were named after Russian mineralogist L. A. Perovski. Perovskite-type materials can be represented by their general formula as  $\text{ABX}_3$  where, A and B are any two different sized cations and X is the anion bonding them. Most of the perovskites contain oxygen as the anion. Hence, perovskite oxides can be presented by their general formula as  $\text{ABO}_3$ . In perovskite oxides, the A ion can be a rare earth element, alkali element or other large ion like  $\text{Pb}^{2+}$ ,  $\text{Bi}^{3+}$ ; which can fit into the dodecahedron frame and B ions can be 3d, 4d or 5d transition metal ions placing themselves at the octahedral sites as shown in fig. 1.4.1.

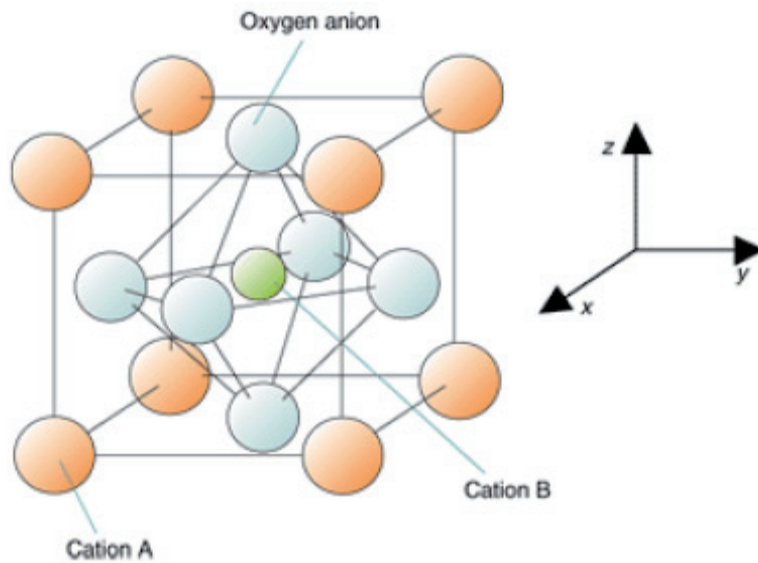


Figure 1.4.1. Representation of the crystal structure of perovskite oxide

Generally, perovskite oxides can only be formed if the tolerance factor,  $T$ , ranges between 0.8 - 1.0 (Goldschmidt, 1927-1928). The tolerance factor,  $T$ , is given by

$$T = (R_a + R_o) / \sqrt{2} (R_b + R_o) \quad (1.4.1)$$

where,  $R_a$  and  $R_b$  are the atomic radii of A and B cations and  $R_o$  is the ionic radius of oxygen. Ideal perovskite oxides have all the atomic states filled. Electrons cannot move freely through the crystal as the atoms are bonded with strong ionic bonds. This makes the perovskite electrically insulating. Also, perovskites are cubic and isotropic. The unusual and interesting properties of perovskite oxides, as mentioned before, come into play when there is distortion in lattice structure differing from the ideal one. If the tolerance factor,  $T$ , is differed from its range, i.e., if the radius of ion A is very large compared to ion B, then, the octahedral structure of B ions gets tilted leading to the distortion in

lattice. The symmetry of the lattice gets affected resulting in altering the electrical, optical, elastic, magnetic properties. Some tilted perovskites contain a B atom at the center of their octahedron structure. In some other perovskites, the positions of B cations is shifted resulting in ferroelectricity due to electric polarity of the crystals. BaSrTiO<sub>3</sub> can be an example of this type.

The structure of perovskite manganites always deviates from the ideal cubic structure by both the rotation of MnO<sub>6</sub> octahedron and the stretch of the Mn-O bond (Solovyev *et al.*, 1996). Properties of the perovskite also can be varied by substituting either A or B ions with different ions. Lanthanum strontium manganite (La<sub>1-x</sub>Sr<sub>x</sub>MnO<sub>3</sub>) is one example where A cation lanthanum is substituted by strontium. PZT is an example of replacement of B cation where some amount of titanium is replaced by zirconium. (Sakhalkar, 2009)

### 1.4.1. Lanthanum Manganite

Lanthanum manganite (LaMnO<sub>3</sub>) with perovskite structure have gained much attention in the last two decades due to their colossal magneto-resistance (CMR) effect, complex magnetic behaviour and interesting physical properties (Tokura *et al.*, 1996; Mills, 1998; De *et al.*, 2005; Nakayama *et al.*, 2003; Siwach *et al.*, 2008). These effects are believed to arise due to strong coupling among the charge, lattice and spin degrees of freedom. Defects, doping and electronic stabilities play crucial role in determining the materials properties (Ritter *et al.*, 1997, Kim and Christen, 2010). Even without cation doping, LMO has a very rich phase diagram due to its oxygen nonstoichiometry (Salamon and Jaime, 2001; Töpfer and Goodenough, 1997). Some important properties of this material are discussed in following sections.

#### 1.4.1.1. LaMnO<sub>3</sub> Electronic Structure (Jahn-Teller effect)

Undoped lanthanum manganite having chemical formula La<sup>3+</sup>Mn<sup>3+</sup>O<sub>3</sub><sup>2-</sup> is a transition-metal oxide with the perovskite structure, the 3d transition metal ion (i.e. Mn ion) is surrounded by six oxygen ions, as shown in fig. 1.4.1. Due to the crystal-field effects, the 3d bands split into an e<sub>g</sub> doublet and a t<sub>2g</sub> triplet degeneracy. The lower lying orbitals, t<sub>2g</sub> states, are d<sub>xy</sub>, d<sub>yz</sub> and d<sub>zx</sub>, while the higher lying one, e<sub>g</sub> are d<sub>x<sup>2</sup>-y<sup>2</sup></sub> and d<sub>3z<sup>2</sup>-r<sup>2</sup></sub>. The crystal field splitting between e<sub>g</sub> and t<sub>2g</sub> states is about 1 eV. The e<sub>g</sub> orbitals are oriented towards the neighboring oxygen atoms while t<sub>2g</sub> states have nodes in that direction suggesting that only e<sub>g</sub> orbitals can intermix with oxygen p-orbitals (Helmholt *et al.*, 1993). The degeneracy of e<sub>g</sub> and t<sub>2g</sub> orbitals can be lifted due to the orbital-lattice interaction called the Jahn-Teller effect. For example, when the oxygens in z-axis move toward or away from the transition metal ion, the local symmetry is broken and the e<sub>g</sub>-orbital degeneracy splits into the d<sub>x<sup>2</sup>-y<sup>2</sup></sub> and d<sub>3z<sup>2</sup>-r<sup>2</sup></sub> orbitals. Because the strong hybridization with ligands, e<sub>g</sub> electrons have a strong Jahn-Teller effect. However, for the t<sub>2g</sub> orbital, the orbital degeneracy is associated with the weaker π-bonding. Therefore the energy splitting of t<sub>2g</sub> orbital is less

than that of  $e_g$  orbital. The  $d_{yz}$  and  $d_{zx}$  orbitals are still degenerate by symmetry. Only  $d_{xy}$  orbital will have a different energy. The Jahn-Teller effect thus reduces the total energy. For example, as shown in fig. 1.4.2, a distortion in which the oxygen ions in the  $\pm z$  direction move away from the transition metal ion and the others in the  $x$  and  $y$  direction move closer will make the energy of  $d_{x^2-y^2}$  orbital higher than that of  $d_{3z^2-r^2}$  orbital. For  $Mn^{3+}$ , there are four electrons in the 3d energy band, three in the  $t_{2g}$  and the other in the  $e_g$ . The energy of  $d_{3z^2-r^2}$  orbital with the Jahn-Teller effect is reduced. In addition, the cooperative Jahn-Teller effect will cause an orbital order.

According to Hund's rule, all the d electrons on a Mn ion must have same spin means all the three electrons in the  $t_{2g}$  states will have the same spin. Also, one electron in  $e_g$  state should also have same spin as in electrons in  $t_{2g}$  state. Also, Jahn-Teller effect should be considered here for the distortion of the crystal. The Jahn-Teller theorem states that any non-linear molecular system in a degenerate electronic state will be unstable and will undergo distortion to form a system of lower symmetry and lower energy, thereby removing the degeneracy. With an electron in the  $e_g$  state, this will lower the energy of the system (Helmholt *et al.*, 1993).

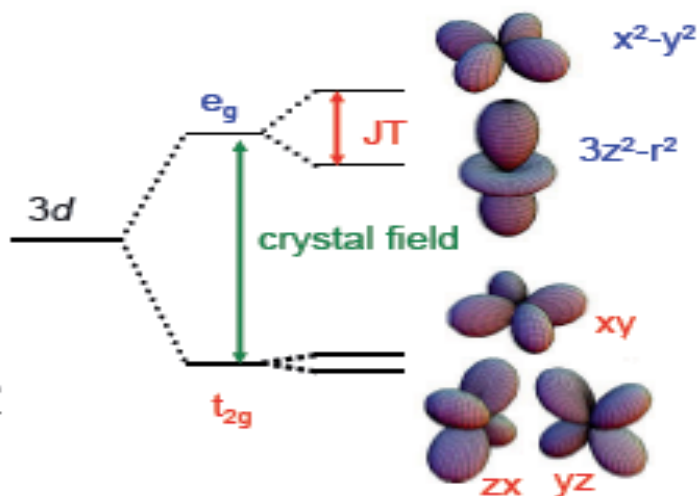


Figure 1.4.2. Schematic figure of the 3d band of the transition metal ion with an octahedral crystal field and the Jahn-Teller effect

#### 1.4.1.2. Double Exchange

The correlation between the electrical conductivity and ferromagnetism was introduced by Jonker and Van Santen (Van Santen and Jonker, 1950) through the theory of double exchange proposed by Zener (Zener, 1951). This theory predicts that an electron may be exchanged between two species and has important implications for whether materials are ferromagnetic,

antiferromagnetic or neither with relative ease. In the double exchange phenomenon  $\text{Mn}^{3+}\text{-O- Mn}^{4+}$  and  $\text{Mn}^{4+}\text{-O- Mn}^{3+}$  bonds degenerate, leads to delocalization of the electron at  $\text{Mn}^{4+}$  site. The delocalization of electron at  $\text{Mn}^{4+}$  site lowers the energy of system and there is an energy gain by aligning the  $t^{2g}$  spins. The delocalization of electron at  $\text{Mn}^{4+}$  site can be shown as fig. 1.4.3.

Undoped LMO is an insulator at room temperature because all Mn ions have one electron in the lower  $e_g$  level. An electron needs to go to the higher  $e_g$  level to move from  $\text{Mn}^{3+}$  site to  $\text{Mn}^{4+}$  site. Under the Neel temperature, the energy of this barrier gets lower and the spin canted ferromagnetism induces in LMO.

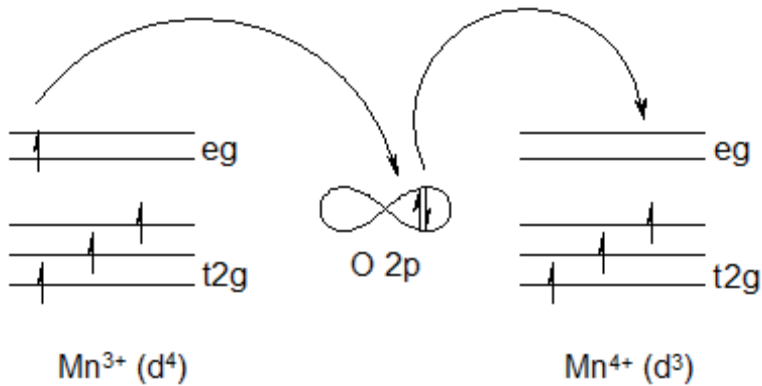


Figure 1.4.3. Representation of Double Exchange Mechanism

In ferromagnetism (fig. 1.4.4 (a)), the exchange energy is minimized when all the spins are parallel as occurs in pure iron. When spins are perfectly antiparallel (antiferromagnetism, fig. 1.4.4 (b)), there is no net magnetic moment, as occurs in ilmenite. Occasionally the antiferromagnetic spins are not perfectly aligned in an antiparallel orientation, but are canted by a few degrees. This spin-canting (fig. 1.4.4 (c)) gives rise to a weak net moment, as occurs in hematite, a common magnetic mineral.

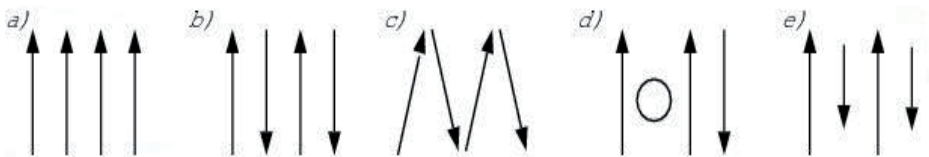


Figure 1.4.4. Types of spin alignment in ferromagnetism (a) ferromagnetism, (b) antiferromagnetism, (c) spin-canted antiferromagnetism, (d) defected antiferromagnetism, (e) ferrimagnetism

As doping percentage in LMO increases, more numbers of Mn<sup>3+</sup> - Mn<sup>4+</sup> pairs will lead to ferromagnetism. The relationship between electrical conductivity and percentage of Mn<sup>4+</sup> was given by Zener (Zener, 1951) as,

$$\sigma = (xe^2/ah) (T_c/T) \quad (1.4.2)$$

where, T is temperature, T<sub>c</sub> is Curie temperature, a is lattice parameter and x is fraction of Mn<sup>4+</sup> ions.

The Mn-O-Mn bond is not usually ideal 180°, as the perovskite structure is not perfect. The bond length and bond angle plays a major role in the manganites properties like magnetism and conductivity. Batlogg and coworkers (Hwang *et al.*, 1995) showed that, it is possible to vary the ionic radius of the ion at A-site perovskite by using different trivalent rare earth element ions. Their experiments showed that, with increase in radius of A-site ion, temperature for metal insulator transition T<sub>mi</sub> also increased. By increasing the A-site radius, the rotations of the octahedrons become smaller and Mn-O-Mn bond angle close to 180°. Zhang and coworkers (Wang and Zhang, 2002) compared the effects of applying external pressure to undoped LMO to the application of phase change and the change in lattice parameter and lattice structure. They showed that application of external pressure of 10 kbar and 15 kbar leads to phase transition in undoped LMO and transition temperature varies with the amount of pressure applied. The decrease in cell volume caused by the isostatic pressure will reduce the ionic size mismatch, which will decrease the rotation of oxygen octahedron, getting θ closer to 180°.

#### 1.4.1.3. Superexchange Interaction

Superexchange (or Kramers–Anderson superexchange) is the strong (usually) antiferromagnetic coupling between two next-to-nearest neighbor cations through a non-magnetic anion. In this way, it differs from direct exchange in which there is coupling between nearest neighbor cations not involving an intermediary anion. Superexchange is a result of the electrons having come from the same donor atom and being coupled with the receiving ions spins. If the two next-to-nearest neighbor positive (Mn) ions are connected at 90° to the bridging non-magnetic anion (O), then the interaction can be a ferromagnetic interaction. Superexchange was proposed by Hendrik Kramers in 1934 when he noticed in crystals like MnO that there are Mn atoms that manage to interact with one another despite having nonmagnetic oxygen atoms between them (fig. 1.4.5) (Kramers, 1934). Phillip Anderson later refined Kramers' model in 1950 (Anderson, 1950).

A set of semi-empirical rules were developed by John B. Goodenough and Junjiro Kanamori in the 1950s (Goodenough, 1955; Goodenough, 1958; Kanamori, 1959). These rules are known as the Goodenough-Kanamori rules, which are based on the symmetry relations and electron occupancy of the overlapping atomic orbitals. Essentially, the Pauli Exclusion Principle dictates

that between two magnetic ions with half-occupied orbitals, which couple through an intermediary non-magnetic ion (e.g.  $O^{2-}$ ), the superexchange will be strongly anti-ferromagnetic while the coupling between an ion with a filled orbital and one with a half-filled orbital will be ferromagnetic. The coupling between an ion with either a half-filled or filled orbital and one with a vacant orbital can be either antiferromagnetic or ferromagnetic, but generally favors ferromagnetic (Lalena and Cleary, 2010). When multiple types of interactions are present simultaneously, the antiferromagnetic one is generally dominant since it is independent of the intra-atomic exchange term (Weihe and Güdel, 1997). For simple cases, the Goodenough-Kanamori rules readily allow the prediction of the net magnetic exchange expected for the coupling between ions. Complications begin to arise in various situations: (1) when direct exchange and superexchange mechanisms compete with one another, (2) when the cation-anion-cation bond angle deviates away from  $180^\circ$ , (3) when the electron occupancy of the orbitals is non-static or dynamical and (4) when spin-orbit coupling becomes important.

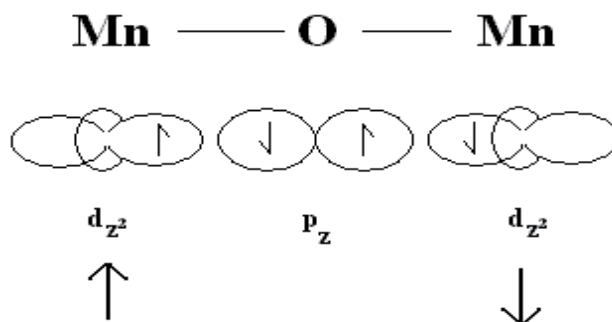


Fig. 1.4.5. Representation of superexchange for MnO

#### 1.4.1.4. Crystal structure

The ideal structure of lanthanum manganite is perovskite cubic with lattice parameter  $a = 0.387$  nm. If there is a deviation from the difference in radii of A and B site ions (Goldschmidt Tolerance Factor), then new unit cell will be of different type due to change in crystal symmetry. Coey and Viret (Coey and Viret, 1999) showed that, the Jahn-Teller effect causes distortion by elongating oxygen octahedron in some direction. Also, with a larger misfit of ionic sizes, there will be buckling of  $MnO_6$  octahedron to an orthorhombic structure. The structure of lanthanum manganite thin films depends upon substrate crystal structure as well as film processing parameters.

### 1.4.1.5. Electronic Transport

The resistivity vs. temperature curve for typical calcium doped LMO is as shown in fig. 1.4.6. The curve shows two distinct regions. The region at the lower temperatures, showing increase in resistance with temperature and the region at high temperature showing decrease in resistivity with temperature. Below the peak resistivity the sample shows the metallic behavior and semiconducting above. The sample is ferromagnetic in the metallic region and paramagnetic in the semiconducting region. Temperature at the maximum slope is called the transition temperature  $T_{tr}$ , this temperature is close to the ferromagnetic ordering temperature  $T_c$ .

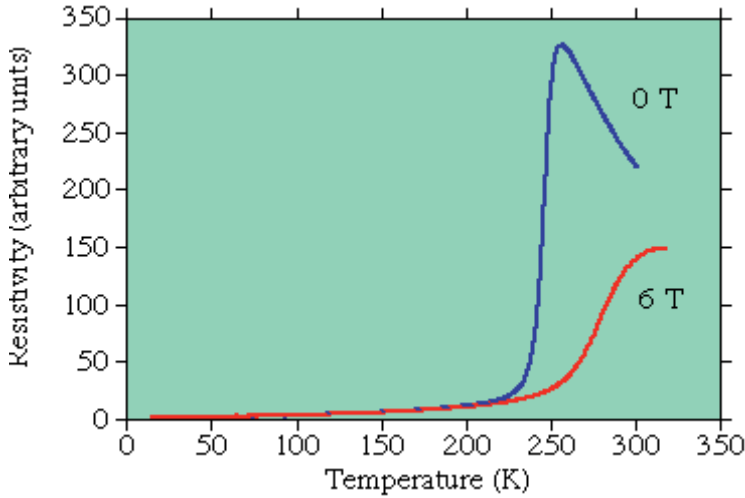


Figure 1.4.6. Temperature vs. resistivity curve for a typical epitaxial  $\text{La}_{0.67}\text{Ca}_{0.33}\text{MnO}_3$

For the temperature vs. resistivity curve, the resistivity, plotted as  $\log \rho$  versus  $1/T$  follows straight line, showing activated behavior,

$$\rho(T) \propto e_0^{E/kT} \quad (1.4.3)$$

where  $e_0$  is the activation energy and  $k$  is Boltzmann constant in the paramagnetic region (Van Santen and Jonker, 1950). In the ferromagnetic region, the resistivity has been found to be described as

$$\rho(T) = \rho_0 + AT^2 + BT^{4.5} \quad (1.4.4)$$

Kubo and Ohata (Kubo and Ohata, 1972) in their work showed that the term  $T^{4.5}$  is caused by two magnon process. Since the charge carriers at low temperature are spin-polarized, first order spin-wave interactions will decrease exponentially with temperature. Such processes would give a  $T^2$  behavior of the resistivity.

Therefore it has been suggested that the  $T^2$  term comes from electron-electron scattering.

#### 1.4.1.6. Magnetic properties

The stoichiometric  $\text{LaMnO}_3$  end member contains only  $\text{Mn}^{3+}$  magnetic ions which arrange themselves in the A-type planar antiferromagnetic structure (fig. 1.4.7 (A)) with a Neel temperature  $T_N = 140$  K. The arrangement in the a-b plane is ferromagnetic (spins in plane with the moments parallel to the orthorhombic b-axis in the Pbnm space group (a-axis in Pnma)) but successive planes are coupled antiferromagnetically (Wollan and Koehler, 1955; Elemans *et al.*, 1971). The moment in the A mode is  $3.87 \mu_B$ , in-plane and intraplane exchange parameters have been determined by inelastic neutron scattering. There may be a weak moment along the c-axis (Matsumoto, 1970; Anane, 1998) attributed in the stoichiometric compound to the Dzyaloshinsky (Dzyaloshinsky, 1958) - Moriya (Moriya, 1960) interaction (*Dzyaloshinsky-Moriya (DM) interaction: antisymmetric, anisotropic exchange coupling between two magnetic moments on a lattice bond with no inversion center*). Precise measurements on untwinned single crystals at 20 K have shown that there is a moment of  $0.18 \mu_B/\text{Mn}$  along the c-axis but no moment was measured along the a- or b-axes. A narrow peak in the susceptibility at  $T_N$  is characteristic of a canted antiferromagnet (Coey *et al.*, 1999).

Cation-deficient lanthanum manganites  $(\text{LaMn})_{1-\delta}\text{O}_3$  are antiferromagnetic, orthorhombic and insulating when  $\delta < 0.03$ , but compounds with  $\delta > 0.03$  are ferromagnetic with a spin-only moment of up to  $3.8 \mu_B$  per manganese atom (Ranno *et al.*, 1996; Mahendiran, *et al.*, 1996; Töpfer *et al.*, 1996). A sample with  $\delta = 0.04$  has a canted spin structure with the moments at  $45^\circ$  to the rhombohedral (0 0 1) axis (Cheetham *et al.*, 1996). The  $\delta \leq 0.04$  compounds remain insulating to low temperatures but the  $\delta \geq 0.05$  compounds exhibit a metal- insulator transition at  $T_c$ . A tentative  $\delta - T$  phase diagram has been proposed by Töpfer and Goodenough (Töpfer and Goodenough, 1997). When the cation deficiency is on only one sublattice, the oxide tends to order ferromagnetically (Arulraj *et al.*, 1996).

Lanthanum can be replaced by a magnetic rare earth ion such as praseodymium or neodymium. The pure end members  $\text{RMnO}_3$  can be classified in two groups: those where the rare earth has an ionic radius larger than holmium which crystallize in the orthorhombic Pbnm space group and the others which are hexagonal and belong to the  $\text{P6}_3\text{cm}$  group with six molecules per cell. Although the manganese ions order antiferromagnetically with Neel temperatures ranging from 30 K to 91 K, the rare-earth sublattice was not found to order above 1.5 K (Quez el-Ambrunaz, 1968). The Neel temperature of  $\text{PrMnO}_3$ , for example, is 91 K and the magnetic order is of the A type.

Wollan and Koehler (Wollan and Koehler, 1955) first studied the neutron diffraction measurements on a series of  $\text{La}_{1-x}\text{Ca}_x\text{MnO}_3$  samples. The samples showed the various antiferromagnetic and ferromagnetic kinds of behaviors,

depending upon the level of calcium doping. The different magnetic structures they observed are as shown in fig. 1.4.7. The  $\text{LaMnO}_3$  was found to be antiferromagnetic (labeled A in the fig. 1.4.7) with ferromagnetic planes that had alternating directions of magnetization. The 100% doped  $\text{CaMnO}_3$  was also found to be antiferromagnetic.  $\text{Mn}^{4+}$  ions are surrounded by the six closest neighbors having opposite spin (label G). Other doping levels gave other types of antiferromagnetic ordering, but in the doping range of  $x = 0.3$  the samples were ferromagnetic (label B).

Shiffer and coworkers (Shiffer *et al.*, 1995) studied measurements of the magnetic states of manganites as a function of temperature and doping in  $\text{La}_{1-x}\text{Ca}_x\text{MnO}_3$  ceramic samples. The CMR effect takes place at the ferromagnetic to paramagnetic transition, with a doping level approximately between 20 and 50%. The maximum Curie temperature is achieved with a doping level of around 30%. Goodenough and Loeh (Goodenough and Loeb, 1955) have explained the magnetic structures for different doping levels in terms of different types of bonding, where some bonds are ferromagnetic and others are antiferromagnetic or paramagnetic. This is determined by the relative orientation of occupied and unoccupied orbitals of the Mn-O-Mn pairs.

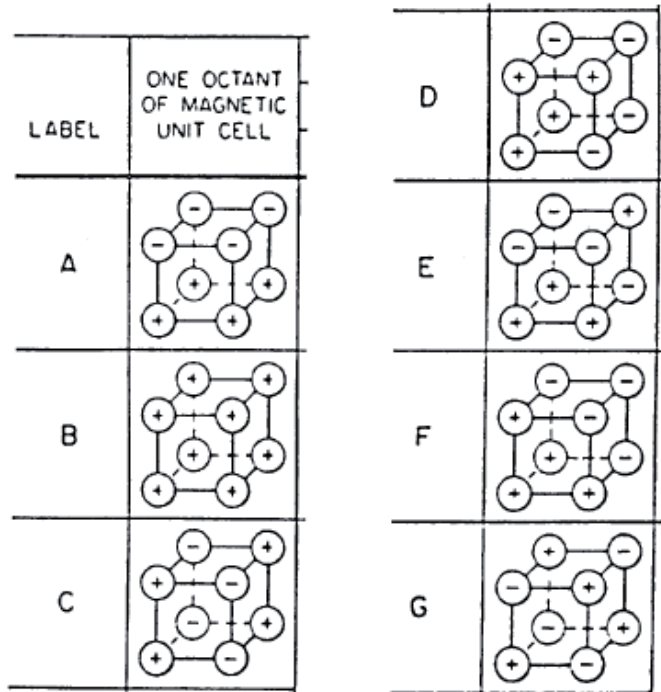


Figure 1.4.7. Possible magnetic structures of the perovskite manganites, the circle represents the Mn ion and the sign indicates the direction of the projection of the spin along z-axis (Sakhalkar, 2009)

#### *1.4.1.7. Colossal Magnetoresistance (CMR)*

Colossal magnetoresistance is a material's property which enables it to change its electrical resistance in the presence of magnetic field. A magnetic field applied to perovskite manganite in the paramagnetic semiconducting state enables its phase transformation into ferromagnetic metallic state causing colossal magnetoresistance to occur. The magnetoresistance has a peak close to position of the maximum slope of the resistivity curve. There should be a large change of resistivity with temperature to have a large magnetoresistance. Also the transition temperature should be highly sensitive to the applied field.

The double exchange phenomenon helps to explain the CMR effect. The applied magnetic field will align the  $t_{2g}$  spins and the transport will be possible between Mn ions. At the Curie temperature both spins will disorder and magnetic susceptibility will be high which maximizes the effect of applied field. In order to have a sharp transition between the metallic and insulating state, the sample should be as homogeneous as possible so that all parts have the same transition temperature. If there are polycrystalline grains, there will be regions between the grains that have different transition temperatures because the material is distorted with different Mn-O-Mn bond angles and lengths and different  $Mn^{4+}$  concentrations. The resistivity curve for the whole sample is a superposition of the resistivity curves for the different parts, and with different transition temperatures there will be a broader transition.

## 2. AIMS OF THE STUDY

The general objectives of present study were to synthesize different functional oxides in polycrystalline bulk and in thin film forms and to investigate their structural and magnetic properties for application in spintronics and multiferroics. Specifically, the aims are as follows:

- To investigate the effects of strontium substitution on the structure, magnetic transition temperatures and dielectric behaviour of  $\text{Ba}_{2-x}\text{Sr}_x\text{Mg}_2\text{Fe}_{12}\text{O}_{22}$  ( $0 \leq x \leq 2$ ) hexaferrites, prepared by chemical solution method.
- Investigation of room-temperature ferromagnetism in Ca and Mg stabilized zirconia bulk samples and thin films.
- To deposit  $\text{LaMnO}_3$  thin films by atomic layer deposition (ALD) and investigate their structural, microstructural and magnetic properties.

### 3. EXPERIMENTAL

More detailed descriptions of the samples and experimental parameters are available in the publications (appendix). The following sections are provided to make the experimental process more accessible.

#### 3.1. Synthesis of samples

##### 3.1.1. Polycrystalline powder samples of Y-type ( $Ba_{2-x}Sr_xMg_2Fe_{12}O_{22}$ ) hexaferrites

Polycrystalline samples of  $Ba_{2-x}Sr_xMg_2Fe_{12}O_{22}$  (with  $x = 0, 0.5, 1, 1.5,$  and  $2$ ) were prepared by chemical citrate solution method. Initially, the aqueous solutions (0.5 M) of  $Ba(NO_3)_2$ ,  $SrCO_3$ ,  $MgO$ ,  $Fe(NO_3)_3 \cdot 9H_2O$ , and citric acid were prepared separately in deionised water. These solutions were mixed and the pH of the resulting solution was made neutral or slightly alkaline (pH = 7–8) by adding ammonia solution. Mixed solution was heated on hot plate with constant stirring until auto-combustion. The resulting powders were heated at 500 °C for 3 h to remove the organic impurities. The powders were pressed in disc shape pellets and sintered at 1200 °C for 5h in air.

##### 3.1.2.1. Polycrystalline powder samples of $Zr_{1-x}Ca_xO_2$ and $Zr_{0.86}Mg_{0.14}O_2$

Polycrystalline powders of  $Zr_{1-x}Ca_xO_2$  ( $x = 0$  and  $0.16$ ) and  $Zr_{0.86}Mg_{0.14}O_2$  were prepared by the chemical citrate combustion route. Zirconyl oxychloride ( $ZrOCl_2 \cdot 8H_2O$ ), CaO and MgO were used as starting materials. 0.5 M solutions were prepared in deionized water for zirconium salt, whereas CaO and MgO were dissolved in excess of nitric acid and peroxide. Citric acid was added in 3 : 2 proportions for every cation. The resulting solution after mixing was first heated at 60 °C for 2 h and later at 80 °C until the complete evaporation of solvents. All our as-prepared powders were calcined at 800 °C in air for 5 h. To see the effects of annealing in other environments than air, the as-prepared powder samples were alternatively calcined in argon/hydrogen environments at 800 °C/ 5 h. The calcined powders were pressed to disc-shaped pellets and sintered in air at either 1200 or 1500 °C for 3 h, to investigate the dependence of structural and magnetic properties on sintering temperatures.

##### 3.1.2.2. $Zr_{1-x}Ca_xO_2$ thin films prepared by pulsed laser deposition

Thin films of 16 at% calcium-doped  $ZrO_2$  were deposited on  $10 \times 10$  mm Si (1 0 0)/ $SiO_2$  (25 nm thermal oxide) substrates by the pulsed laser deposition (PLD) technique. The substrates were ultrasonically cleaned in an acetone bath prior to the deposition process. Pellets that were used as PLD targets were sintered at 1200 °C for 5 h. A KrF excimer laser (COMPexPro 205, Coherent, wavelength

248 nm, pulse width 25 ns) was used for ablation. The deposition conditions of the  $Zr_{1-x}Ca_xO_2$  films were as follows: laser pulse energy density on the target  $2 \text{ J cm}^{-2}$ , repetition rate of laser 5 Hz, substrate temperature  $800 \text{ }^\circ\text{C}$ , the distance between the substrate and the target 7.5 cm. Ca-doped  $ZrO_2$  thin films were deposited at three different oxygen pressures in the chamber during the film growth:  $10^{-2}$ ,  $10^{-3}$  and  $10^{-4}$  mbar. The number of laser impulses for growing each film were 30000 and the resulting thicknesses of the films were  $\sim 150 \text{ nm}$ .

### 3.1.3.1. *LaMnO<sub>3</sub> thin films prepared by atomic layer deposition*

Thin films of  $LaMnO_3$  (LMO) were grown in a commercial flow-type ALD reactor (F-120 by ASM Microchemistry Ltd.) under a pressure of 2-3 mbar. Freshly synthesized  $La(thd)_3$  and  $Mn(thd)_3$  (thd=2,2,6,6-tetramethylheptane-3,5-dionate) were used as precursors. The precursors were prepared by the method described in refs (Eisentraut and Sievers, 1956; Hammond *et al.*, 1963) and then purified by a sublimation process. Ozone ( $O_3$ ), used as the oxidizer, was generated from oxygen (>99.999%) in an ozone generator (Fischer model 502). Nitrogen (>99.999%) was used as a carrier and purging gas. The pulsing period for the lanthanum and manganese precursors was 2 s, whereas the  $N_2$  purging period was 2.5 s. Ozone was pulsed for 1.2 s followed by  $N_2$  purging for 2.5 s. For the deposition of films, each ALD cycle had the pulsing sequences, *i.e.* first  $La(thd)_3$ , then  $O_3$ , followed by  $Mn(thd)_3$  and finally  $O_3$  again. These films were deposited on single-crystal substrates of Si (1 0 0) at the deposition temperature  $330 \text{ }^\circ\text{C}$  with different number of deposition cycles and were labelled as LM1300 (for 1300 deposition cycles), LM1000 (for 1000 deposition cycles) and LM900 (for 900 deposition cycles). The composition of La and Mn in thin films was measured by an X-ray fluorescence (XRF) spectrometer (Philips PW 1480 WDS) using Rh excitation. These XRF data were analyzed with the UniQuant software. The as-deposited films were annealed after deposition in a rapid thermal annealing (RTA) furnace PEO 601 (ATV Technologie GmbH) in  $N_2$  and/or  $O_2$  atmosphere at temperatures ranging between  $600$  and  $900 \text{ }^\circ\text{C}$ . The thicknesses of the  $LaMnO_3$  films were determined by X-ray reflectivity (XRR) using Panalytical X'Pert Pro MPD Alpha-1 powder diffractometer with  $Cu K\alpha$  radiation.

### 3.1.3.2. *Polycrystalline powder samples of LaMnO<sub>3</sub>*

Polycrystalline bulk samples of LMO were synthesized by chemical citrate solution method.  $La_2O_3$  and  $MnO_2$  were used as starting materials, and their aqueous solutions (0.5 M) with nitric acid and deionized (DI) water were prepared separately. Citric acid solution (0.5 M) was also prepared using DI water. These solutions were mixed, and the pH of the resulting solution was made neutral or slightly alkaline (pH = 7 – 8) by adding ammonia solution. The mixed solution was heated on a hot plate at around  $80 \text{ }^\circ\text{C}$  with constant stirring, until auto-combustion. The resulting fluffy powders were calcined at  $600 \text{ }^\circ\text{C}$  for

2 hours for the LMO crystalline phase formation and removing the organic impurities. The calcined powders were uniaxially pressed in disc shape pellets and sintered at 1300 °C for 3 hours in air.

## **3.2. Characterization techniques**

### *3.2.1. X-ray diffraction*

The x-ray diffraction measurements on polycrystalline powder samples of  $\text{Ba}_{2-x}\text{Sr}_x\text{Mg}_2\text{Fe}_{12}\text{O}_{22}$  hexaferrites was carried out using a Philips X-ray diffractometer. The X-ray diffraction technique (Rigaku Ultima IV) was used for structural identification of  $\text{Zr}_{1-x}\text{Ca}_x\text{O}_2$  and  $\text{Zr}_{0.86}\text{Mg}_{0.14}\text{O}_2$  thin film and bulk samples. The X-ray diffraction of LMO samples was carried out using a Philips X-ray diffractometer for the bulk powder samples and Panalytical X'Pert Pro diffractometer with Cu  $K\alpha$  radiation for thin films. All x-ray diffraction measurements were done at room temperature.

### *3.2.2. Raman spectroscopy*

Raman spectroscopy was performed at room temperature for structural identification of hexaferrite samples ( $\text{Ba}_{2-x}\text{Sr}_x\text{Mg}_2\text{Fe}_{12}\text{O}_{22}$ ),  $\text{Zr}_{1-x}\text{Ca}_x\text{O}_2$ ,  $\text{Zr}_{0.86}\text{Mg}_{0.14}\text{O}_2$  and LMO thin films as well as bulk samples by using Raman spectrometer (Horiba Jobin Yvon Labram HR 800).

### *3.2.3. SEM micrographs and EDX spectra*

Scanning electron microscopy (SEM) and Energy dispersive spectroscopic (EDS or EDX) measurements carried out on the undoped and doped zirconia samples sintered at different temperatures, using a Zeiss EVO-MA15 apparatus.

### *3.2.4. Magnetic measurements*

Vibrating sample magnetometer (VSM, Quantum Design's 14T – PPMS) was used to measure the magnetic susceptibility (/magnetization) and hysteresis loops of the all samples ( $\text{Ba}_{2-x}\text{Sr}_x\text{Mg}_2\text{Fe}_{12}\text{O}_{22}$  hexaferrites samples,  $\text{Zr}_{1-x}\text{Ca}_x\text{O}_2$  and  $\text{Zr}_{0.86}\text{Mg}_{0.14}\text{O}_2$  thin film and bulk samples and LMO thin film and bulk samples). The temperature dependence of magnetization was measured in a broad temperature range, 10 – 850 K for Y-type hexaferrite samples and 10 – 350 K for LMO samples in an applied magnetic field of 0.1 T. Magnetic hysteresis loops were measured at different temperatures, 10 – 400 K for  $\text{Ba}_{2-x}\text{Sr}_x\text{Mg}_2\text{Fe}_{12}\text{O}_{22}$  hexaferrites, 300 K for  $\text{Zr}_{1-x}\text{Ca}_x\text{O}_2$  ( $x= 0, 0.16$ ) and  $\text{Zr}_{0.86}\text{Mg}_{0.14}\text{O}_2$  and 10 – 300 K for  $\text{LaMnO}_3$  samples.

### 3.2.5. NMR measurements

The solid state NMR ( $^{57}\text{Fe}$ ) spectrum of  $\text{Ba}_2\text{Mg}_2\text{Fe}_{12}\text{O}_{22}$  sample was measured using the Fourier transform spin echo technique on Bruker AVANCE II NMR spectrometer. The spectra were recorded at  $T = 5$  K in zero external field, because the signal was noisy and weak at room temperature. The excitation frequency was varied from 69 to 77 MHz in steps of 0.1 MHz to cover the full broad spectral range of lines corresponding to different typical crystallographic iron sites in hexaferrites.

### 3.2.6. Dielectric measurements

Dielectric measurements were performed on disk shape pellets of  $\text{Ba}_{2-x}\text{Sr}_x\text{Mg}_2\text{Fe}_{12}\text{O}_{22}$  ( $x = 0, 0.5, 1, 1.5$ ) samples coated with silver electrodes. The temperature dependence of the dielectric permittivity and loss was measured at various frequencies from 1 to 100 kHz using a precision LCR meter (Agilent, 4284A) connected to a high temperature tube furnace.

### 3.2.7. Atomic force microscopy (AFM) and magnetic force microscopy (MFM)

The LMO thin films morphology at room temperature was evaluated by a scanning atomic force microscope (AFM, Veeco DIMENSION edge) in the area ( $0.5 \times 0.5 \mu\text{m}^2$ ) with resolution of 1024 lines, whereas NanoScan PPMS - AFM was used for magnetic force microscopy (MFM) on these thin films at 65 K and in zero magnetic fields.

## 4. RESULTS AND DISCUSSION

The results on various samples synthesized in this work are presented and discussed in this section. Structural and microstructural results are given in section 4.1, whereas magnetic results are discussed in section 4.2. Section 4.3 discusses the dielectric studies on hexaferrite samples.

### 4.1. Structural and Microstructural Studies

#### 4.1.1. Phase identification of Y-type $Ba_{2-x}Sr_xMg_2Fe_{12}O_{22}$ samples

The XRD patterns of the  $Ba_{2-x}Sr_xMg_2Fe_{12}O_{22}$  powder samples calcined at 1200 °C/5 h is shown in fig. 4.1.1. The x-ray diffractograms reveal that samples  $Ba_{2-x}Sr_xMg_2Fe_{12}O_{22}$  (with  $x = 0, 0.5, 1, 1.5$ ) have pure Y-type hexagonal structure, whereas  $Sr_2Mg_2Fe_{12}O_{22}$  ( $x = 2$ ) does not exhibit single phase Y-type structure and was therefore not examined in detail in the present study. This is consistent with previous structural studies on  $Zn_2Y$  hexaferrites (Bai *et al.*, 2005), where the maximum solubility of strontium in the  $Ba_{2-x}Sr_xZn_2Fe_{12}O_{22}$  ferrite was found to be about 1.8 and complete substitution of  $Ba^{2+}$  by  $Sr^{2+}$  prevented the Y-type phase formation.

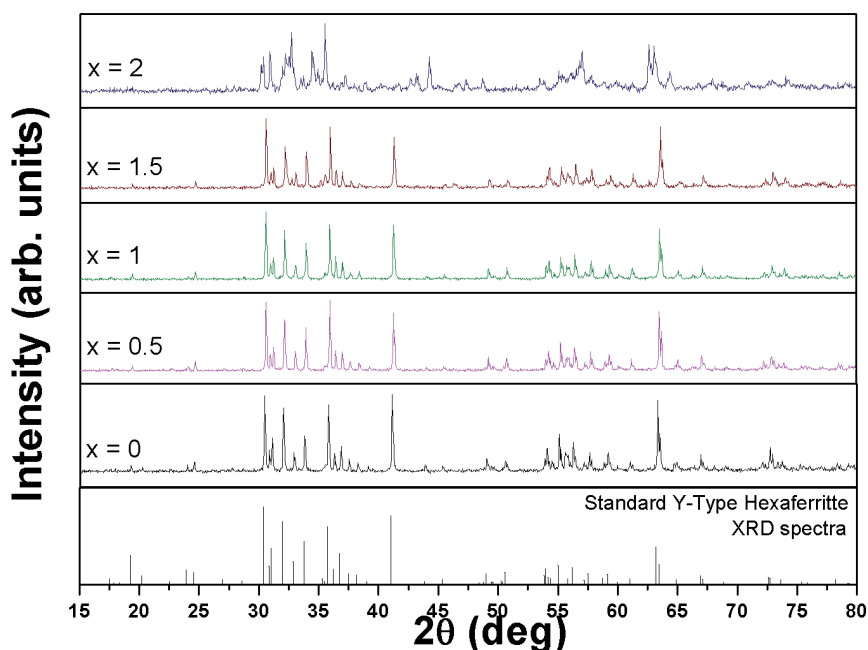


Figure 4.1.1. X-ray diffraction patterns of  $Ba_{2-x}Sr_xMg_2Fe_{12}O_{22}$  powder samples

Lattice parameters of  $\text{Ba}_{2-x}\text{Sr}_x\text{Mg}_2\text{Fe}_{12}\text{O}_{22}$  (with  $x = 0, 0.5, 1, 1.5$ ) calculated and listed in table 4.1.1 confirmed Y-type hexaferrite phase. The value of lattice parameter “a” decreased with the rise of Sr content, since the ionic radius of  $\text{Sr}^{2+}$  (1.32 Å) is smaller compared to  $\text{Ba}^{2+}$  (1.49 Å). The c/a ratio increased with increasing strontium content.

Table 4.1.1. Lattice parameters for different Sr concentration in the  $\text{Ba}_{2-x}\text{Sr}_x\text{Mg}_2\text{Fe}_{12}\text{O}_{22}$  samples (with estimated errors)

Value of x in $\text{Ba}_{2-x}\text{Sr}_x\text{Mg}_2\text{Fe}_{12}\text{O}_{22}$	a (Å) (1%)	c (Å) (0.5%)	c/a
0	5.866	43.2683	7.376
0.5	5.8548	43.3514	7.404
1	5.8436	43.2799	7.406
1.5	5.8436	43.2799	7.406

The Raman spectra measured at room temperature in fig. 4.1.2 also confirm that  $\text{Ba}_{2-x}\text{Sr}_x\text{Mg}_2\text{Fe}_{12}\text{O}_{22}$  samples exhibit a hexaferrite structure (Zhao *et al.*, 2008; Braun, 1957; Chen *et al.*, 2000; Kreisel *et al.*, 1998). In our knowledge, there are not many Raman studies on Y-type hexaferrites, except a recent publication on  $\text{Zn}_2\text{Y}$  hexaferrite (Kamba *et al.*, 2010). Raman peaks become broader with the increase of the value of x from 0 to 1.5 (fig. 4.1.2).

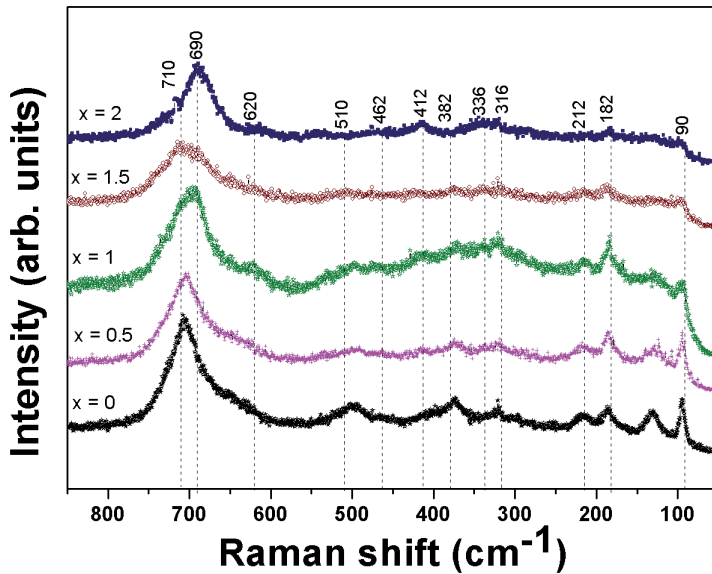


Figure 4.1.2. Raman spectra of  $\text{Ba}_{2-x}\text{Sr}_x\text{Mg}_2\text{Fe}_{12}\text{O}_{22}$  bulk samples

Changes in chemical composition, atomic radii, valence, bond length, cell size, and magnetic order might lead to the broadening of Raman peaks (Kreisel *et al.*, 1999). In our samples, peak broadening may be related to changes in magnetic structure on strontium substitution.

#### 4.1.2. Phase identification of $Zr_{1-x}Ca_xO_2$ ( $x = 0$ and $0.16$ ) and $Zr_{0.86}Mg_{0.14}O_2$ samples

X-ray diffraction patterns for the undoped as well as Ca- and Mg-doped  $ZrO_2$  bulk samples, heated at different temperatures are shown in fig. 4.1.3 (a). From these diffractograms we see that 16 at% Ca- and 14 at% Mg-doped  $ZrO_2$  samples sintered at 1500 °C exhibit a pure cubic (C) zirconia phase. The undoped sample sintered at 800 °C shows a monoclinic structure with an extra peak of tetragonal zirconia, whereas a single-phase monoclinic structure is exhibited by the sample sintered at 1500 °C. The lower, 10 at% Ca-doped zirconia sample shows a mixed cubic and tetragonal (T) structure, the presence of the tetragonal structure in this sample is also confirmed by the Raman spectra (figure not included). Figure 4.1.3 (b) shows the diffractograms for the PLD thin films of the 16 at% Ca-doped  $ZrO_2$ , grown at different oxygen partial pressures. The films show one XRD peak for cubic zirconia (1 1 1) and other intense peaks from the silicon substrate.

Raman spectra (see fig. 4.1.4 (b)) also confirm the cubic phase formation for thin films showing a characteristic cubic XRD pattern. Raman spectra measured at room temperature for the bulk and thin film samples of doped zirconia are shown in figs. 4.1.4 (a) and (b). The spectrum for 16 at% Ca-doped  $ZrO_2$  sintered sample at 1500 °C (fig. 4.1.4 (a)) validates the cubic phase formation (Raman peaks around 275, 410, 520 and 580  $cm^{-1}$ ) (Morell *et al.*, 1997), whereas the peaks are not separable for both Ca and Mg stabilized zirconia samples heated at 800 °C. These broad and flat spectra may be related to the mixed zirconia phases at 800 °C, although XRD could show single phase for those powders. Usually, the strongest Raman peak position is around 615  $cm^{-1}$  for yttria-stabilized zirconia samples (Morell *et al.*, 1997), but for Ca-stabilized zirconia this shifts towards lower values, and it is around 580  $cm^{-1}$  in our sample. This shift may be because of the difference in sizes and mass of Ca and Zr, as compared with Y and Zr (Morell *et al.*, 1997). Raman spectra for the PLD thin films of 16% Ca-doped  $ZrO_2$  demonstrate characteristic peaks of cubic zirconia (155, 425, 620  $cm^{-1}$ ), the strong peaks due to the silicon substrate (near 300 and 530  $cm^{-1}$ ) can also be seen in the spectra that suppress the intensity of zirconia modes. Our results are consistent with another Raman study by Gazzoli *et al* (Gazzoli *et al.*, 2007), which showed that above 14% calcium doping stabilizes the cubic zirconia phase and below this doping concentration it results in a tetragonal structure, we have also observed the Raman spectra resembling the tetragonal structure for 10 at%  $Ca^{2+}$  in  $ZrO_2$  (figure not included).

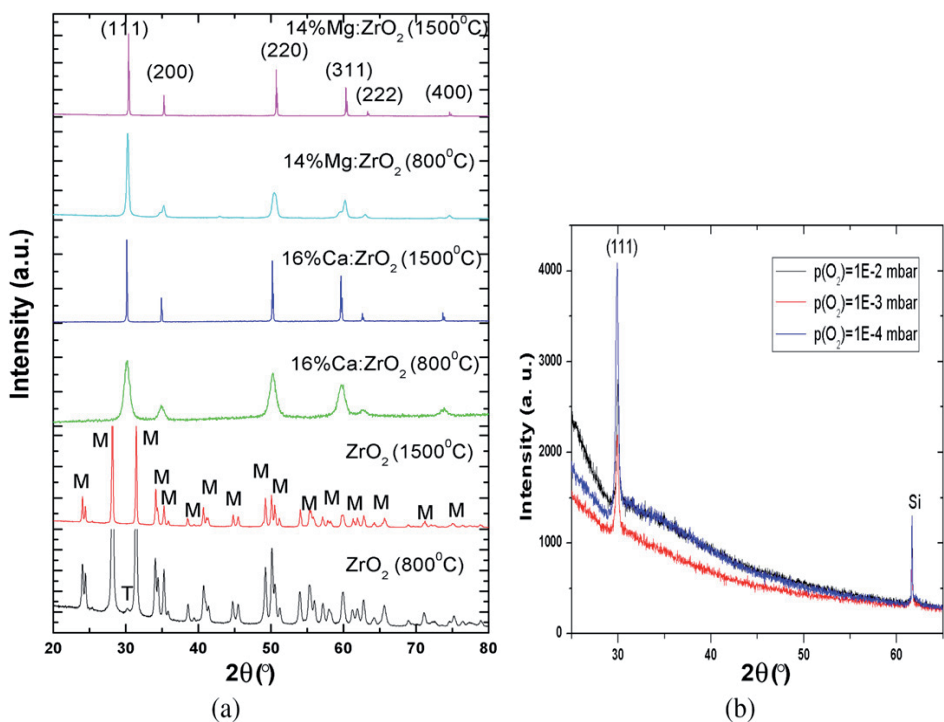


Figure 4.1.3. XRD patterns of (a) bulk powders heat-treated at different temperatures, (b) 16% Ca-doped ZrO<sub>2</sub> thin films deposited at various oxygen partial pressures

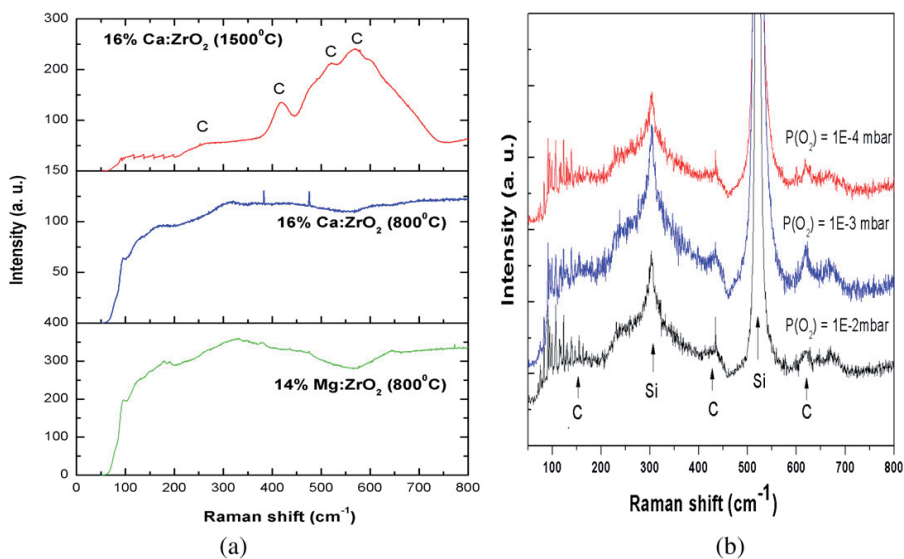


Figure 4.1.4. Room-temperature Raman spectra of (a) bulk samples of doped ZrO<sub>2</sub>, (b) Zr<sub>0.84</sub>Ca<sub>0.16</sub>O<sub>2</sub> thin films

SEM micrographs and EDX spectra of the undoped and doped zirconia samples sintered at different temperatures are shown in fig. 4.1.5. The EDX spectra reveal that the chemical compositions are in good agreement with the desired stoichiometry, and there are no impurities in the prepared samples. From the SEM images we can visualize that all those samples have grains in the micrometre ( $\mu\text{m}$ ) range, however, the grains are smaller ( $\sim 2\text{--}5\mu\text{m}$ ) for the samples treated at  $800^\circ\text{C}$  and the undoped sintered sample at  $1500^\circ\text{C}$ , whereas the grains are in the range  $3\text{--}8\mu\text{m}$  for the doped sintered samples at  $1500^\circ\text{C}$ .

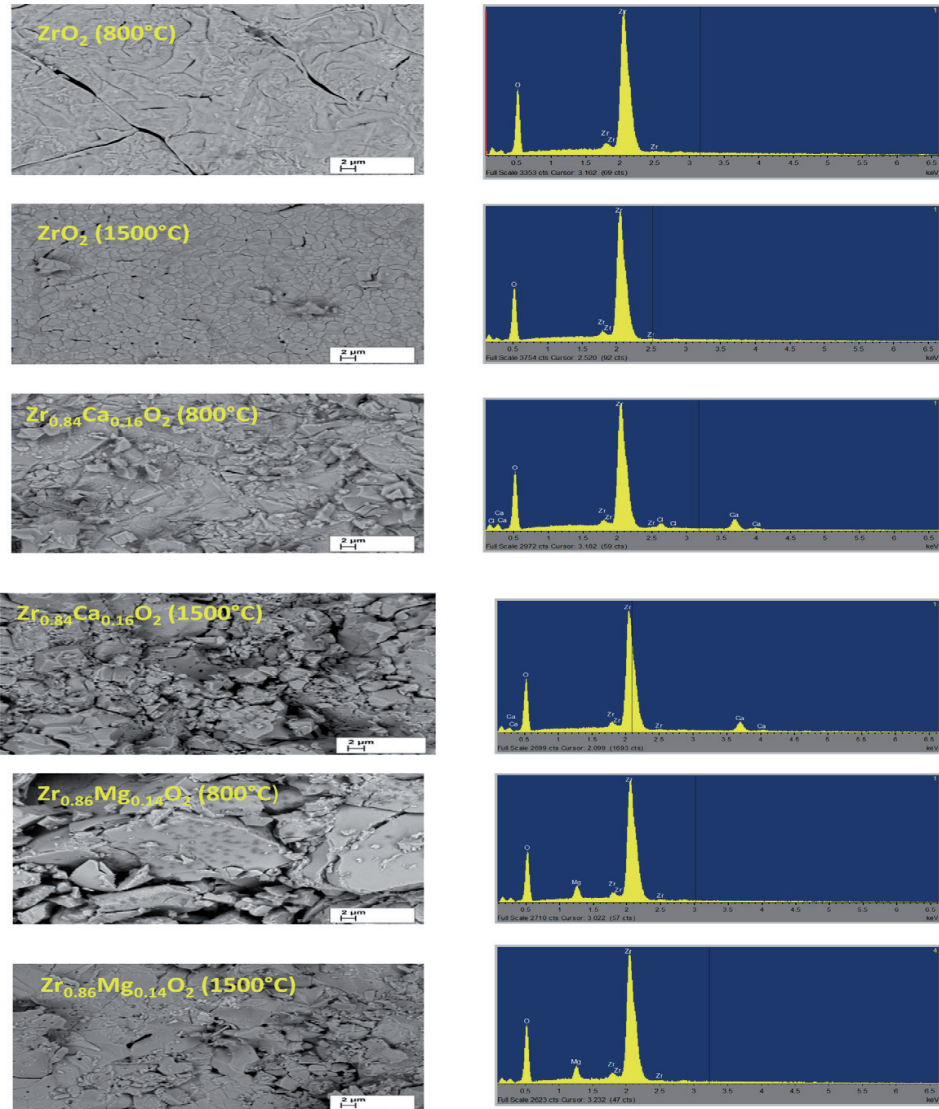


Figure 4.1.5. SEM micrographs and EDX spectra of the undoped and doped zirconia samples

#### 4.1.3.1. Phase identification of $\text{LaMnO}_3$ samples

X-ray reflectivity (XRR) results reveal that the thicknesses of our as-deposited LMO thin films with 1300 (LM1300), 1000 (LM1000) and 900 (LM900) deposition cycles were about 104 nm, 95 nm and 78 nm, respectively, with experimental errors around  $\pm 5\%$ . The thicknesses are correlated to the number of deposition cycles as expected increasing with increasing number of deposition cycles such that the growth per cycle (GPC) could be calculated to be roughly  $0.9 \text{ \AA} / \text{cycle}$ . The small deviation from the perfectly linear dependence of the film thickness on the number of cycles is most probably due to minor changes in the reactor configuration.

The dependence of crystal structure on the annealing temperature is illustrated in fig. 4.1.6 (a) where XRD patterns for variously annealed LM1300 thin films are shown. These XRD patterns infer that as-deposited films and the films annealed at  $600^\circ\text{C}$  are amorphous, films annealed at  $700^\circ\text{C}$  and  $800^\circ\text{C}$  have the single-phase perovskite structure, whereas the films annealed at  $900^\circ\text{C}$  are not of the single-phase anymore. In further sections we will only discuss the results for single phase crystalline films (i.e. thin films treated at  $700^\circ\text{C}$  and  $800^\circ\text{C}$ ).

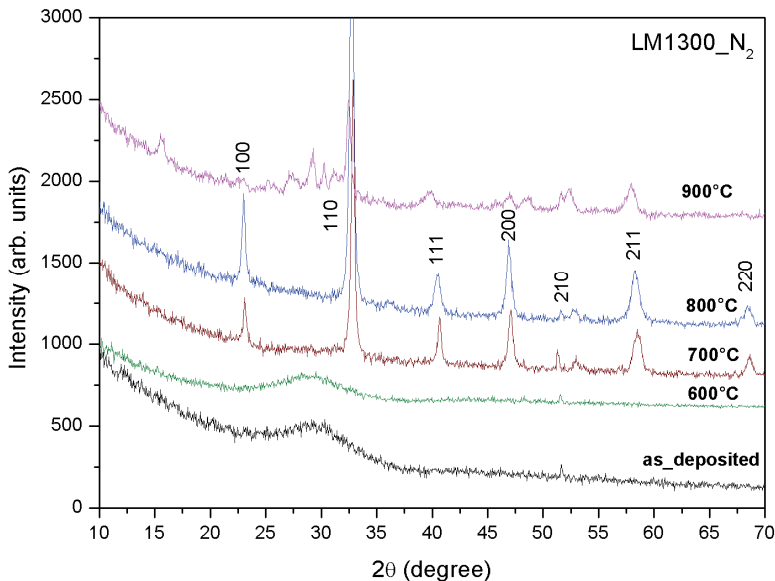


Figure 4.1.6. (a) X-ray diffraction patterns for LM1300 thin films (as deposited and annealed at different temperatures in  $\text{N}_2$  atmosphere)

Figure 4.1.6 (b) shows the XRD patterns for thin films LM1300, LM1000 and LM900 annealed at  $700^\circ\text{C}$  and  $800^\circ\text{C}$  in different atmospheres ( $\text{N}_2$  and  $\text{O}_2$ ). It can

be seen that all these films exhibit a single-phase perovskite-type lanthanum manganite structure (Shimizu and Murata, 1997). The crystal structure is rhombohedral with space group R-3c. Even though determination of small variations in lattice parameters for thin-film samples is somewhat ambiguous we could see that the unit-cell volume for LM1300 thin films increased (from 344.81 to 349.75 Å<sup>3</sup>) with annealing temperature increasing from 700 to 800 °C in N<sub>2</sub>, apparently due to decreasing oxygen content (or oxygen-to-cation ratio). Also seen was that the unit-cell volume for LM1000 thin films annealed at 800 °C depended on the annealing atmosphere (N<sub>2</sub> or O<sub>2</sub>), being larger in case of N<sub>2</sub> (349.91 Å<sup>3</sup>) than in O<sub>2</sub> (342.69 Å<sup>3</sup>) as expected (listed in table 4.1.2).

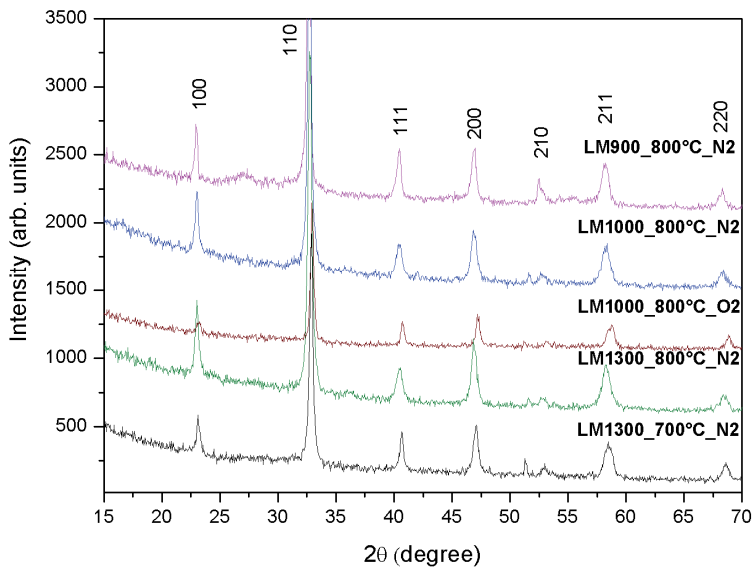


Figure 4.1.6. (b) X-ray diffraction patterns for LMO thin films (LM1300, LM1000 and LM900) annealed at different temperatures in N<sub>2</sub> and O<sub>2</sub> atmospheres

X-ray diffraction patterns of bulk LMO samples sintered at 600 and 1300 °C in air are shown in fig. 4.1.6 (c). These samples also exhibit the single-phase perovskite crystal structure with rhombohedral symmetry. The unit cell volume (table 4.1.2) decreased with increase in annealing temperature (600 to 1300 °C), which could be the effect of change in oxygen content (decrease of oxygen deficiencies) at higher temperature (Ni *et al.*, 2011) and increase in non-stoichiometry. The XRD peaks become sharper and more intense with the increase of the annealing temperature, which indicates the increase in grain size and better crystallinity (Wang *et al.*, 2010).

Table 4.1.2. Unit cell volume, strain and crystallite sizes of LMO thin films and bulk samples calculated from XRD

Sample	Strain (%)	Average crystallite size (nm)	Unit Cell volume (Angstroms <sup>3</sup> )
LM1300 700°C N <sub>2</sub>	0.394	27	344.81
LM1300 800°C N <sub>2</sub>	0.023	34	349.75
LM1000 800°C O <sub>2</sub>	0.150	25	342.69
LM1000 800°C N <sub>2</sub>	0.164	22	349.91
LM900 800°C N <sub>2</sub>	0.132	17	348.23
LaMnO <sub>3</sub> Bulk 600°C	0.237	40	354.64
LaMnO <sub>3</sub> Bulk 1300°C	0.044	1000	353.67

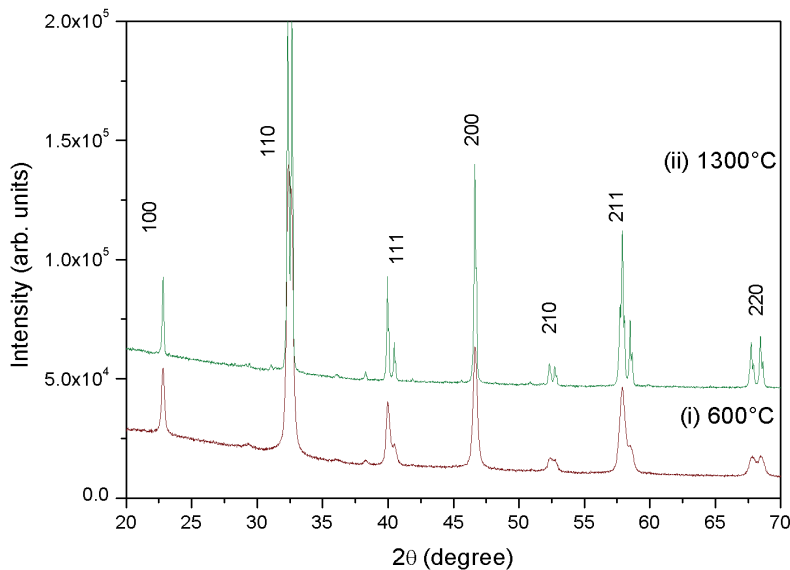


Figure 4.1.6. (c) X-ray diffraction spectra of LMO bulk powder samples annealed at 600°C/2 h and 1300°C/3 h in air

Figure 4.1.7 (a) shows Raman spectra for LMO thin films (LM1300, LM1000, and LM900) annealed at 800 °C in N<sub>2</sub> and O<sub>2</sub> atmospheres. All spectra closely resemble those previously reported for rhombohedral LaMnO<sub>3</sub> at room temperature (Iliev *et al.*, 2001), showing peaks around 217, 323, 427, 497 and 618 cm<sup>-1</sup>, although the peaks around 323 and 497 cm<sup>-1</sup> are not very clear because of the strong signals from silicon substrate around 300 and 520 cm<sup>-1</sup>.

The exact positions of the peaks at 217, 497 and 618  $\text{cm}^{-1}$  are sample-sensitive and vary within 15 – 20  $\text{cm}^{-1}$  in the spectra of polycrystalline samples (Abrashov *et al.*, 1999; Zhizhin *et al.*, 1984). The peaks around 500 and 600  $\text{cm}^{-1}$  are consistent with other studies, being usually ascribed to bending (B) and stretching (S) modes of the  $\text{MnO}_6$  octahedron, respectively (Aruta *et al.*, 2006; Iliev *et al.*, 2001). The spectra for LM1000 films annealed at 800  $^\circ\text{C}$  in  $\text{N}_2$  and  $\text{O}_2$  (see fig. 4.1.7 (a)) confirm their rhombohedral structure, however the peaks are broader for the film annealed in  $\text{O}_2$ , which also indicates the more stoichiometric oxygen-to-cation ratio in the case of the film annealed in  $\text{N}_2$  atmosphere.

The Raman spectra of bulk LMO samples sintered at 600 and 1300  $^\circ\text{C}$  are shown in fig. 4.1.7 (b). Although the peaks are broader due to rough surfaces of bulk samples, they are observable around 179, 217, 323, 427, 497, 618 and 640  $\text{cm}^{-1}$ , confirming the rhombohedral structure in these samples too (Ni *et al.*, 2011; Wang *et al.*, 2010).

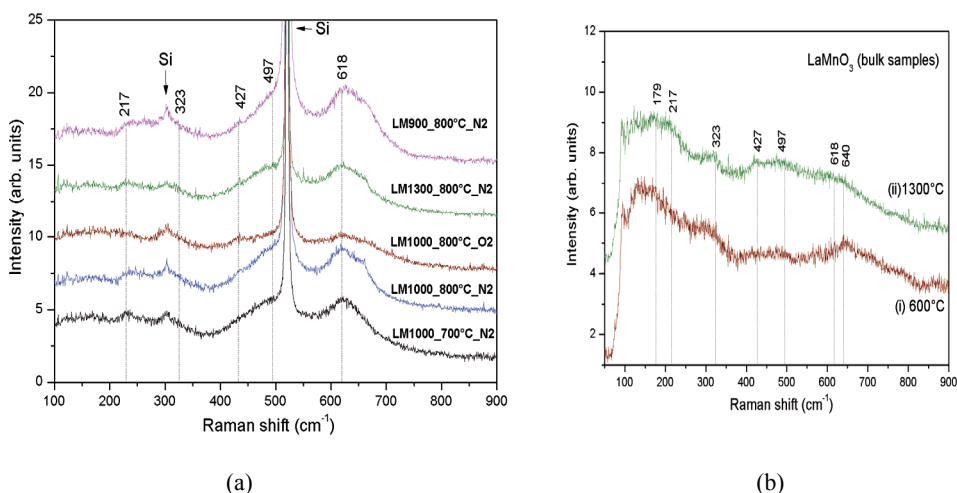


Figure 4.1.7. Raman spectra measured at room temperature: (a) LM1300, LM1000 and LM900 thin films annealed at different temperature in  $\text{N}_2$  and  $\text{O}_2$  atmospheres, (b) Bulk LMO sample annealed at 600 and 1300 $^\circ\text{C}$  in air

#### 4.1.3.2. AFM Studies of $\text{LaMnO}_3$ thin films

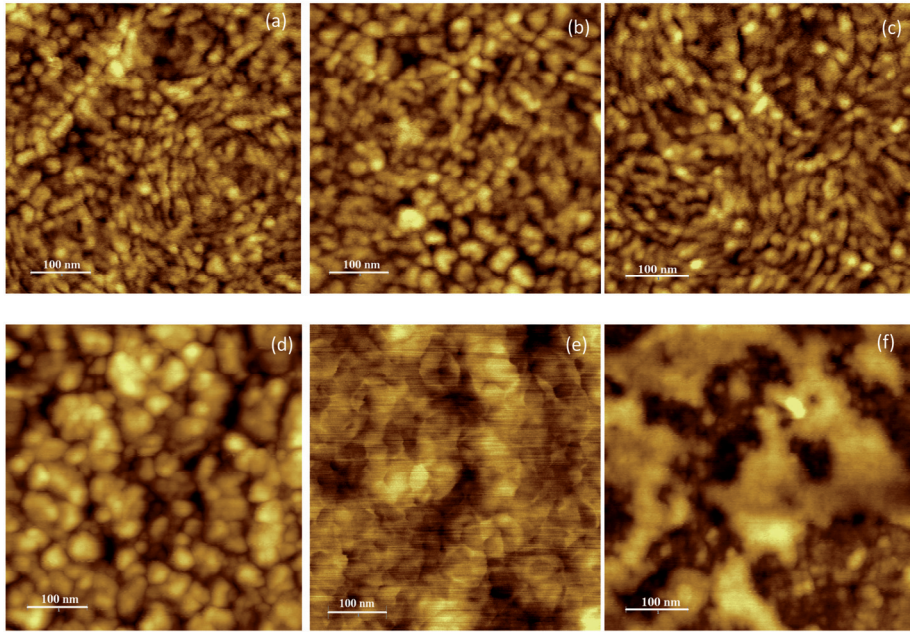


Figure 4.1.8 AFM images (scan area  $0.5 \times 0.5 \mu\text{m}^2$ ) measured under ambient conditions: (a) LM900 annealed at  $800 \text{ }^\circ\text{C}$  in  $\text{N}_2$ , (b) LM1000 annealed at  $700 \text{ }^\circ\text{C}$  in  $\text{N}_2$ , (c) LM1000 annealed at  $800 \text{ }^\circ\text{C}$  in  $\text{N}_2$ , (d) LM1000 annealed at  $800 \text{ }^\circ\text{C}$  in  $\text{O}_2$ , (e) LM1300 annealed at  $700 \text{ }^\circ\text{C}$  in  $\text{N}_2$  and (f) LM1300 annealed at  $800 \text{ }^\circ\text{C}$  in  $\text{N}_2$

Atomic force microscopy images in figs. 4.1.8 (a - f) show the uniform surface topography and microstructure of our annealed LMO thin films. Dense films are obtained by ALD as expected (Choi, 2009). Samples annealed at  $800 \text{ }^\circ\text{C}$  have larger grains (due to coalescence of small grains) than those annealed at  $700 \text{ }^\circ\text{C}$  by grain boundary diffusion, which usually causes major grain growth at high temperature heat treatments. The grain sizes estimated from AFM images are given in table 4.1.3, which shows that the grain size increases also with increasing film thickness. The surface roughness of the films was calculated from the AFM results. The values listed in table 4.1.3 reveal that the films are extremely smooth in general. Results for the LM1300 and LM1000 films annealed at different temperatures ( $700$  and  $800 \text{ }^\circ\text{C}$  in  $\text{N}_2$ ) show that the RMS roughness value is little larger for films annealed at  $800 \text{ }^\circ\text{C}$  presumably due to growth of large grains (Youssef *et al.*, 2009; Sengupta *et al.*, 2011; Liu *et al.*, 2006). The results shown in table 4.1.3 moreover suggest that the annealing atmosphere may also affect the surface morphology, as the LM1000 film annealed at  $800 \text{ }^\circ\text{C}$  in  $\text{N}_2$  atmosphere exhibit lower roughness and smaller grains compared to the same film after being annealed in  $\text{O}_2$  atmosphere, which could be the result of the increase in oxygen non-stoichiometry in the film

annealed in O<sub>2</sub>. Our AFM results and the effect of the annealing atmosphere on microstructure are consistent with other studies (Simoes *et al.*, 2009; Tsang *et al.*, 2000).

Table 4.1.3. Approximate grain sizes and RMS roughness values of LMO thin films determined by atomic force microscopy (AFM)

Thin film sample	RMS Roughness (nm) (with scanned area of 7×7 μm <sup>2</sup> )	Grain size in nm (approx. range)
LM900 annealed at 800 °C in N <sub>2</sub>	1.05	10 - 50
LM1000 annealed at 700 °C in N <sub>2</sub>	0.66	15 - 40
LM1000 annealed at 800 °C in N <sub>2</sub>	0.68	30 - 80
LM1000 annealed at 800 °C in O <sub>2</sub>	1.91	50 - 90
LM1300 annealed at 700 °C in N <sub>2</sub>	0.37	50-70
LM1300 annealed at 800 °C in N <sub>2</sub>	0.59	200-800

## 4.2. Magnetic Studies

### 4.2.1.1. Magnetic properties of Ba<sub>2-x</sub>Sr<sub>x</sub>Mg<sub>2</sub>Fe<sub>12</sub>O<sub>22</sub> samples

The magnetic phase transition temperatures in Ba<sub>2-x</sub>Sr<sub>x</sub>Mg<sub>2</sub>Fe<sub>12</sub>O<sub>22</sub> for different strontium content (x = 0, 0.5, 1, 1.5) were determined from the temperature dependence of magnetic susceptibility measured in an applied magnetic field of 0.1 T (fig. 4.2.2). The ferrimagnetic-paramagnetic transition (Curie temperature, T<sub>c</sub>) was identified as the temperature where the magnetic susceptibility significantly dropped. The two visible susceptibility peaks in correspondence of temperatures T<sub>I</sub> and T<sub>II</sub> (fig. 4.2.2) are associated with the consecutive magnetic spin transitions. Decreasing the temperature, the magnetic order changes from collinear ferrimagnetic to a proper-screw spin phase at transition temperature II, and from screw spin phase to a longitudinal conical spin phase around transition temperature I (see also fig. 4.2.1), as recently suggested for Ba<sub>2</sub>Mg<sub>2</sub>Fe<sub>12</sub>O<sub>22</sub> (x = 0) based on neutron diffraction (Ishiwata *et al.*, 2010; Sagayama *et al.*, 2009). The magnetic transition temperatures of different samples of Ba<sub>2-x</sub>Sr<sub>x</sub>Mg<sub>2</sub>Fe<sub>12</sub>O<sub>22</sub> are given in table 4.2.1. It can be seen that all the magnetic transition temperatures increase with increasing Sr content.

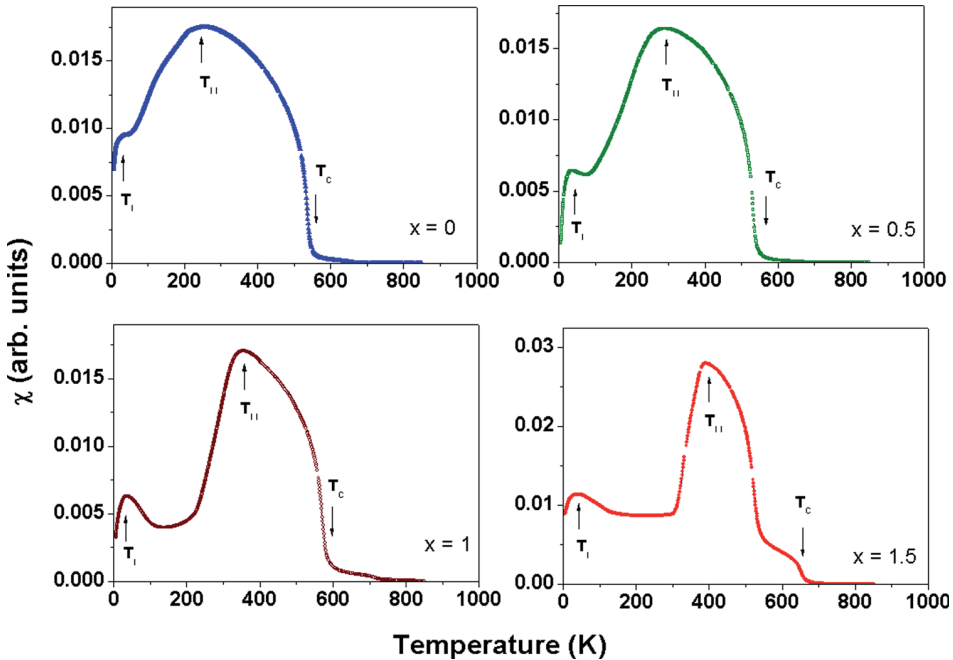
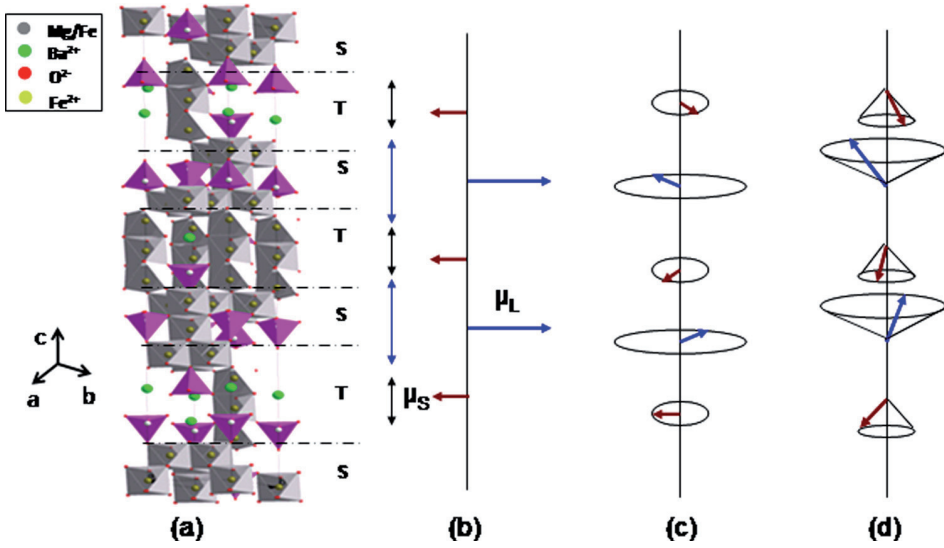


Figure 4.2.3 shows the magnetic hysteresis loops of  $\text{Ba}_{2-x}\text{Sr}_x\text{Mg}_2\text{Fe}_{12}\text{O}_{22}$  measured at 300 K for different strontium content ( $x = 0, 0.5, 1, 1.5$ ). Coercivity was found to be increased with strontium concentration (for  $x = 1.5$ , the coercivity is two times larger than in case of  $x = 0$ ). Similar behaviour in coercivity was also found by other research groups on Sr substitution in Y-type hexaferrites (Bai *et al.*, 2005; Fang *et al.*, 2008). The ground state magnetic structure of these hexaferrites  $\{(\text{BaSr})_2\text{Mg}_2\text{Fe}_{12}\text{O}_{22}, (\text{BaSr})_2\text{Zn}_2\text{Fe}_{12}\text{O}_{22}\}$  is composed of alternating stacking of the L and S blocks along the c-axis (Kimura, 2012). The magnetic moments of Fe sites lying in the ab plane are in collinear ferrimagnetic structures, within these blocks. The Sr-free sample shows the collinear ferrimagnetic order at room temperature, whereas the antiferromagnetic order increased with the increase in Sr content. The enhancement in antiferromagnetic order for higher concentration ( $x = 1.5$ ) results in increased coercivity, whereas the composition  $x = 1$  shows slight decrease in coercivity, possibly due to an intermediate phase (between proper-screw and conical spin phase) and magnetic frustrations existing at this composition. Enhancement in coercivity in antiferromagnetic phase is understandable, because it needs higher demagnetizing fields as compared to ferrimagnetic material. At room temperature,  $\text{Ba}_{2-x}\text{Sr}_x\text{Mg}_2\text{Fe}_{12}\text{O}_{22}$  samples with compositions  $x = 0$  and  $x = 0.5$  are still in collinear ferrimagnetic phase (show single ferrimagnetic loop), while samples with  $x = 1$  and  $x = 1.5$  have entered already in the screw spin phase (showed triple loops). The abnormal triple loops are related to the changes in the magnetic phases and intermediate phases produced by strontium substitution in  $\text{Ba}_{2-x}\text{Sr}_x\text{Mg}_2\text{Fe}_{12}\text{O}_{22}$  samples. Kimura *et al.* had also observed the phase change from collinear ferrimagnetic to antiferromagnetic state, with other intermediate phases, depending on Sr substitution for barium ions in  $\text{Zn}_2\text{Y}$  hexaferrites (Kimura *et al.*, 2005). Our  $\text{Ba}_{2-x}\text{Sr}_x\text{Mg}_2\text{Fe}_{12}\text{O}_{22}$  samples with higher strontium concentration ( $x = 1$  and  $1.5$ ) exhibit an intermediate magnetic phase in between proper screw spin phase and conical spin phase at room temperature. This intermediate phase could be responsible for multistage abnormal hysteresis loop. This kind of loops has been observed in  $\text{Ba}_2\text{Mg}_2\text{Fe}_{12}\text{O}_{22}$  samples (at 10 K) by Sagayama *et al.*, and they attributed it to the phase transition of the magnetic structure, which was supported by neutron diffraction studies at low temperatures (Sagayama *et al.*, 2009).

In order to study the magnetic behaviour of the different magnetic phases, magnetic hysteresis loops of  $\text{Ba}_{0.5}\text{Sr}_{1.5}\text{Mg}_2\text{Fe}_{12}\text{O}_{22}$  were measured at selected representative temperatures in the range 10 – 400 K (fig. 4.2.4). Figures 4.2.4 (a) and (b) show the magnetic hysteresis at 10 and 30 K, respectively, where the conical spin phase is exhibited. In the range 200 – 350 K, the sample has a screw spin phase and it shows triple M - H loops (figs. 4.2.4 (c – e)). At 400 K,  $\text{Ba}_{0.5}\text{Sr}_{1.5}\text{Mg}_2\text{Fe}_{12}\text{O}_{22}$  sample has collinear ferrimagnetic order and the magnetic hysteresis curve shows the typical ferrimagnetic behaviour (fig. 4.2.4 (f)).

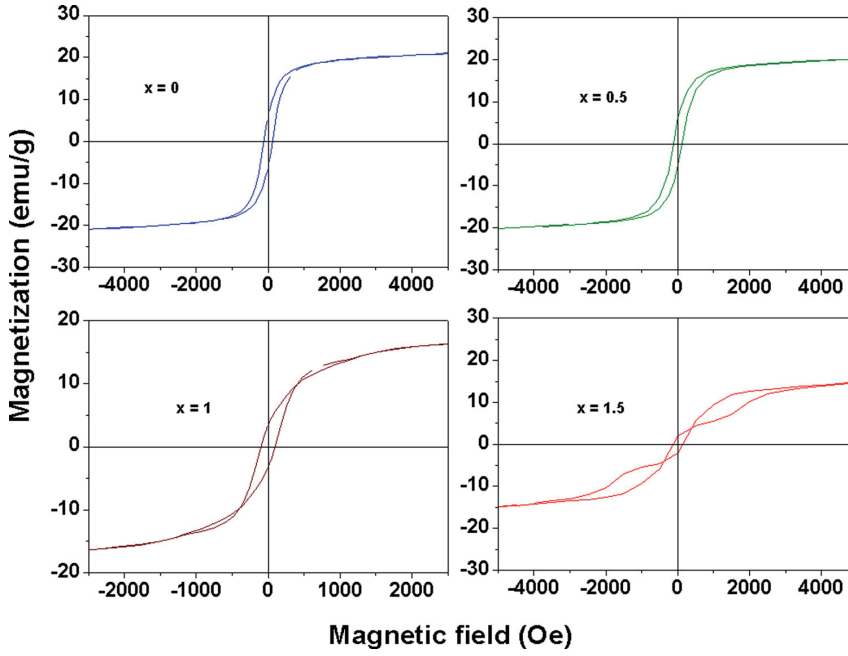


Figure 4.2.3. Hysteresis loops measured at 300K of  $\text{Ba}_{2-x}\text{Sr}_x\text{Mg}_2\text{Fe}_{12}\text{O}_{22}$  samples

Table 4.2.1. Coercivities and magnetic transition temperatures (with averaged estimated errors) of the powder samples of  $\text{Ba}_{2-x}\text{Sr}_x\text{Mg}_2\text{Fe}_{12}\text{O}_{22}$

Value of x in $\text{Ba}_{2-x}\text{Sr}_x\text{Mg}_2\text{Fe}_{12}\text{O}_{22}$	Coercivity $H_c$ (Oe)	Transition Temperatures (K)		$T_c$ (K) ( $\pm 5$ K)
		$T_I$ ( $\pm 5$ K)	$T_{II}$ ( $\pm 10$ K)	
0	100	20	260	550
0.5	150	30	290	550
1	100	35	355	590
1.5	200	40	390	670

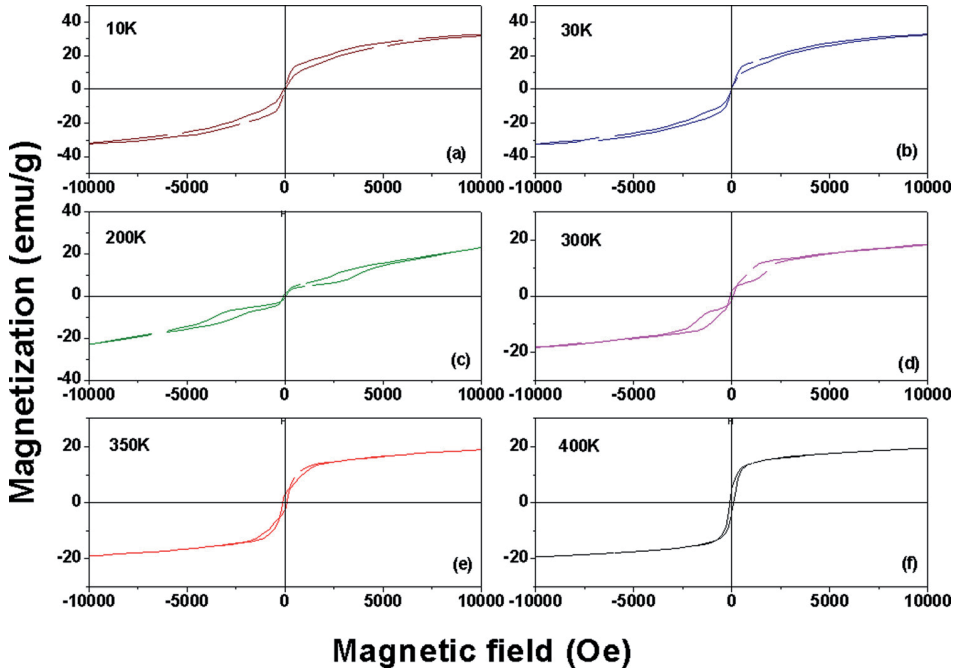


Figure 4.2.4. Hysteresis loops of the powder samples of  $\text{Ba}_{0.5}\text{Sr}_{1.5}\text{Mg}_2\text{Fe}_{12}\text{O}_{22}$  measured at (a) 10 K, (b) 30 K, (c) 200 K, (d) 300 K, (e) 350 K, and (f) 400 K

#### 4.2.1.2. NMR measurements on $\text{Ba}_2\text{Mg}_2\text{Fe}_{12}\text{O}_{22}$

The  $^{57}\text{Fe}$  NMR spectrum of  $\text{Ba}_2\text{Mg}_2\text{Fe}_{12}\text{O}_{22}$  measured at 5 K in zero applied magnetic field is shown in fig. 4.2.5. The NMR spectrum is noisy and broad, consistent with previous NMR measurements on Y-type hexaferrites. Y-type hexaferrites have six sublattice sites ( $6c_{\text{IV}}$ ,  $3a_{\text{VI}}$ ,  $18h_{\text{VI}}$ ,  $6c_{\text{VI}}$ ,  $6c_{\text{IV}}^*$ , and  $3b_{\text{VI}}$ ) (Albanese, 1977), which could not be distinguished in our NMR spectrum. In case of M-type (Streever, 1969) and U-type (Dimri *et al.*, 2011) barium hexaferrites, the NMR spectra consist of five peaks relative to the different lattice iron sites ( $12k$ ,  $4f_{\text{IV}}$ ,  $2a$ ,  $4f_{\text{VI}}$ , and  $2b$  in M-type and  $12k$ ,  $8f_{\text{IV}}$ ,  $4a$ ,  $4f_{\text{VI}}$ , and  $2b$  in U-type hexaferrites). This unresolved spectrum is probably due to a number of different crystallographic (tetrahedral and octahedral) iron sites in the Y-type structure (see fig. 4.2.1). The other reason of broadening may be related to its different magnetic order, because our Y-type hexaferrite samples are in conical spin order at this temperature (5 K), whereas M- and U-type hexaferrites are usually in collinear ferrimagnetic states at that temperature resulting in well resolved NMR spectra.

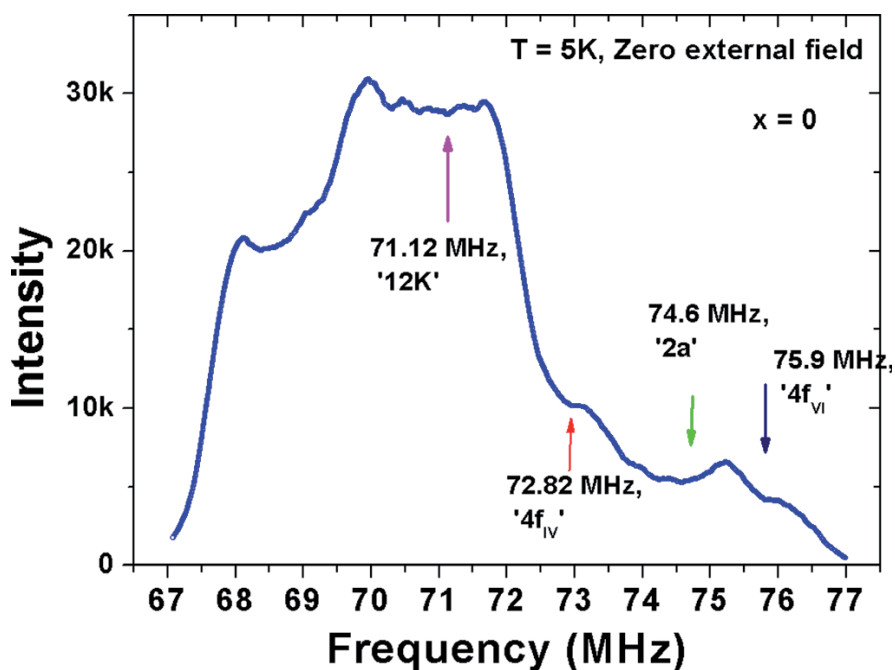


Figure 4.2.5.  $^{57}\text{Fe}$  NMR spectrum of  $\text{Ba}_2\text{Mg}_2\text{Fe}_{12}\text{O}_{22}$  ( $x = 0$ ) powder sample measured in zero field at 5 K. The expected lines of different iron sites as observed in M-type spectra are indicated by arrows at different frequencies

#### 4.2.2. Magnetic properties of $\text{Zr}_{1-x}\text{Ca}_x\text{O}_2$ ( $x = 0$ and 0.16) and $\text{Zr}_{0.86}\text{Mg}_{0.14}\text{O}_2$ samples

Hysteresis loops measured at room temperature (300 K) for the Ca- and Mg-doped and undoped  $\text{ZrO}_2$  samples heated at 800 and 1500 °C are shown in fig. 4.2.6. M – H loops of the doped zirconia samples appear like a good ferromagnet for the powders heated at 800 °C, whereas the diamagnetism is enhanced in samples sintered at higher temperatures. The enhancement of the diamagnetic signal in the sintered samples may be due to the decrease in the number of oxygen vacancies on high-temperature treatment in air. The coercivities and spontaneous magnetization (at 0.5 T) estimated from these curves are listed in table 4.2.2. There are no remarkable changes in coercivities, whereas the saturation magnetization decreases with the increase in sintering temperatures. The undoped  $\text{ZrO}_2$  samples also exhibit tiny ferromagnetic hysteresis, possibly due to the presence of some oxygen vacancies in our samples. The density of oxygen vacancies is strongly dependent on the synthesis methods (Karapetrova *et al.*, 2001). Zirconyl oxychloride was used as the zirconium precursor, so there is excess chlorine ( $\text{Cl}_2$ ) during the sintering process, which was reported in an old study (Karapetrova *et al.*, 2001), which showed that preparation by nitrate or oxychloride precursors leads to oxygen vacancies in zirconia, however the vacancies are lower in the samples prepared

by oxychloride precursors. This is confirmed from the weak ferromagnetic signal in  $M - H$  measurements (fig. 4.2.6) due to these oxygen vacancies, however, the oxygen vacancy concentration was not enough to result in long-range ferromagnetic ordering in these undoped samples.

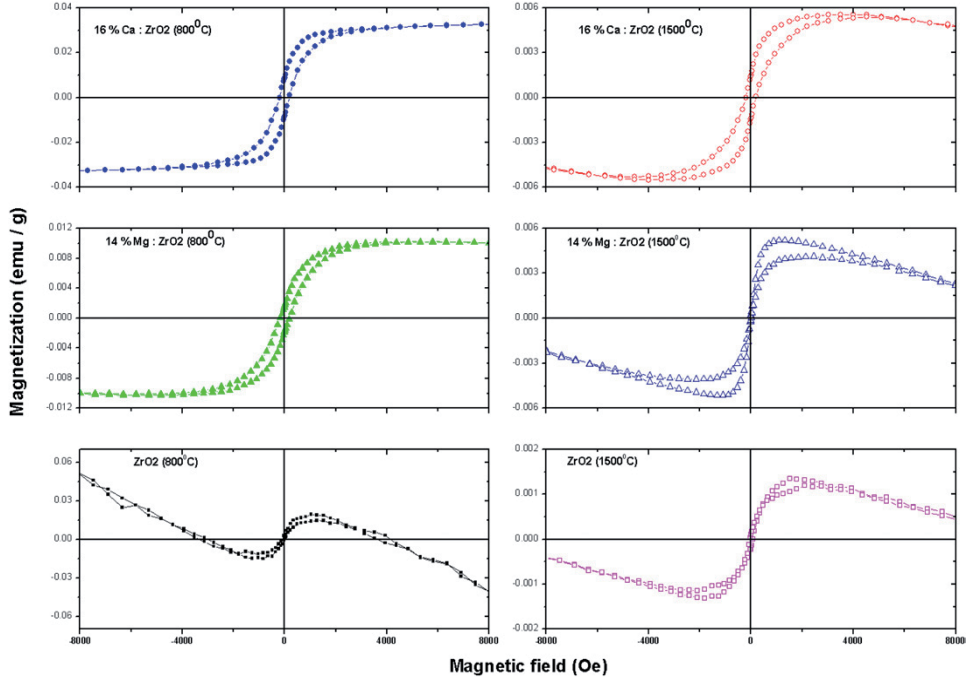


Figure 4.2.6. As-measured ( $T = 300$  K) hysteresis loops of Ca- and Mg-doped  $ZrO_2$  bulk samples heated at 800 and 1500 °C

Table 4.2.2. Magnetic parameters for different Ca and Mg doped zirconia samples

	$Zr_{0.84}Ca_{0.16}O_2$			$Zr_{0.86}Mg_{0.14}O_2$	
	800°C	1200°C	1500°C	800°C	1200°C
$M_s$ in emu/g (at 0.5T)	0.0335	0.0076	0.0055	0.012	0.005
Coercivity (Oe)	200	200	200	185	25

Figure 4.2.7 shows the  $M - H$  curves measured at room temperature (300 K) for the  $Zr_{0.84}Ca_{0.16}O_2$  bulk samples annealed at 800, 1200 and 1500 °C/3 h in air. The magnetization decreases with increase in the sintering temperature, whereas the coercivity does not change noticeably. Saturation magnetization is six times larger for the sample annealed at 800 °C, as compared with the sample treated at 1500 °C. These results suggest that vacancies present at lower temperatures enhance the ferromagnetism, which diminishes on high-temperature treatments.

The decrease in oxygen vacancies on high-temperature treatments results in the lowering of the ferromagnetic order and magnetic moment. There are more vacancies at 800 °C, due to the mixed phase (tetragonal phase as an additional phase), also reported in another study (Lu *et al.*, 1997).

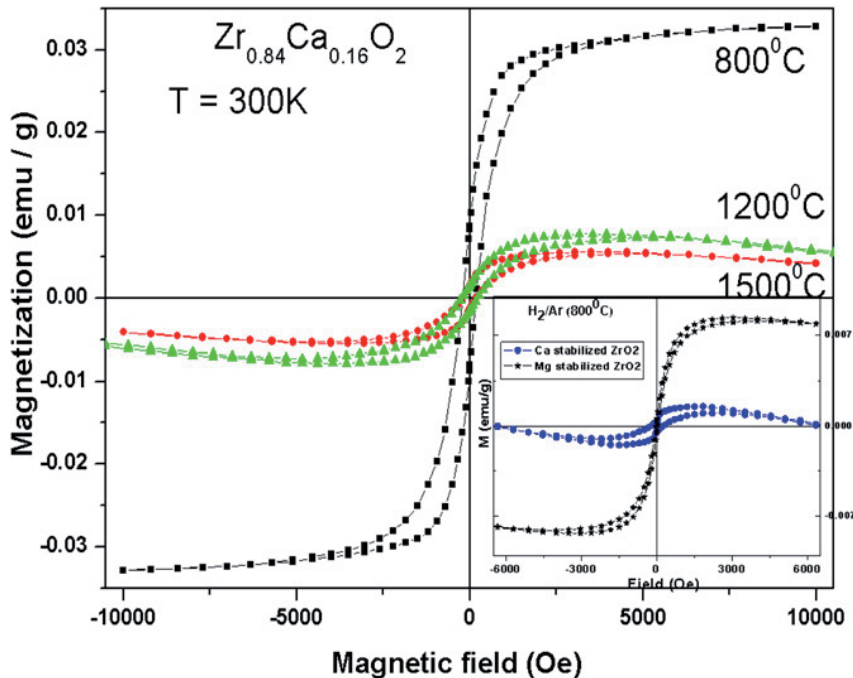


Figure 4.2.7. Hysteresis loops (measured at room temperature) of the  $Zr_{0.84}Ca_{0.16}O_2$  bulk samples sintered at different temperatures in air

The decrease in oxygen vacancies on high-temperature treatments are also observed in other studies conducted for photoluminescence (Xie *et al.*, 2010; Cong *et al.*, 2009). The inset shows the M – H loops of the Ca- and Mg - doped  $ZrO_2$  samples annealed in a  $H_2/argon$  environment. In order to examine the defect nature of magnetism, annealing in different environments was performed, but even annealing in  $H_2/Ar$  environment could not enhance the long-range ferromagnetic ordering at high temperatures, as expected due to the increasing number of oxygen vacancies. The temperature dependence of magnetization for these samples was also measured in the temperature range 10 – 350 K (figures not included), it was almost constant and did not show any transition in this temperature range.

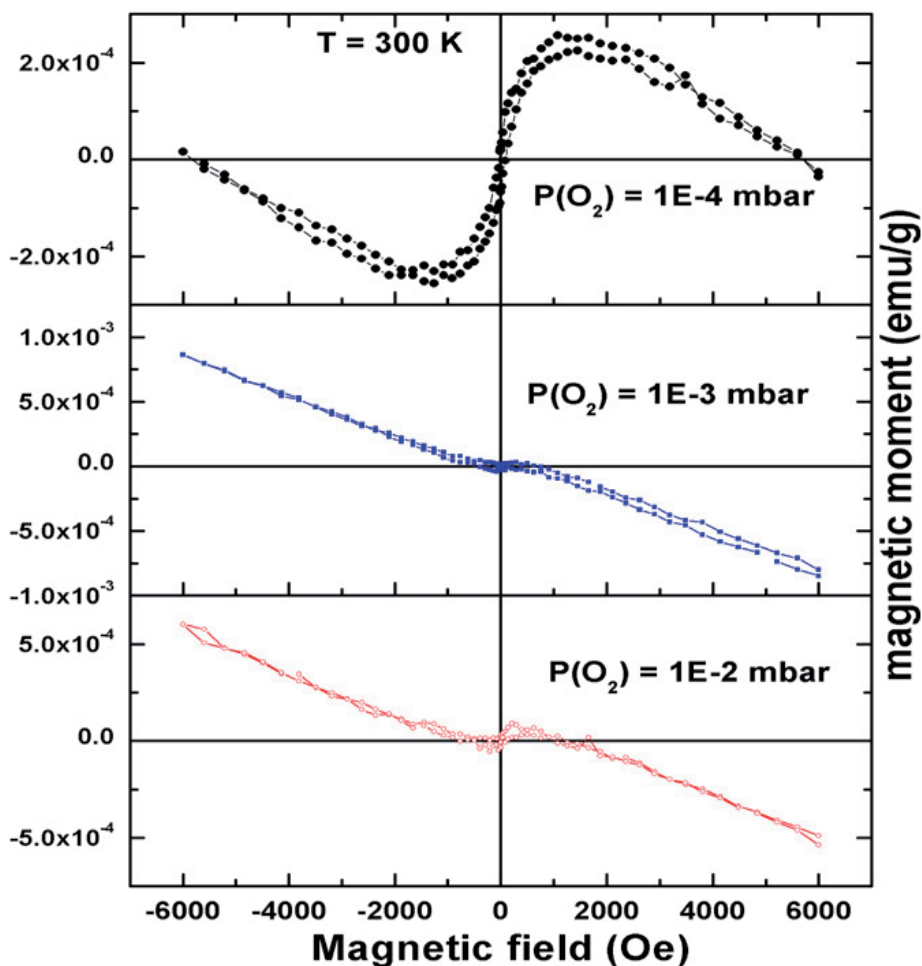


Figure 4.2.8. M–H loops measured (room temperature) for the thin films of  $Zr_{0.84}Ca_{0.16}O_2$  samples grown at different oxygen pressures

Figure 4.2.8 shows the dependence of magnetization on the magnetic field at room temperature for  $Zr_{0.84}Ca_{0.16}O_2$  thin films, grown on silicon substrates with different oxygen pressures. The ferromagnetic ordering is quite weak for samples grown at oxygen partial pressures of  $10^{-2}$  and  $10^{-3}$  mbar, whereas the film grown at an oxygen partial pressure of  $10^{-4}$  mbar shows ferromagnetic character. This indicates that the film grown at lower oxygen partial pressures has more oxygen vacancies, available for ferromagnetic ordering. This type of oxygen partial pressure dependence was also observed in doped ZnO and SnO<sub>2</sub> oxide thin films by Hong *et al.*, and in CeO<sub>2</sub> by Singhal *et al.* (Hong *et al.*, 2005; Singhal *et al.*, 2011). There are often significant differences between the properties of bulk samples and thin films due to the effects of the substrate, the magnetic moments are quite low in the thin film samples, as expected. The magnetization does not saturate due to the dominating diamagnetic signal from

the silicon substrate, but the value of spontaneous magnetization ( $M$ )  $\sim 2 \times 10^{-4}$  emu  $\text{g}^{-1}$  (at 2000 Oe) and the coercivity is around 80 Oe, and those values are quite low as compared with bulk values (see table 4.2.2).

Usually, bulk  $\text{ZrO}_2$  is diamagnetic at room temperature. When  $\text{Ca}^{2+}$  or  $\text{Mg}^{2+}$  ions are substituted for zirconium ion ( $\text{Zr}^{4+}$ ) sites, compensating anionic vacancies are created in the  $\text{O}^{2-}$  sublattice. These anionic vacancies could be the origin of ferromagnetism in non-magnetic divalent ion doped  $\text{ZrO}_2$ . This type of defect induced magnetism has already been observed in thin films of undoped  $\text{HfO}_2$ ,  $\text{TiO}_2$  (Venkatesan *et al.*, 2004; Kim *et al.*, 2009) and many other nanoparticles (Sundaresan *et al.*, 2009; Coey *et al.*, 2008), usually found in thin films and nanoparticles due to surface effects. However, this type of ferromagnetism in our bulk samples is robust and repeatable (even after months), because the samples are highly crystalline cubic zirconia, obtained on heating at very high temperatures. High-temperature treatments and larger grains ruled out the possibilities of hygroscopic nature and ageing, which have been observed in our recent study on Mn-doped zirconia powders due to low-temperature treatments and nanosized grains (Dimri *et al.*, 2011).

#### 4.2.3.1. Magnetic properties of $\text{LaMnO}_3$ samples

To see the effects of the film thickness on magnetic properties, hysteresis curves and temperature dependence of magnetization were measured for the films. Figures 4.2.9 (a - c) show the hysteresis curves at 100 K for LM1300, LM1000, and LM900 thin films annealed at 800 °C in  $\text{N}_2$ . The saturation magnetization does not show any noticeable change with thickness, whereas the coercivity changes in some extent with thickness presumably due to lattice disorder and strain present in the films. The hysteresis loops at room temperature (300 K) were almost diamagnetic (figures not included). However, below the transition temperature the films show a strong ferromagnetic behaviour, which is clear from fig. 4.2.9.

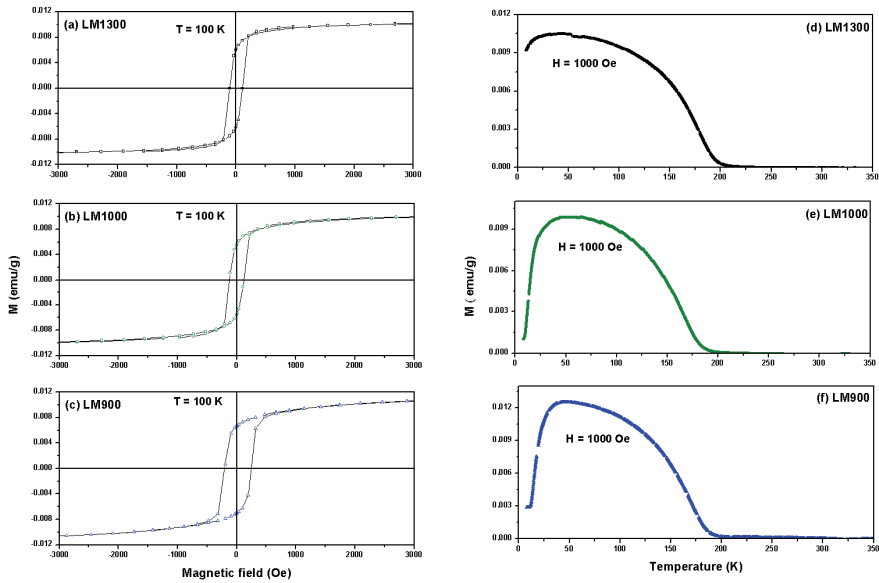


Figure 4.2.9. (a - c) Hysteresis ( $T = 100$  K) and (d - f) magnetization curves (ZFC at 0.1 T) for LM1300, LM1000 and LM900 thin films annealed at  $800$  °C in  $N_2$  atmosphere

The temperature dependence of magnetization (ZFC at 0.1 T or 1000 Oe) is shown in figs. 4.2.9 (d - f) for the films LM1300, LM1000 and LM900 annealed at  $800$  °C in  $N_2$ . LM1300 exhibits broad anomalies at 44 and 211 K (fig. 4.2.9 (d)), this is consistent with the results of another study (Romaguera-Barcelay *et al.*, 2011). These anomalies for LM1000 and LM900 were found to be around 46 and 196 K, and 45 and 200 K, respectively. The small shift in transition temperatures for different films of varying thicknesses might be the result of the presence of lattice disorder and/or strain in the films. The lower-temperature anomaly at around 45 K in the magnetization curves might be associated with re-arrangements of ferromagnetic domains, whereas the higher-temperature anomaly is likely associated with the paramagnetic-ferromagnetic phase transition ( $T_C$ ), usually occurring at 140 K in high-quality single crystals and ceramics (Ritter *et al.*, 1997). The noticeable increase in the Curie temperature in our thin films ( $T_C$  around 200 K) may be due to the non-stoichiometry (increased oxygen-to-cation ratio).

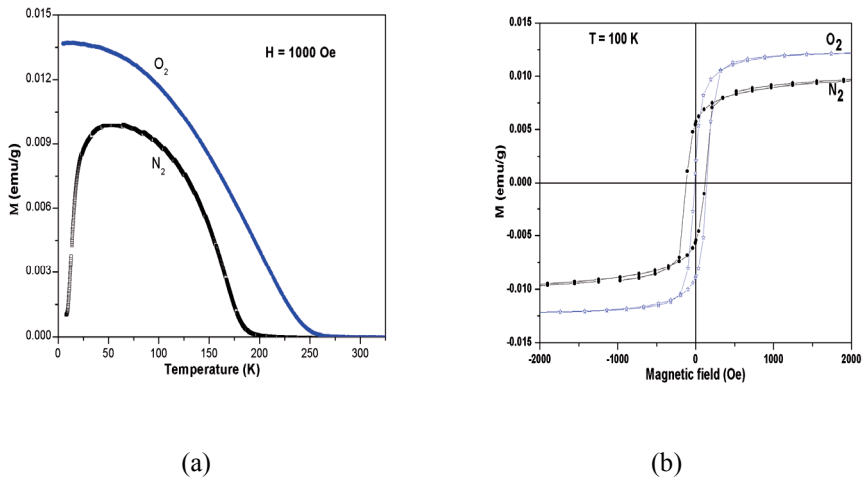


Figure 4.2.10. (a) Magnetization and (b) hysteresis ( $T = 100$  K) curves for LM1000 thin films annealed at  $800$  °C in  $N_2$  and  $O_2$  atmospheres

Figures 4.2.10 (a) and (b) show magnetization and hysteresis curves for LM1000 thin films annealed at  $800$  °C in  $N_2$  and  $O_2$  atmospheres. The film annealed in  $O_2$  atmosphere has  $T_C$  around  $250$  K, whereas the one annealed in  $N_2$  has a clearly lower  $T_C$  of around  $200$  K (figure 4.2.10 (a)). The high  $T_C$  value for our  $O_2$  - annealed LM1000 thin film is consistent with the enhanced  $T_C$  observed in another study on LMO thin films grown in pure oxygen atmosphere by pulsed laser deposition (Kim *et al.*, 2010). The larger saturation magnetization suggests the enhanced ferromagnetism for the  $O_2$ -annealed film as compared to that annealed in  $N_2$  atmosphere, however the coercivity is lower (fig. 4.2.10 (b)) for this film due to the larger grains (see AFM image in fig. 4.1.8). Our XRD and magnetic property characterization results are in good agreement with other studies on LMO thin films (Kim *et al.*, 2010; Raj Sankar *et al.*, 2005), and we hence conclude that upon  $O_2$  annealing the concentration of the smaller  $Mn^{4+}$  ions increases on the expense of the larger  $Mn^{3+}$  ions which enhances the exchange coupling between  $Mn^{3+}$  and  $Mn^{4+}$  ions, resulting in improved ferromagnetism and the higher  $T_C$  value (Coe *et al.*, 1999).

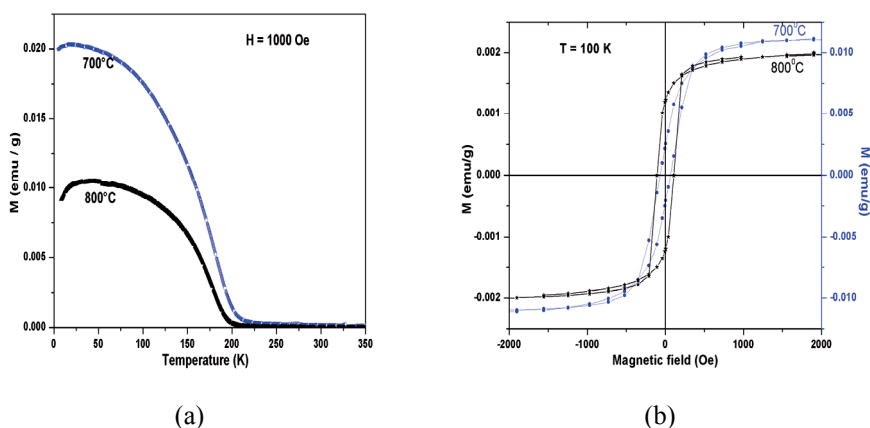


Figure 4.2.11. Magnetization and hysteresis curves ( $T = 100$  K) for LM1300 thin films annealed at 700 and 800 °C in  $N_2$

Annealing in  $O_2$  atmosphere induces cation vacancies in LMO, which results in an up-shift of the magnetic transition temperatures and enhanced ferromagnetic character arising from the canting of the antiferromagnetic arrangement of spins (Krishnamoorthy *et al.*, 2007; Raychaudhuri *et al.*, 2003). The magnetization curves of LM1300 thin films annealed in  $N_2$  atmosphere at 700 and 800 °C are shown in fig. 4.2.11 (a), revealing a decrease in  $T_C$  from 210 to 195 K with an increase in the annealing temperature from 700 to 800 °C, apparently due to an increase in the cation-to-oxygen ratio and a reduction in ferromagnetism. A decrease in the  $Mn^{4+}$  content at higher temperature may also be the reason for the depression of ferromagnetism and thus the lowering of  $T_C$ . Figure 4.2.11 (b) shows the hysteresis curve of LM1300 thin films (annealed at 700 and 800 °C in  $N_2$ ) measured at 100 K. There is an increase in the coercivity for the sample annealed at 800 °C, which can be related to the enhanced antiferromagnetism (at the measurement temperature of 100 K) for this film.

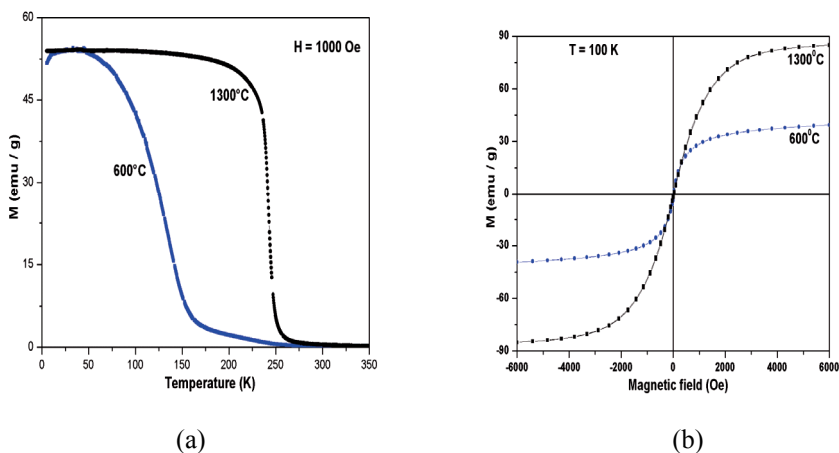


Figure 4.2.12. Magnetization and hysteresis curves ( $T = 100$  K) of LMO bulk samples annealed at 600 and 1300 °C in air

Figure 4.2.12 (a) shows the temperature dependence of magnetization of bulk LMO samples sintered at 600 and 1300 °C in air. Here  $T_C$  is increased (from 220 to 250 K) with increasing annealing temperature from 600 to 1300 °C in air indicating that the higher-temperature annealing in air results in an increased oxygen content (or higher  $Mn^{4+}$ - ion content) and formation of cation vacancies, which enhances the  $T_C$  (Ritter *et al.*, 1997; Joy *et al.*, 2002). Hysteresis loops measured at 100 K for the two bulk samples are shown in fig. 4.2.12 (b) revealing remarkably high values of saturation magnetization. Sankar and Joy (Sankar *et al.*, 2005) obtained similar values of magnetization in self-doped LMO prepared by solid state reaction method, through which the samples trap more La vacancies. Since Mn is smaller than La, Mn species can be incorporated on vacant La sites and consequently the valence state of Mn changes ( $Mn^{3+} \rightarrow Mn^{4+}$ ), the total concentration of  $Mn^{4+}$  ions increases and  $Mn^{3+} - O - Mn^{4+}$  interactions are enhanced (Brankovic *et al.*, 2010) resulting in better ferromagnetic properties. It is clear from fig. 4.2.12 (b) that the LMO bulk sample sintered at the lower temperature (600 °C) exhibits lower saturation magnetization and coercivity compared to the sample sintered at the higher temperature (1300 °C). We suggest that in the present case too sintering at 1300 °C in air induces La vacancies which then results in higher  $Mn^{4+}$  - ion concentration and enhanced ferromagnetic properties.

It is important to emphasize that the annealing atmosphere affects the magnetic properties significantly. Annealing in  $N_2$  atmosphere at higher temperature leads to the more stoichiometric samples and causes reduction in ferromagnetism, whereas the high-temperature treatment in air/ $O_2$  atmosphere leads to the non-stoichiometry and enhancement in ferromagnetism in  $LaMnO_3$  bulk and thin film samples. The structural and microstructural properties of

LMO thin films deposited by ALD method are found to be good and can be improved by changing substrates and deposition temperatures.

#### 4.2.3.2. MFM Studies of $\text{LaMnO}_3$ thin films

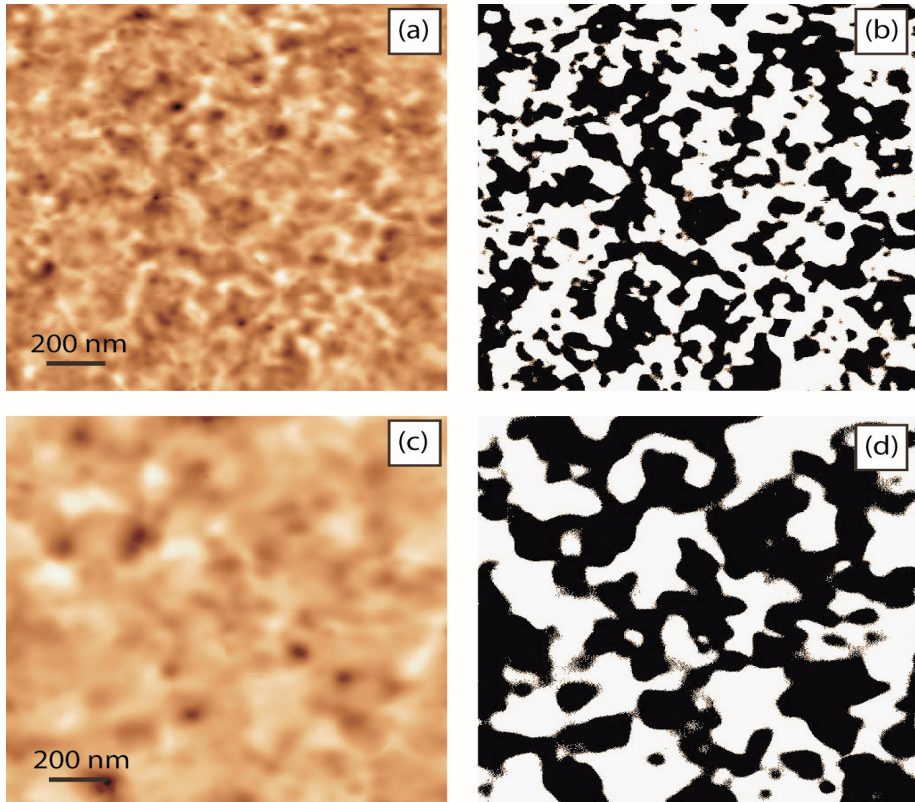


Figure 4.2.13. MFM images taken at constant average height ( $T = 65 \text{ K}$ ,  $H = 0$ ) of LM1000 film annealed at  $800^\circ\text{C}$ . Image (a)  $\text{N}_2$  atmosphere, (b) domain pattern derived from image (a); domain size  $50 - 100 \text{ nm}$ . Image (c)  $\text{O}_2$  atmosphere, (d) domain pattern derived from image (c); domain size  $150 - 200 \text{ nm}$

Magnetic force microscopy images were taken at  $65 \text{ K}$  and zero magnetic fields for the LM1000 films annealed in  $\text{N}_2$  and  $\text{O}_2$  atmospheres. The images were taken at constant average height in dynamic mode. The contrast observed in the images of fig. 4.2.13 corresponds to the detected shift of the centre frequency due to the interaction of the tip magnetic field with the stray field of the surface. Both images were taken at the same height and with the same cantilever amplitude, enabling a comparison to be made between the two films. Figure 4.2.13 shows the magnetic domain structure at  $65 \text{ K}$  to have domain size of  $50 - 100 \text{ nm}$  for the film annealed in  $\text{N}_2$  and  $150 - 200 \text{ nm}$  for the film annealed in  $\text{O}_2$ . These domain sizes correspond well to the grain sizes of the films as

measured by AFM (fig. 4.1.8 (c and d)), suggesting that the magnetic domains are pinned due to the topology of the surface.

### 4.3. Dielectric Studies of Y-type $\text{Ba}_{2-x}\text{Sr}_x\text{Mg}_2\text{Fe}_{12}\text{O}_{22}$ samples

Figure 4.3 shows the temperature and frequency dependence of the dielectric permittivity  $\epsilon_r$  and loss ( $\tan\delta$ ) of  $\text{Ba}_{2-x}\text{Sr}_x\text{Mg}_2\text{Fe}_{12}\text{O}_{22}$ . High dielectric loss is consistent with previous dielectric characterization on Y-type hexaferrites (Abo El Atta *et al.*, 2003). The dielectric permittivity exhibits very broad peaks in the range 430 – 680 K (figs. 4.3 (a) – (d)).

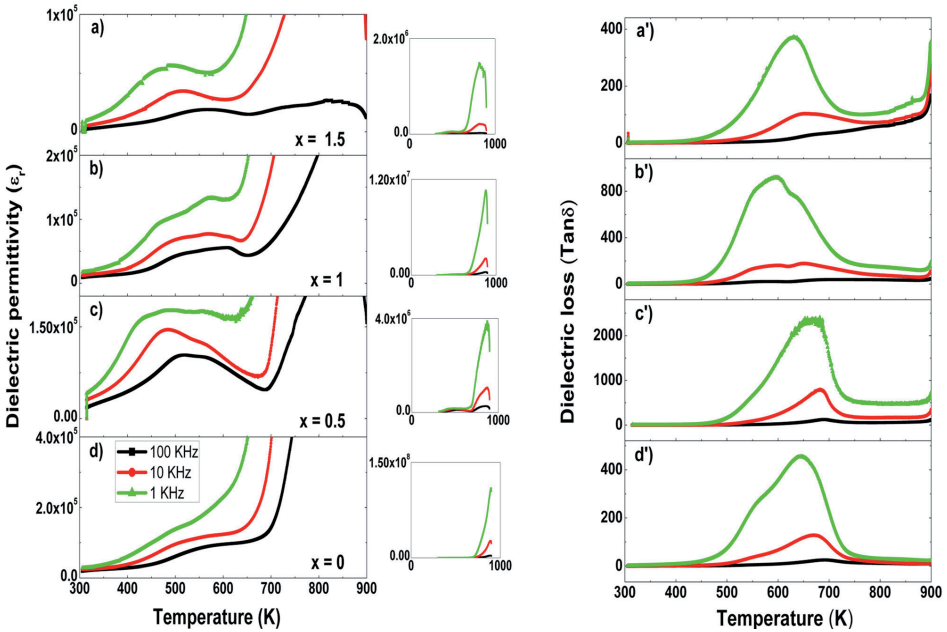


Figure 4.3. Temperature dependence of the dielectric permittivity  $\epsilon_r$  and dielectric loss ( $\tan\delta$ ) of  $\text{Ba}_{2-x}\text{Sr}_x\text{Mg}_2\text{Fe}_{12}\text{O}_{22}$  samples measured at different frequencies

The broadness and position of the peaks changed with strontium content, but no clear trend could be assigned. It is likely that these peaks are associated with the Curie (ferrimagnetic-paramagnetic) transition in the range 550 – 670 K as previously identified from our magnetic susceptibility data (see table 4.2.1). In addition, these peaks showed pronounced frequency dispersion, with the maximum shifting to higher temperature with increasing frequency. Frequency dependent peaks in the dielectric permittivity around the magnetic transition temperatures were also observed in other magnetic systems, such as bilayer manganite ( $\text{Pr}(\text{Sr}_{0.1}\text{Ca}_{0.9})_2\text{Mn}_2\text{O}_7$ ) (Ghosh *et al.*, 2009) and hexagonal  $\text{ABX}_3$ -type antiferromagnets (Morishita *et al.*, 2001). In the bilayer manganite, it was observed that the broad anomaly around the Curie temperature had an intrinsic

capacitive nature, which was also responsible for the frequency dispersion in the dielectric permittivity (Ghosh *et al.*, 2009). For the hexagonal ABX<sub>3</sub>-type antiferromagnets, the dielectric anomalies and the strong frequency dispersion observed in CsCoBr<sub>3</sub> and the weaker dispersion in RbCoBr<sub>3</sub> were attributed to spinlattice interaction (Morishita *et al.*, 2001). Our results suggest that in Y-type hexaferrite too, the perturbation of the magnetic order during heating produces frequency dependent broad peaks in the dielectric constant. This indicates that the dielectric properties are influenced by the magnetic state. The dielectric loss peaks shown in figs. 4.3 (a') – (d'), also attributed to the transformation of the magnetic order.

An additional anomaly in the dielectric permittivity was observed at higher temperatures in the range 820 – 890 K, represented by broad or narrower peaks (see out-set of figs. 4.3 (a) – (d)). The broadness and position of the peaks did not show any clear trend with strontium content. The position of the permittivity peaks at high temperatures (above 820 K) did not change with varying the frequency. This normally occurs in correspondence of structural modifications, suggesting that the dielectric constant peaks observed probably indicate a phase transition.

## 5. CONCLUSIONS

- Different samples of  $\text{Ba}_{2-x}\text{Sr}_x\text{Mg}_2\text{Fe}_{12}\text{O}_{22}$ , Ca and Mg stabilized zirconia ( $\text{ZrO}_2$ ), and  $\text{LaMnO}_3$  (LMO) were synthesized in bulk form by citrate combustion route, whereas thin films of Ca doped  $\text{ZrO}_2$  have been prepared by pulsed laser deposition (PLD) and LMO by atomic layer deposition (ALD) techniques.
- Strontium substitution for Barium in  $\text{Ba}_{2-x}\text{Sr}_x\text{Mg}_2\text{Fe}_{12}\text{O}_{22}$  alters the magnetic phase transition temperatures and magnetic hysteresis behaviour. Intermediate spin phase transition temperatures and the Curie temperature (ferrimagnetic-paramagnetic phase transition) shifted to higher temperatures with increasing strontium content. Saturation magnetization decreases and coercivity increases with increasing Sr substitution for Ba ions.  $^{57}\text{Fe}$  NMR spectrum measured at 5 K and in zero magnetic field was found to be broad for the  $\text{Ba}_2\text{Mg}_2\text{Fe}_{12}\text{O}_{22}$  hexaferrite due to a more complex structure when compared to the well resolved NMR spectra for M-type hexaferrites (Paper I).
- Broad and frequency dependent peaks for  $\text{Ba}_{2-x}\text{Sr}_x\text{Mg}_2\text{Fe}_{12}\text{O}_{22}$  samples were observed in the dielectric permittivity around the Curie temperature, evidencing that a change in the magnetic order affects the dielectric properties (Paper I).
- Room-temperature ferromagnetism have observed in Ca and Mg stabilized zirconia ( $\text{ZrO}_2$ ) bulk samples and similar thin film oriented in [1 1 1] direction. X-ray diffraction studies and Raman spectra measured at room temperature reveal the formation of cubic phase zirconia. Bulk powders show good ferromagnetic hysteresis loops, whereas it is weaker in thin films. The origin of the ferromagnetism can be related to oxygen vacancies created due to divalent calcium and magnesium ion substitution for tetravalent zirconium ions (Paper II).
- High-quality perovskite-structured LMO thin films deposited on silicon substrates by the atomic layer deposition technique and also bulk LMO samples synthesized by a citrate combustion method. All thin films annealed at 700-800 °C and bulk samples (sintered at 600 and 1300 °C) exhibited the single-phase perovskite-type lanthanum manganite structure, as confirmed from both XRD and Raman spectroscopy data. (Paper III).
- Variations in film thickness, annealing atmosphere ( $\text{N}_2$  or  $\text{O}_2$ ) and temperature did not affect the crystal structure but changed the microstructure, surface morphology, oxygen-to-cation ratio and

magnetic transition temperatures in our LMO thin films. The oxygen non-stoichiometry (i.e. cation vacancies) and thereby the  $\text{Mn}^{4+}/\text{Mn}^{3+}$  ratio tuned by the processing parameters caused the variation in magnetic properties of our ALD-grown LMO thin films as well as the bulk samples (Paper III).

- Annealing in  $\text{N}_2$  atmosphere enhanced the antiferromagnetism and better stoichiometry, whereas the air/ $\text{O}_2$  annealing enhanced the ferromagnetism and non-stoichiometry in LMO samples. The Curie transition temperatures in our LMO film and bulk samples were found to be higher from the ideal value ( $\sim 140$  K), which also could be related to non-stoichiometry (Paper III).

## REFERENCES

- Abo El Atta, A. M., Attia, S. M., 2003. *J. Magn. Magn. Mater.* 257, 165.
- Abrashev, M. V. et al., 1999. *Phys. Rev. B* 59, 4146.
- Adam, J., Rogers, M. D., 1959. The crystal structure of  $ZrO_2$  and  $HfO_2$ . *Acta Cryst.* 12, 951.
- Albanese, G., 1977. *J. Phys. Colloq.* 38, C1–85.
- Anane, A., 1998. PhD thesis, Université de Paris XI.
- Anderson, P. W., 1950. *Phys. Rev.* 79, 350.
- Anderson, P. W., 1950. *Phys. Rev.* 79, 705.
- Arulraj, A., Mahesh, R., Subbanna, G. N., Mahendiran, R., Raychaudhuri, A. K., Rao, R., 1996. *J. solid-st. Chem.* 127, 87.
- Aruta, C., Angeloni, M., Balestrino, G., et al., 2006. *J. Appl. Phys.* 100, 023910.
- Aulock, W. H. von (ed.), Boxer, A. S., Ollom, J. F., and Rauchmiller, R. F., 1965. *Handbook of Microwave Ferrite Materials*, Academic Press, London.
- Bai, Y., Zhou, J., Gui, Z., Yue, Z., Li, L., 2003. *J. Magn. Magn. Mater.* 264, 44.
- Bai, Y., Zhou, J., Gui, Z., Li, L., 2004. *Mater. Lett.* 58, 1602.
- Bai, Y., Zhou, J., Gui, Z., Li, L., 2005. *J. Am. Ceram. Soc.* 88, 318.
- Bai, Y., Zhou, J., Gui, Z., Li, L., 2006. *Mater. Chem. Phys.* 98, 66.
- Baker, H. (Ed.), 1992. *Alloy Phase Diagrams*. ASM International, Ohio, USA.
- Belov, K. P., Koroleva, L. I., Levitin, R. Z., Jergin, Y. V., Pedko, A. V., 1965. *Phys. Staus Solidi* 12, 219.
- Bouzerar, G., Ziman, T., 2006. *Phys. Rev. Lett.* 96, 207602.
- Brankovic, Z., Duris, K., Radojkovic, A., Bernik, S., Jaglicic, Z., Jagodic, M., Vojisavljevic, K., Brankovic, G., 2010. *J Sol-Gel Sci Technol* 55, 311.
- Braun, P. B., 1952. *Nature* 170, 708, doi:10.1038/170708a0.
- Braun, P. B., 1957. *Philips Res. Rep.* 12, 491.
- Bryan, J. D., Heald, S. M., Chambers, S. A., Gamelin, D. R., 2004. *J. Am. Chem. Soc.* 126, 11640.
- Buschow, K. H. J., and Boer, F. R. de, 2004. *Physics of Magnetism and Magnetic Materials*. Kluwer Academic Publishers, New York, Boston, Dordrecht, London, Moscow.
- Butler, E. P., 1985. Transformation-toughened zirconia ceramics. *Mater. Sci. Tech.* 1, 417-431.
- Carter, C. B., Norton, M. G., 2007. *Ceramic materials: science and engineering*. Springer, ISBN 0-387-46270-8.
- Castelliz, L. M., Kim, K. M., Boucher, P. S., 1969. *J. Can. Ceram. Soc.* 38, 57.
- Chai, Y. S., Chun, S. H., Haam, S. Y., Oh, Y. S., Kim, I., Kim, K. H., 2009. *N. J. Phys.* 11, 073030.
- Chatterji, T., Henry, P. F., and Ouladdiaf, B., 2008. *Phys. Rev. B* 77, 212403.
- Cheetham, A. K., Rao, C. N. R., Vogt, T., 1996. *J. solid-st. Chem.* 126, 337.
- Chen, M. S., Shen, Z. X., Liu, X. Y., Wang, J., 2000. *J. Mater. Res.* 15, 483.
- Cho, H.-S., Kim, S.-S., 1999. *IEEE Trans. Magn.* 35, 3151.
- Choi, W. S., 2009. *Trans. Electr. Electron. Mater.* 10, 200.
- Choi, W. S., Marton, Z., Jang, S. Y., Moon, S. J., Jeon, B. C., Shin, J. H., Seo, S. S. A., Noh, T. W., Kim, M.-W., Lee, H. N. and Lee, Y. S., 2009. *J. Phys. D: Appl. Phys.* 42, 165401.
- Chun, S. H., Chai, Y. S., Oh, Y. S., Jaiswal-Nagar, D., Haam, S. Y., Kim, I., Lee, B., Nam, D. H., Ko, K.-T., Park, J.-H., Park, J.-H., Chung, J.-H., and Kim, K. H., 2010.

- Phys. Rev. Lett. 104, 037204.
- Clavel, G., Willinger, M. G., Zioun, D. Pinna, N. 2008. Eur. J. Inorg. Chem. 6, 863–868.
- Coey, J. M. D., Venkatesan, M., Stamenov, P., Fitzgerald, C. B., Dorneles, L. S., 2005. Phys. Rev. B 72, 024450.
- Coey, J. M. D., Viret, M., von Molnar, S., 1999. Mixed-valency manganites, *Advances in Physics* 48, 167-293.
- Coey, J. M. D., Wongsaprom, K., Alaria, J., Venkatesan, M., 2008. J. Phys. D: Appl. Phys. 41, 134012.
- Cong, Y., Li, B., Yue, S. M., Fan, D., Wang, X. J., 2009. J. Phys. Chem. C 113, 13974.
- Cullity, B. D., and Graham, C. D., 2009. *Introduction to Magnetic Materials*, Second Edition. Institute of Electrical and Electronics Engineers, Inc.
- De, K., Ray, R., Panda, R.N., Giri, S., Nakamura, H., Kohara, T., 2005. J. Magn. Magn. Mater. 288, 339.
- De Silva, P. S. I. P. N., Richards, F. M., Cohen, L. F., Alonso, J. A., Martinez-Lope, M. J., Casais, M. T., Thomas, K. A., MacManus-Driscoll, J. L., 1998. J. Appl. Phys. 83, 394.
- Dietl, T., Ohno, H., Matsukura, F., Cibert, J., Ferrand, D., 2000. Science 287, 1019.
- Dimri, M. C., Kashyap, S. C., Dube, D. C., 2004. Ceram. Int. 30, 1623.
- Dimri, M. C., Stern, R., Kashyap, S. C., Bhatti, K. P., Dube, D. C., 2009. Phys. Status Solidi A 206, 270.
- Dimri, M. C., Khanduri, H., Kooskora, H., Joon, E., Heinmaa, I., Stern, R., 2011. J. Magn. Magn. Mater. 323, 2210.
- Dimri, M. C., Kooskora, H., Pahapill, J., Joon, E., Heinmaa, I., Subbi, J., Stern, R. 2011. Phys. Status Solidi a 208, 172.
- Dutta, P., Seehra, M., Zhang, Y., Wender, I., 2008. J. Appl. Phys. 103, 07D104.
- Dzyaloshinsky, I., 1958. J. Phys. Chem. Solids 4, 241-55.
- Eisenbraut, K. J., Sievers, R. E., 1956. J. Am. Chem. Soc. 87, 5254.
- Elemans, J. B. A. A., van Laar, K. R., van der Veen, K. R., and Loopstra, B. O., 1971. J. solid-st. Chem. 3, 238.
- Fang, X., Yang, B. Fen, A., Li-Jie, Q., 2008. Chin. Phys. B 17, 4652.
- Fischer, R. F., Kronmuller, H. J., 1998. Appl. Phys. 83, 3271.
- Garvie, R. C., 1988. A personal history of the development of transformation toughened PSZ ceramics. *Materials Science Forum* 34-36, 65-77.
- Gazzoli, D., Mattei, G., Valigi, M., 2007. J. Raman Spectrosc. 38, 824.
- Ghasemi, A., Hossienpour, A., Morisako, A., Saatchi, A., Salehi, M., 2006. J. Magn. Magn. Mater. 302, 429.
- Ghivelder, L., Abrego-Castillo, I., Gusmao, M. A., Alonso, J. A., and Cohen, L. F., 1999. Phys. Rev. B 60, 12184.
- Ghosh, B., Bhattacharya, D., Raychaudhuri, A. K., Arumugam, S., 2009. J. Appl. Phys. 105, 123914.
- Goldman, A., 2006. *Modern Ferrite Technology*, 2<sup>nd</sup> edn. Springer, Berlin.
- Goldschmidt, V.M., 1927-1928. *Geochemische verteilungsgesetzte der elemente*, VII, VIII.
- Goodenough, J. B., 1955. Phys. Rev. 100, 564.
- Goodenough, J. B., Loeb, A. L., 1955. Theory of ionic ordering, crystal distortion, and magnetic exchange due to covalent forces in spinals., *Phys. Rev.*, Vol. 98, 2, 391-408.
- Goodenough, J. B., 1958. J. Phys. Chem. Solids 6, 287.
- Gorter, E. W., 1957. Proc. Inst. Electr. Eng. 104B, 255–60.

- Guimarães, A. P., 1998. *Magnetism and Magnetic Resonance in Solids*. John Wiley & Sons, Inc.
- Gupta, A., McGuire, T. R., Duncombe, P. R., Rupp, M., Sun, J. Z., Gallagher, W. J., Xiao, G., 1995. *Appl. Phys. Lett.* 67, 3494.
- Hagaza, A., Kallel, N., Kallel, S., Guizouarn, T., Pena, O., and Oumezzine, M., 2009. *Journal of Alloy and Compounds* 486, 250-256.
- Hammond, G. S., Nonhebel, D. C., Wu, C. H. S., 1963. *Inorg. Chem.* 2, 73.
- Hann, R.E., Suitch, P. R., Pentecost, J. L., 1985. Monoclinic crystal structures of ZrO<sub>2</sub> and HfO<sub>2</sub> refined from X-ray powder diffraction data. *Commun. Am. Ceram. Soc.* C285-C286.
- Heck, C., 1974. In: *Magnetic materials and their applications*. London: Butterworth.
- Helmholtz, R. V., Wecker, J., Holzapfel, B., Schultz, L., Samwer, K., 1993. Giant negative magnetoresistance in perovskite like LaBaMnO ferromagnetic films. *Phys. Rev. Lett.* 71, 2331-2333.
- Heuer, A. H., Chaim, R., Lanteri, V., 1988. Review: Phase transformations and microstructural characterisation of alloys in the system Y<sub>2</sub>O<sub>3</sub>-ZrO<sub>2</sub>. *Advances in Ceramics* 24, 3-20.
- Hill, R. J., Cranswick, L. M. D., 1994. International Union of Crystallography Commission on Powder Diffraction Rietveld round robin. II. Analysis of monoclinic ZrO<sub>2</sub>. *J. Appl. Cryst.* 27, 802-844.
- Hong, N. H., Park, C. K., Raghavender, A. T., Ciftja, O., Bingham, N. S., Phan, M. H., Srikanth, H., 2012. *J. Appl. Phys.* 111, 07C302.
- Hong, N. H., Sakai, J., Huong, N. T., Poirot, N., Ruyter, A., 2005. *Phys. Rev. B* 72, 045336.
- Howard, C. J., Hill, R. J., Reichart, B.E., 1988. *Acta Crystallographa* B44, 116.
- Howard, C. J., Hunter, B. A., Kim, D.-J., 1998. Oxygen position and bond lengths from lattice parameters in tetragonal zirconias. *J. Am. Ceram. Soc.* 81, 241-243.
- Hueur, A. H., Riihle, M., in *Advances in Ceramics*, edited by Claussen, N., Riihle, M., Hueur, A. H., 1984. *Am. Ceram. Soc., Columbus, OH* 12, 1-13.
- Hughan, R. R., Hannink, R. H., 1986. Precipitation during controlled cooling of magnesia partially stabilized zirconia. *J. Am. Ceram. Soc.* 69, 556-563.
- Hwang, H. Y., Palstra, T. T. M., Cheong, S.-W., Batlogg, B., 1995. Pressure effects on the magnetoresistance in doped Mn perovskite. *Phys. Rev. B* 52, 15046-15049.
- Iliev, M. N., Abrashev, M. V., 2001. *J. Raman Spectrosc.* 32, 805.
- Ishiwata, S., Taguchi, Y., Murakawa, H., Onose, Y., Tokura, Y., 2008. *Science* 319, 1643.
- Ishiwata, S., Taguchi, Y., Tokunaga, Y., Murakawa, H., Onose, Y., Tokura, Y., 2009. *Phys. Rev. B* 79, 180408 (R).
- Ishiwata, S., Okuyama, D., Kakurai, K., Nishi, M., Taguchi, Y., Tokura, Y., 2010. *Phys. Rev. B* 81, 174418.
- Jakubovics, J. P., 1994. *Magnetism and Magnetic Materials*, 2nd Ed., Institute of Materials, London.
- Jonker, G. H., Wijn, H. P. J., Braun, P. B., 1956. *Philos. Technol. Rev.* 18, 145.
- Joy, P. A., Sankar, R. C., Date, S. K., 2002. *J. Phys.: Condens. Matter* 14, 4985.
- Kamba, S., Goian, V., Savinov, M., Buixaderas, E., Nuzhnyy D., et al., 2010. *J. Appl. Phys.* 107, 104109.
- Kanamori, J., 1959. *J. Phys. Chem. Solids* 10, 87.
- Karapetrova, E., Platzer, R., Gardner, J. A., Schutfort, E., Sommers, J. A., Evenson, W. E., 2001. *J. Am. Ceram. Soc.* 84 65.
- Kartopu, G., Es-Souni, M., 2006. *J. Appl. Phys.* 99, 033501.

- Kida, N., Kumakura, S., Ishiwata, S., Taguchi, Y., Tokura, Y., 2011. *Phys. Rev. B* 83, 064422.
- Kida, N., Okuyama, D., Ishiwata, S., Taguchi, Y., Shimano, R., Iwasa, K., Arima, T., Tokura, Y., 2009. *Phys. Rev. B* 80, 220406 (R).
- Kim, D., Hong, J., Park, Y. R., Kim, K. J., 2009. *J. Phys.: Condens. Matter* 21, 195405.
- Kim, D.-J., 1997. Effect of tetravalent dopants on Raman spectra of tetragonal zirconia. *J. Am. Ceram. Soc.* 80 (6) 1453-1461.
- Kim, H. S., Christen, H. M., 2010. *J. Phys.: Condens. Matter* 22, 146007.
- Kim, T. O., Kim, S. J., Grohs, P., Bonnenberg, D., Hempel, K. A., 1992. In: *Ferrites*, proc ICF6, Tokyo and Kyoto, p. 75.
- Kimura, T., Lawes, G., Raimirez, A. P., 2005. *Phys. Rev. Lett.* 94, 137201.
- Kimura, T., 2012. *Annu. Rev. Condens. Matter Phys.* 3, 93.
- Kisi, E. H., Howard, C. J., 1998. Crystal structure of zirconia phase and their inter-relation. *Key Engineering Materials* 153-154, 1-36.
- Kitagawa, Y., Hiraoka, Y., Honda, T., Ishikura, T., Nakamura, H., Kimura, T., 2010. *Nature Mater.* 9, 797.
- Kleine, A., Luo, Y., Samwer, K., 2006. *Europhys. Lett.* 76, 135.
- Kramers, H. A., 1934. *Physica* 1, 182.
- Kreisel, J., Lucazeau, G., Vincent, H., 1998. *J. Solid State Chem.* 137, 127.
- Kreisel, J., Lucazeau, G., Vincent, H., 1999. *J. Raman Spectrosc.* 30, 115.
- Krishnamoorthy, C., Sethupathi, C. K., Sankaranarayanan, V., Nirmala, R., Malik, S. K., 2007. *J Alloys Compd* 438, 1.
- Kubo K., Ohata, N., 1972. A quantum theory of double exchange. *J. Phys. Soc. Jpn.* 33, 21-32.
- Kumar, S., Pramamik, P., 1995. Innovative chemical method preparation of calcia stabilized zirconia powders, *Trans. J. Br. Ceram. Soc.* 94, 123–126.
- Lalena, J. N., Cleary, D. A., 2010. *Principles of Inorganic Materials Design*, 2nd ed., John Wiley & Sons, New York, pp. 345-346.
- Lee, S. G., Kwon, S. J., 1996. *J. Magn. Magn. Mater.* 153, 279.
- Liu, Y. C., Tung, S. K., Hsieh, J. H., 2006. *J Cryst Growth* 287, 105.
- Lotgering, F. K., Enz, U., Smit, J., 1961. *Philips. Res. Rep.* 16, 441.
- Lu, X., Liang, K., Gu, S., Zheng, Y., Fang, H., 1997. *J. Mater. Sci.* 32, 6653-6656.
- Luo, J., Stevens, R., 1999. *J. Am. Ceram. Soc.* 82, 1922–1924.
- Lynch, C. T., Bahldiek, F. W., Robinson, L. B., 1961. *J. Am. Ceram. Soc.* 44, 147-148.
- Maca, F., Kudrnovsk'y, J., Drchal, V., and Bouzerar, G., 2008. *Appl. Phys. Lett.* 92, 212503.
- Mahendiran, R., Mahesh, R., Rangavittal, N., Tewari, S., Raychauduri, A., Ramakrishnan, T., Rao, C., 1996. *Phys. Rev. B* 53, 3348.
- Maiti, H. S., Gokhale, K. V. G. K., Subba Rao, E.C., 1972. *J. Am. Ceram. Soc.* 55, 317-322.
- Matsumoto, G., 1970. *J. phys. Soc. Japan* 29, 606.
- Matsumoto, Y., Murakami, M., Shono, T., Hasegawa, T., Fukumura, T., Kawasaki, M., Ahmet, P., Chikyow, T., Koshihara, S., Koinuma, H., 2001. *Science* 291, 854.
- Millis, A. J., 1998. *Nature* 392, 147.
- Millis, A. J., 1998. *Philos. Trans. R. Soc. Lond. Ser. A, Math.Phys. Sco.* 356, 1473-1478.
- Momozawa, N., 1986. *J. Phys. Soc. Jpn.* 55, 4007–13.
- Momozawa, N., Yamaguchi, Y., 1993. *J. Phys. Soc. Jpn.* 62, 1292–304.
- Momozawa, N., Yamaguchi, Y., Takei, H., Mita, M., 1985. *J. Phys. Soc. Jpn.* 54, 3895.
- Morell, G., Katiyar, R. S., Torres, D., Paje, S. E., Llopis, J., 1997. *J. Appl. Phys.* 81,

- 2830.
- Morishita, K., Iio, K., Mitsui, T., Kato, T., 2001. *J. Magn. Magn. Mater.* 226, 579.
- Moriya, T., 1960. *Phys. Rev.* 120, 91–98.
- Murray, P., Allison, E.B., 1954. *Trans. Brit. Ceram. Soc.* 53, 335-361.
- Murthy, V. R. K., Sundaram, S., Vishwanathan, B., 1993. *Microwave Materials*. Narosa Publishing House, New Delhi.
- Murugavel, P., Lee, J. H., Yoon, J.-G., and Noh, T. W., 2003. *Appl. Phys. Lett.* 82, 1908.
- Mustafa, E., 1997. Microstructure and mechanical properties of PSZ toughened alumina ceramics prepared via polymeric sol–gel route, PhD thesis from Faculty of Science, Cairo University.
- Nakayama, S., Okasaki, M., Aung., Y.L., Sakamoto, M., 2003. *Solid State Ionics* 158, 133.
- Neel, L., 1948. *Ann. Phys.* 3, 137.
- Ni, H., Yu, D., Zhao, K., Kong, Y. C., Wong, H. K., Zhao, S. Q., Zhang, W. S., 2011. *J. Appl. Phys.* 110, 033112.
- Nielsen, R., 2005. Zirconium and Zirconium Compounds, in *Ullmann's Encyclopedia of Industrial Chemistry*, Wiley-VCH, Weinheim.
- Nishizawa, H., Yamasaki, N., Matsuoka, K., Mitsushio, H., 1982. Crystal structure and transformation of zirconia under hydrothermal conditions. *J. Am. Ceram. Soc.* 65 (7) 343-346.
- Obol, M., Vittoria, C., 2003. *J. Magn. Magn. Mater.* 265, 290.
- Ogale, S. B., et al 2003. *Phys. Rev. Lett.* 91, 077205.
- Ohno, H., 1998. *Science* 281, 951.
- Orgaini, P., Aruta, C., Ciancio, R., Galdi, A., Maritato, L., 2009. *Appl. Phys. Lett.* 95, 013510.
- Ostanin, S., Ernst, A., Sandratskii, L. M., Bruno, P., Dane, M., Hughes, I. D., Staunton, J. B., Hergert, W., Mertig, I. Kudrnovsky, J., 2007. *Phys. Rev. Lett.* 98, 016101.
- Özgur, U., Alivov, Y., Morkoc, H., 2009. *J. Mater Sci: Mater Electron* 20, 789-834.
- Patil, R. N., Subba Rao, E. C., 1970. *Acta Crystallogr.* A26, 555.
- Perekalina, T. M., Shchvrova, A. D., Fonton, S. S., Annikov, D. G., 1970. *Soviet. Phys. JETP.* 31, 440.
- Philip, J., Theodoropoulou, N., Berera, G., Moodera, J. S., Satpati, B., 2004. *Appl. Phys. Lett.* 85, 777.
- Pollert, E., 1985. *Prog. Cryst. Growth and Charact.* 11, 155–205.
- Pore, V., 2010. Atomic Layer Deposition and Photocatalytic Properties of Titanium Dioxide Thin Films, PhD Thesis. ([www.doria.fi/bitstream/handle/10024/62220/atomicla.pdf](http://www.doria.fi/bitstream/handle/10024/62220/atomicla.pdf)).
- Pullar, R. C., 2012. Hexagonal ferrites: A review of the synthesis, properties and applications of hexaferrite ceramics. *Progress in Materials Science* 57, 1191–1334.
- Puri, R. K., Babbar, V. K., 1997. *Solid State Physics & Electronics*. S. Chand & Company LTD. Ram Nagar, New Delhi-110055.
- Putkonen, M., Niinistö, J., Kukli, K., Sajavaara, T., Karppinen, M., Yamauchi, H., Niinistö, L., 2003. *Chem. Vap. Deposition* 9, 207.
- Quezel-Ambrunaz, S., 1968. *Bull. Soc. Fr. Mineral. et de Crystallogr.* 91, 339.
- Ranno, L., Viret, M., Mari, A., Thomas, R. M., Coey, J. M. D., 1996. *J. Phys: condens. Matter* 8, L33.
- Raychaudhuri, P., Mitra, C., 2003. *J Appl Phys* 93, 8328.
- Richter, H. G., 1968, *IEEE Trans. Magn. Magn.* 4, 263.
- Ritala, M., Leskelä, M., Nalwa, H. S. (Ed.), 2001. *Handbook of Thin Film Materials*,

- Academic Press, San Diego, CA, USA, Vol. 1, Chapter 2, p. 103.
- Ritter, C., Ibarra, M.R., Teresa, J. M. De, Algarabel, P. A., Marquina, C., Blasco, J., García, J., Oseroff, S., Cheong, S.-W., 1997. *Phys Rev B* 56, 8902–8911.
- Romaguera-Barcelay, Y., Agostinho Moreira, J., Gonzalez-Aguilar, G., Almeida, A., Araujo, J. P., Perez de la Cruz, J., 2011. *J Electroceram* 26, 44.
- Ruff, O., Ebert, F. Z., 1929. *Anorg. U. All. Gem. Chem.* 180, 19–41.
- Sagayama, H., Taniguchi, K., Abe, N., Arima, T. H., Nishikawa, Y., Yano, S. I., Kousaka, Y., Akimitsu, J., Matsuura, M., Hirota, K., 2009. *Phys. Rev. B* 80, 180419(R).
- Salamon, M. B., Jaime, M., 2001. *Rev. Mod. Phys.* 73, 583.
- Sankar, R. C., Joy, P. A., 2005. *Phys. Rev. B* 72, 02440.
- Santen, J. H. V., Jonker, G. H., 1950. Electrical conductivity of ferromagnetic compounds of Mn with perovskite structure. *Physica*, 16, 599–600.
- Schwartz, M. M., 1992. *Handbook of Structural Ceramics*, McGraw-Hill Inc, New York.
- Serena, S., Sainz, M. A., Aza, S. D., Caballero, A., 2005. *J. Eur. Ceram. Soc.* 25, 681.
- Sergienko, I. A., Dagotto, E., 2006. *Phys. Rev. B* 73, 094434.
- Sengupta, J., Sahoo, R. K., Bardhan, K. K., Mukherjee, C. D., 2011. *Materials Letters* 65, 2572.
- Sharma, P., Gupta, A., Rao, K. V., Owens, F. J., Sharma, R., Ahuja, R., Osorio Guillen, J. M., Johansson, B., Gehring, G. A., 2003. *Nature Mater.* 2, 673.
- Shiffer, P., Ramirez, A. P., Bao, W., Cheong, S.-W., 1995. Low temperature magnetoresistance and the magnetic phase diagram of  $\text{La}_{1-x}\text{Ca}_x\text{MnO}_3$ . *Phys. Rev. Lett.* 75, 3336–3339.
- Shimizu, Y., Murata, T., 1997. *J. Am. Ceram. Soc.* 80, 2702.
- Simoes, A. Z., Riccardi, C. S., Dos Santos, M. L., Gonzalez Garcia, F., Longo, E., Varela, J. A., 2009. *Mater. Res. Bull.* 44, 1747.
- Singhal, R. K., Kumari, P., Kumar, S., Dolia, S. N., Xing, Y. T., Alzamora, M., Deshpande, U. P., Shripathi, T., Saitovitch, E., 2011. *J. Phys. D: Appl. Phys.* 44, 165002.
- Siwach, P. K., Singh, H. K., Srivastava, O. N., 2008. *J. Phy: Condens. Matter* 20, 273201.
- Sixtus, K. J., Kronenberg, K. J., Tenzer, R. K., 1956. *J. Appl. Phys.* 27, 1051.
- Skumryev, V., Ott, F., Coey, J. M. D., Anane, A., Renard, J.-P., Pinsard-Gaudart, L., and Revcolevsch, A., 1999. *Eur. Phys. J. B* 11, 401.
- Slowak, R., Voight, C., Hempel, K. A., Kypriamidis, A., 1977. *Appl. Phys.* 14, 197.
- Smith, D. K., Newkirk, H. W., 1965. *Act Cryst.* 18, 989–991.
- Smith, J., Wijn, H. P. J., 1959. *Ferrites*. Philips Technical Library, Eindhoven, The Netherlands, pp. 177–190, 285.
- Solovyev, I., Hamada, N., Terakura, K., 1996. *Phys. Rev. Lett.* 76, 4825.
- Srinivasan, R., Simpson, S. F., Harris, J. M., Davis, B. H., 1991. *J. Mater. Sci. Lett.* 10, 352–354.
- Streever, R. L., 1969. *Phys. Rev.* 186, 285.
- Stubican, V. S., Ray, S. P., 1977. *J. Am. Ceram. Soc.* 60, 534.
- Sudakar, C., Subbanna, G. N., Kutty, T. R. N., 2003. *J. Magn. Magn. Mater.* 263, 253.
- Sugimoto, S., Kondo, S., Okayama, K., Nakamura, H., Book, D., Kagotani, T., Homma, M., Ota, H., Kimura, M., Sato, R., 1999. *IEEE Trans. Magn.* 35, 3154.
- Sundaresan, A., Rao, C. N. R. 2009. *Nano Today* 4, 96.
- Suyama, R., Ashida, T., Kume, S., 1985. *J. Am. Ceram. Soc.* 68, C-134.
- Todorovska, R., Petrova, N., Todorovsky, D., Groudeva-Zotova, S., 2006. *Appl. Surf.*

- Sci. 252, 3441.
- Tokura, Y., Tomioka, Y., Kuwahara, H., Asamitsu, A., Moritomo, Y., Kasai, M., 1996. *J. Appl. Phys.* 79, 5288.
- Töpfer, J., Doumerc, J., Grenier, J.-C., 1996. *J. Mater. Chem.* 6, 1511.
- Töpfer, J., Goodenough, J. B., 1997. *J. Solid State Chem.* 130, 117.
- Tsang, C. F., Woo, J., 2000. *Materials Characterization* 45, 187.
- Utsumi, S., Yoshiba, D., Momozawa, N., 2007. *J. Phys. Soc. Jpn.* 76, 034704.
- Uusi-Esko, K., Karppinen, M., 2011. *Chem. Mater.* 23, 1835.
- Valenzuela, R., 1994. *Magnetic Ceramics*. Cambridge University Press, Cambridge.
- Varad Rajan Sakhalkar, 2009. *Structural, Magnetic and Surface Properties of RF-Magnetron Sputtered Undoped Lanthanum Manganite Thin Films*. MSc. Thesis, The University of Texas at Arlington.
- Venkatesan, M., Fitzgerald, C. B., Coey, J. M. D., 2004. *Nature* 430, 630.
- Venkatesan, M., Fitzgerald, C. B., Lunney, J. G., Coey, J. M. D., 2004. *Phys. Rev. Lett.* 93, 177206.
- Wang, C., Li, L., Zhou, J., Qi, X., Yue, Z., 2002. *J. Mater. Sci.: Mater. Electron.* 13, 713.
- Wang, L., Zhang, X., 2002. *Physica C*, 371, 330–338.
- Wang, X. L., Li, D., Shi, C. X., Li, B., Cui, T. Y., Zhang, Z. D., 2010. *Physica B* 405, 1362.
- Weihe, H., Güdel, H. U., 1997. *Inorg. Chem.* 36, 3632.
- Wen, Q. Y., Zhang, H. W., Song, Y. Q., Yang, Q.-H., Zhu, H., Xiao, J. Q., 2007. *J. Phys.: Condens. Matter.* 19, 246205.
- Went, J. J., Ratheneau, G. W., Gorter, E. W., Oosterhout, G. W. V., 1952. *Philips Tech. Rev.* 13, 194.
- Wijn, H. P. J., 1952. *Nature* 170, 707, doi:10.1038/170707a0.
- Withers, R. L., Thompson, J. G., Gabbitas, N., Wallenberg, L. R., Welberry, T. R., 1995. Microdomains, solid solutions and the “defect fluorite” to c-type sesquioxide transition in  $\text{CeO}_2\text{-RO}_{1.5}$  and  $\text{ZrO}_2\text{-RO}_{1.5}$  systems. *J. Solid State Chem.* 120, 290-298.
- Wollan, E. O., Koehler, W. C., 1955. *Phys. Rev.* 100, 545-563.
- Xie, Y., Ma, Z., Liu, L., Su, Y., Zhao, H., Liu, Y., Zhang, Z., Duan, H., Li, J., Xie, E., 2010. *Appl. Phys. Lett.* 97, 141916.
- Yashima, M., Kakihana, M., Ishii, K., Ikuma, Y., Yoshimura, M., 1996. Synthesis of metastable tetragonal (t') zirconia-calcia solid solution by pyrolysis of organic precursors and coprecipitation route. *J. Mater. Res.* 11, 1410-1420.
- Yin, S., Uchida, S. U., Fujishio, Y., Ohmori, M., Sato, T., 1999. Preparation of porous ceria doped tetragonal zirconia ceramics by capsule free hot isostatic pressing. *Trans. J. Br. Ceram. Soc.* 98, 19–23.
- Yoshimura, M., 1988. Phase stability of zirconia. *Bull. Am. Ceram. Soc.* 67, 1950-55.
- Youssef, S., Combette, P., Podlecki, J., Asmar, R. A., Foucaran, A., 2009. *Cryst. Growth Des.* 9, 1088.
- Yu, J., Duan, L. B., Yang, Y. C., Rao, G. H., 2008. *Physica B* 403, 4264.
- Zener, C., 1951. Interaction between the d-shells in the transition metals. II. ferromagnetic compounds of Mn with perovskite structure. *Phys. Rev.* 82, 403-405.
- Zhao, W. Y., Wei, P., Wang, W., Zhang, Q. J., 2008. *J. Appl. Phys.* 103, 063902.
- Zhizhin, G. N., Mavrin, B. N., Shabanov, V. F., 1984. *Optical Vibrational Spectra of Crystals* (Nauka, Moscow) 212.

## ACKNOWLEDGMENTS

The work presented in this thesis was carried out in the Laboratories of Chemical Physics of National Institute of Chemical Physics and Biophysics, Tallinn, Estonia, between September 2009 and March 2013.

This work was financially supported by the European Social Fund's 'Doctoral Studies and Internationalisation Programme' (DoRa) - DoRa4, DoRa6 and DoRa8, and partially supported by the Estonian Science Foundation grants 8440, 6852 and Estonian target funding project SF0690029s09.

First, I would like to thank my supervisor Dr. Raivo Stern for giving me opportunity for postgraduate studies, the constant encouragement and for the opportunities provided to me during the years of my PhD studies. I am grateful to Prof. Jüri Krustok for the support during my studies in TUT. I would also like to thank Prof. Maarit Karppinen for extending the experimental facilities and for her help during my stay at School of Chemical Technology, Aalto University, Espoo, Finland. I would like to thank Dr. Mukesh Chandra for all his guidance and support during structural and magnetic measurements and analysis. I am grateful to Dr. Ivo Heinmaa for help with the NMR measurements of Y-type hexaferrites and his valuable suggestions. I also owe thanks to the Mrs. Helgi Kooskora for her help in samples' preparation.

I am very grateful for the members of NICPB for their help and cooperation throughout the PhD period.

I would like to thank my parents for the love and support they have given me all through my life. I thank my brothers and in-laws for the encouragement. I would like to thank my son Arnav for bringing the happiness in my life. Finally I would like to thank my husband for his support, love and patience through it all.

## ABSTRACT

The structural and magnetic properties of various multifunctional oxides such as Y-type hexaferrites (chemical formula  $\text{Ba}_{2-x}\text{Sr}_x\text{Mg}_2\text{Fe}_{12}\text{O}_{22}$  with  $0 \leq x \leq 2$ ), Ca and Mg stabilized cubic zirconia ( $\text{ZrO}_2$ ) and  $\text{LaMnO}_3$  (LMO) samples have been studied in this thesis.

Due to much interest in the multiferroic Y-type hexaferrites, we investigated the effect of strontium substitution on structural, magnetic, and dielectric properties of  $\text{Ba}_{2-x}\text{Sr}_x\text{Mg}_2\text{Fe}_{12}\text{O}_{22}$  (with  $0 \leq x \leq 2$ ) samples. Y-type hexaferrite phase formation was not affected by strontium substitution for barium, in the range  $0 \leq x \leq 1.5$ , confirmed by x-ray diffraction and Raman spectroscopy measured at room temperature. Two intermediate magnetic spin phase transitions (at temperatures  $T_I$  and  $T_{II}$ ) and a ferrimagnetic-paramagnetic transition (at Curie temperature  $T_c$ ) were identified from the temperature dependence of the magnetic susceptibility. These magnetic transition temperatures increased with increasing strontium content. Magnetic hysteresis measurements indicated that by increasing strontium concentration, the coercivity increases, while the saturation magnetization decreases. The  $^{57}\text{Fe}$  NMR spectrum of the Y-type hexaferrite measured at 5 K and in zero magnetic field showed remarkable differences compared to that of other hexaferrites due to their different number of tetrahedral and octahedral iron sites. The temperature and frequency dependence of the dielectric permittivity evidenced broad peaks with frequency dispersion in correspondence of the Curie temperature.

We also studied the room-temperature ferromagnetism in Ca and Mg stabilized zirconia bulk samples and thin films for spintronic applications. Powders were prepared by the citrate-combustion route, and thin films grown on silicon substrates by the pulsed laser deposition technique. X-ray diffractograms and Raman spectra at room temperature reveal the formation of cubic phase zirconia. The observed ferromagnetism is robust at room temperature in both bulk as well as in thin film samples, although it is weaker in thin films. The origin of the ferromagnetism can be related to oxygen vacancies created due to divalent (calcium and magnesium) substitution for tetravalent zirconium ions.

Thin films of  $\text{LaMnO}_3$  (LMO) were deposited by the atomic layer deposition (ALD) technique on silicon (100) substrates, whereas bulk samples were prepared by citrate combustion route. Effects of varying thickness, annealing atmosphere and temperature were studied on both LMO sample classes. Single phase perovskite crystal structure was confirmed by X-ray diffraction and Raman spectroscopy, in thin films annealed at 700 and 800 °C as well as in bulk samples. Thin films annealed in  $\text{N}_2$  or  $\text{O}_2$  environments do not vary in the crystal structure, but differ by the oxygen stoichiometry, microstructure and magnetic properties. Curie temperature in all LMO thin films annealed in  $\text{N}_2$  was found to be around 200K, while it was around 250K for the films annealed in  $\text{O}_2$  as well as for the bulk samples.

## KOKKUVÕTE

Käesolevas doktoritöös on uuritud erinevate multifunktsionaalsete oksiidide, nagu Y-tüüpi heksaferriitide (keemilise valemiga  $Ba_{2-x}Sr_xMg_2Fe_{12}O_{22}$ ,  $0 \leq x \leq 2$ ), Ca- ja Mg-stabiliseeritud kuubilise tsirkooniumoksiidi ( $ZrO_2$ ) ja  $LaMnO_3$  (LMO) struktuursete ja magnetilisi omadusi.

Tänu suurele üldisele huvile multiferroiliste Y-tüüpi heksaferriitide vastu uurisime baariumi asukohale strontsiumi asendamise mõju  $Ba_{2-x}Sr_xMg_2Fe_{12}O_{22}$  (kus  $0 \leq x \leq 2$ ) proovide struktuursetele, magnetilistele ja dielektrilistele omadustele. Vahemikus  $0 \leq x \leq 1,5$  ei avaldanud strontsiumi asendamine baariumiga avastatavat mõju Y-tüüpi heksaferriidi faasi moodustumisele, mida kinnitasid toatemperatuuril mõõdetud röntgendifraktsioonianalüüs ja Ramani spektroskoopia. Magneetumise temperatuurisõltuvuse järgi identifitseeriti kaks vahepealset spinkorrastuse faasiüleminekut (temperatuuridel  $T_I$  ja  $T_{II}$ ) ja ferromagnetiline-paramagnetiline üleminek (Curie temperatuuril  $T_C$ ). Nende magnetiliste üleminekute temperatuurid tõusid koos kasvava strontsiumi sisaldusega. Magnetilise hüstereesi mõõtmised näitasid, et strontsiumi kontsentratsiooni suurenemisel koertsiivus kasvab, samal ajal kui magnetiline küllastus väheneb. 5 K juures nullväljas mõõdetud Y-tüüpi heksaferriidi  $^{57}Fe$  TMR spekter näitas tänu erinevale tetraeedriliste ja oktaeedriliste raua tsentrite olemasolule märkimisväärseid erinevusi teistest heksaferriitidest. Dielektrilise läbitavuse temperatuur- ja sagedussõltuvus avaldus Curie temperatuurile vastava sageduse dispersiooniga laiades piikides.

Me uurisime ka toatemperatuurset ferromagnetismi Ca ja Mg stabiliseeritud tsirkooniumoksiidi lähteproovides ning magnetoolektronilistes seadmetes kasutatavates õhukestes kiledes. Pulbrid valmistati tsitraat-põletamise meetodil ja õhukesed kiled kasvatati ränisubstraadil impulsslaser-sadestus meetodil. Toatemperatuurset röntgendifraktogrammid ja Ramani spektrid paljastavad kuubilise tsirkooniumoksiidi faasi tekkimise. Täheldatud ferromagnetism on toatemperatuuril stabiilne nii lähteaines kui ka õhukese kile proovides, olles õhukestes kiledes nõrgem. Ferromagnetismi päritolu võib seostada hapniku vakantsidega, mis tekkisid divalentsete ionide (kaltsium, magneesium) asendamisel tetravalentsete tsirkooniumi ionide asemele.

$LaMnO_3$  (LMO) õhukesed kiled sadestati räni (100) subtraatidele aatomkihtsadestamise (ALD) teel, mille lähteproovid valmistati tsitraat-põletamise meetodil. Muutuva paksuse, lõõmutamisatmosfääri ja -temperatuuri mõju uuriti mõlemat tüüpi LMO proovil. Ühefaasiline perovskiid kristallstruktuur kinnitati röntgendifraktsiooniga ja Ramani spektroskoopiaga nii 700 ja 800 °C juures lõõmutatud õhukestes kiledes kui ka lähteproovides. Õhukeste kilede  $N_2$  või  $O_2$  keskkondades lõõmutamine ei muuda kristallstruktuuri, kuid mõjutab hapniku stöhhiomeetriat, mikrostruktuuri ning magnetilisi omadusi.  $N_2$  keskkonnas lõõmutatud LMO õhukeste kilede Curie temperatuuriks määrati ligikaudu 200 K, samas oli  $O_2$  keskkonnas lõõmutatud õhukeste kilede ja lähteproovide Curie temperatuur ligikaudu 250 K.

# CURRICULUM VITAE

## 1. Personal data

Name Himani Khanduri  
Date and place of birth 12.07.1985, India

## 2. Contact information

Address Akadeemia tee 23, 12618, Tallinn, Estonia  
Phone +372 6398370  
E-mail himani.khanduri@gmail.com

## 3. Education

2009 – 2013 Tallinn University of Technology, PhD student of Physics  
2008 – 2009 H.N.B. Garhwal University, India, Bachelor of Education (B. Ed.)  
2004 – 2006 H.N.B. Garhwal University, India, Master of Science (M. Sc.)  
2001 – 2004 H.N.B. Garhwal University, India, Bachelor of Science (B. Sc.)

## 4. Language competence/skills (fluent, average, basic skills)

Hindi, English (fluent)

## 5. Special Course

Professional Training at the department of Chemistry, School of Chemical Technology, Aalto University, Finland

## 6. Professional Employment

2012 – 2013 National Institute of Chemical Physics and Biophysics; Engineer  
2009 – 2010 National Institute of Chemical Physics and Biophysics; Engineer

## 7. Main areas of scientific work/Current research topics

Synthesis and magnetic studies of functional oxides.

## 8. Publications

- 1) **Khanduri, H.**; Dimri, M. Chandra; Vasala, S.; Leinberg, S.; Lohmus, R.; Ashworth, T. V.; Mere, A.; Krustok, J.; Karppinen, M.; Stern, R. 2013. Magnetic and structural studies of LaMnO<sub>3</sub> thin films prepared by atomic layer deposition. *J. Phys. D: Appl. Phys.* 46, 175003.
- 2) Dimri, M. Chandra; **Khanduri, H.**; Kooskora, H.; Kodu, M.; Jaaniso, R.; Heinmaa, I.; Mere, A.; Krustok, J.; Stern, R. 2012. Room-temperature ferromagnetism in Ca and Mg stabilized cubic zirconia bulk samples and thin films prepared by pulsed laser deposition. *J. Phys. D: Appl. Phys.* 45, 475003.
- 3) **Khanduri, H.**; Dimri, M. Chandra; Kooskora, H.; Heinmaa, I.; Viola, G.; Ning, H.; Reece, M. J.; Krustok, J.; Stern, R. 2012. Structural, dielectric, magnetic, and nuclear magnetic resonance studies of multiferroic Y-type hexaferrites. *J. Appl. Phys.* 112, 073903.
- 4) Dimri, M. Chandra; **Khanduri, H.**; Kooskora, H.; Subbi, J.; Heinmaa, I.; Mere, A.; Krustok, J.; Stern, R. 2012. Ferromagnetism in rare earth doped cerium oxide bulk samples. *Phys. Status Solidi A* 209, 353–358.
- 5) Dimri, M. Chandra; **Khanduri, H.**; Kooskora, H.; Heinmaa, I.; Joon, E.; Stern, R. 2011. Magnetic properties and <sup>57</sup>Fe NMR studies of U-type hexaferrites. *Journal of Magnetism and Magnetic Materials*, 323, 2210 - 2213.
- 6) Pore, V.; Dimri, M.; **Khanduri, H.**; Stern, R.; Lu, J.; Hultman, L.; Kukli, K.; Ritala, M.; Leskelä, M.; 2011. Atomic layer deposition of ferromagnetic cobalt doped titanium oxide thin films. *Thin Solid Films*, 519, 3318 - 3324.



## **APPENDIX**



## PUBLICATION I

**Khanduri, H.**; Dimri, M. Chandra; Kooskora, H.; Heinmaa, I.; Viola, G.; Ning, H.; Reece, M. J.; Krustok, J.; Stern, R. 2012. Structural, dielectric, magnetic, and nuclear magnetic resonance studies of multiferroic Y-type hexaferrites. *J. Appl. Phys.* 112, 073903.



## Structural, dielectric, magnetic, and nuclear magnetic resonance studies of multiferroic Y-type hexaferrites

H. Khanduri,<sup>1,2,a)</sup> M. Chandra Dimri,<sup>1</sup> H. Kooskora,<sup>1</sup> I. Heinmaa,<sup>1</sup> G. Viola,<sup>3</sup> H. Ning,<sup>3</sup> M. J. Reece,<sup>3</sup> J. Krustok,<sup>2</sup> and R. Stern<sup>1</sup>

<sup>1</sup>National Institute of Chemical Physics and Biophysics, Tallinn-12618, Estonia

<sup>2</sup>Tallinn University of Technology, Tallinn-19086, Estonia

<sup>3</sup>School of Engineering and Materials Science, Queen Mary University of London, Mile End Road, London E1 4NS, United Kingdom

(Received 29 March 2012; accepted 24 August 2012; published online 1 October 2012)

The effect of strontium substitution on structural, magnetic, and dielectric properties of a multiferroic Y-type hexaferrite (chemical formula  $\text{Ba}_{2-x}\text{Sr}_x\text{Mg}_2\text{Fe}_{12}\text{O}_{22}$  with  $0 \leq x \leq 2$ ) was investigated. Y-type hexaferrite phase formation was not affected by strontium substitution for barium, in the range  $0 \leq x \leq 1.5$ , confirmed by x-ray diffraction and Raman spectroscopy measured at room temperature. Two intermediate magnetic spin phase transitions (at temperatures  $T_I$  and  $T_{II}$ ) and a ferrimagnetic-paramagnetic transition (at Curie temperature  $T_C$ ) were identified from the temperature dependence of the magnetic susceptibility. Magnetic transition temperatures ( $T_I$ ,  $T_{II}$ , and  $T_C$ ) increased with increasing strontium content. Magnetic hysteresis measurements indicated that by increasing strontium concentration, the coercivity increases, while the saturation magnetization decreases. The  $^{57}\text{Fe}$  NMR spectrum of the Y-type hexaferrite measured at 5 K and in zero magnetic field showed remarkable differences compared to that of other hexaferrites due to their different number of tetrahedral and octahedral iron sites. The temperature and frequency dependence of the dielectric permittivity evidenced broad peaks with frequency dispersion in correspondence of the Curie temperature. © 2012 American Institute of Physics. [<http://dx.doi.org/10.1063/1.4754532>]

### I. INTRODUCTION

Hexagonal ferrites are largely used in different types of electronic and microwave devices due to their versatile magnetic properties.<sup>1–5</sup> Hexaferrites are subdivided into six types, according to their chemical formula and structure, namely M-, W-, Y-, Z-, X-, and U-type.<sup>6,7</sup> Most hexaferrites have M-type structure as one of the basic units. This has the simplest structure among the other six variants and is composed of R and S blocks. The R block has the stoichiometry  $\text{BaFe}_6\text{O}_{11}$ , with five octahedral sites of two different types and one trigonal bipyramidal site. The S unit is formed by two formula units of  $\text{Fe}_3\text{O}_4$  with the spinel structure containing two tetrahedral and four octahedral cation sites. Y-type hexaferrites are derived from S and T blocks.<sup>7–9</sup> The T unit has four layers with formula  $\text{Ba}_2\text{Fe}_8\text{O}_{14}$ , where Fe ions occupy two tetrahedral sites, and six octahedral sites of two different types (Fig. 1). Magnetic spin blocks stack along the c axis, with alternating large ( $\mu_L$ ) and small ( $\mu_S$ ) magnetic moments of opposite direction, produce collinear ferrimagnetism even at high temperatures exceeding room temperature. Decreasing the temperature, Y-type hexaferrites undergo transitions from a collinear ferrimagnetic phase to a proper-screw spin phase, and at lower temperature, from screw spin phase to a longitudinal conical spin phase (see Fig. 1).<sup>10</sup>

Y- and Z-type hexaferrites attracted large interest in recent years due to the observation of magnetoelectric effects,<sup>9–13</sup> the possibility of tailoring magnetic properties by

varying doping and sintering conditions,<sup>14</sup> and the recent discovery of ferroelectricity.<sup>9,10,15</sup> Ferroelectricity in a Y-type hexaferrite system ( $\text{Ba}_{0.5}\text{Sr}_{1.5}\text{Zn}_2\text{Fe}_{12}\text{O}_{22}$ ) was first reported by Kimura *et al.*<sup>9</sup> At ambient conditions and zero magnetic field,  $\text{Ba}_{0.5}\text{Sr}_{1.5}\text{Zn}_2\text{Fe}_{12}\text{O}_{22}$  is a nonferroelectric insulator with noncollinear spin arrangement. In an applied magnetic field, it undergoes several phase transitions and some of the phases exhibit ferroelectricity induced by a critical magnetic field of 0.3–0.8 T.<sup>9,16,17</sup> Ferroelectricity was also observed in  $\text{Ba}_2\text{Mg}_2\text{Fe}_{12}\text{O}_{22}$  and  $\text{Ba}_2(\text{Mg}_{1-x}\text{Zn}_x)_2\text{Fe}_{12}\text{O}_{22}$  Y-type hexaferrites, where the critical magnetic field to induce the ferroelectricity was dramatically reduced to 30 mT.<sup>10,18</sup> Chun *et al.*<sup>18</sup> partially substituted Fe with Al in  $\text{Ba}_{0.5}\text{Sr}_{1.5}\text{Zn}_2(\text{Fe}_{1-x}\text{Al}_x)_{12}\text{O}_{22}$  and successfully induced the ferroelectric phase at 1 mT.

In order to further explore the interesting properties of  $\text{Mg}_2\text{Y}$  hexaferrites ( $\text{Ba}_2\text{Mg}_2\text{Fe}_{12}\text{O}_{22}$ ), we investigated the effect of strontium substitution on structure, magnetic transition temperatures, and dielectric behaviour of  $\text{Ba}_{2-x}\text{Sr}_x\text{Mg}_2\text{Fe}_{12}\text{O}_{22}$  ( $0 \leq x \leq 2$ ), prepared by chemical solution method. Strontium was chosen because it has good solubility in Y-type barium hexaferrite, and it has also shown to improve the magnetic properties of Y-type hexaferrites.<sup>19</sup>

### II. EXPERIMENTAL

Polycrystalline powder samples of  $\text{Ba}_{2-x}\text{Sr}_x\text{Mg}_2\text{Fe}_{12}\text{O}_{22}$  (with  $x=0, 0.5, 1, 1.5$ , and 2) were prepared by chemical citrate solution method.<sup>20,21</sup> Initially, the aqueous solutions (0.5M) of  $\text{Ba}(\text{NO}_3)_2$ ,  $\text{SrCO}_3$ ,  $\text{MgO}$ ,  $\text{Fe}(\text{NO}_3)_3 \cdot 9\text{H}_2\text{O}$ , and citric acid were prepared separately in deionised water. These solutions were mixed and the pH of the resulting solution was

<sup>a)</sup>Author to whom correspondence should be addressed. Electronic mail: himani.khanduri@gmail.com.

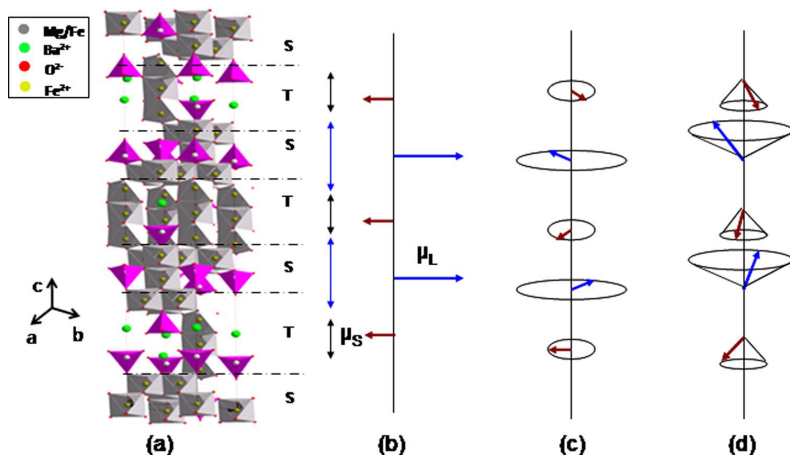


FIG. 1. (a) Schematic crystal structure of Y-type hexaferrite; (b) the ferrimagnetic structure consists of alternate stacks of two spin blocks with  $\mu_L$  (larger magnetic moments) and  $\mu_S$  (small magnetic moments) along c axis. (c) and (d) represent the proper screw structure and longitudinal conical spin order states respectively exhibited at lower temperatures.<sup>10,11</sup>

made neutral or slightly alkaline ( $pH = 7-8$ ) by adding ammonia solution. The solution was heated on hot plate with constant stirring until auto-combustion. The resulting powders were heated at  $500^\circ\text{C}$  for 3 h to remove the organic impurities. The powders were pressed in disc shape pellets and sintered at  $1200^\circ\text{C}$  for 5 h in air.

Powder x-ray diffraction and Raman spectroscopy were used for phase identification. The x-ray diffraction was carried out using a Philips x-ray diffractometer. Raman spectroscopy (Horiba Jobin Yvon Labram HR 800) was performed at room temperature on sintered samples. Vibrating sample magnetometer (VSM, Quantum Design's 14T-PPMS) was used to measure the magnetic susceptibility and hysteresis loops of the sintered and crushed powder samples. The temperature dependence of magnetization was measured in a broad temperature range ( $10-850\text{ K}$ ). Magnetic hysteresis loops were measured in the range  $10-400\text{ K}$ . The solid state NMR ( $^{57}\text{Fe}$ ) spectra were measured using the Fourier transform spin echo technique on Bruker AVANCE II NMR spectrometer. The spectra were recorded at  $T = 5\text{ K}$  in zero external field, because the signal was noisy and weak at room temperature. The excitation frequency was varied from 69 to 77 MHz in steps of 0.1 MHz to cover the full broad spectral range of lines corresponding to different typical crystallographic iron sites in hexaferrites. For the dielectric measurements, the disk shape pellets were coated with silver electrodes. The temperature dependence of the dielectric permittivity and loss was measured at various frequencies from 1 to 100 kHz using a precision LCR meter (Agilent, 4284A) connected to a high temperature tube furnace.

### III. RESULTS AND DISCUSSION

#### A. Phase identification

Figure 2 shows the XRD patterns of the samples calcined at  $1200^\circ\text{C}/5\text{ h}$ . The x-ray diffractograms reveal that samples  $\text{Ba}_{2-x}\text{Sr}_x\text{Mg}_2\text{Fe}_{12}\text{O}_{22}$  (with  $x = 0, 0.5, 1, 1.5$ ) have pure Y-type hexagonal structure, whereas  $\text{Sr}_2\text{Mg}_2\text{Fe}_{12}\text{O}_{22}$  ( $x = 2$ ) does not exhibit single phase Y-type structure and

was therefore not examined in details in the present study. This is consistent with previous structural studies on  $\text{Zn}_2\text{Y}$  hexaferrites,<sup>19</sup> where the maximum solubility of strontium in the  $\text{Ba}_{2-x}\text{Sr}_x\text{Zn}_2\text{Fe}_{12}\text{O}_{22}$  ferrite was found to be about 1.8, and complete substitution of  $\text{Ba}^{2+}$  by  $\text{Sr}^{2+}$  prevented the Y-type phase formation.

Lattice parameters of  $\text{Ba}_{2-x}\text{Sr}_x\text{Mg}_2\text{Fe}_{12}\text{O}_{22}$  (with  $x = 0, 0.5, 1, 1.5$ ) calculated and listed in Table I confirmed Y-type hexaferrite phase. The value of lattice parameter "a" decreased with the rise of Sr content, since the ionic radius of  $\text{Sr}^{2+}$  ( $1.32\text{ \AA}$ ) is smaller compared to  $\text{Ba}^{2+}$  ( $1.49\text{ \AA}$ ). The  $c/a$  ratio increased with increasing strontium content.

The Raman spectra measured at room temperature in Fig. 3 also confirm that  $\text{Ba}_{2-x}\text{Sr}_x\text{Mg}_2\text{Fe}_{12}\text{O}_{22}$  samples exhibit a hexaferrite structure.<sup>22-25</sup> In our knowledge, there are not many Raman studies on Y-type hexaferrites, except a recent publication on  $\text{Zn}_2\text{Y}$  hexaferrite.<sup>26</sup> Raman peaks become broader with the increase of the value of  $x$  from 0 to 1.5 (Fig. 3). Changes in chemical composition, atomic radii, valence, bond length, cell size, and magnetic order might lead to the broadening of Raman peaks.<sup>27</sup> In our samples,

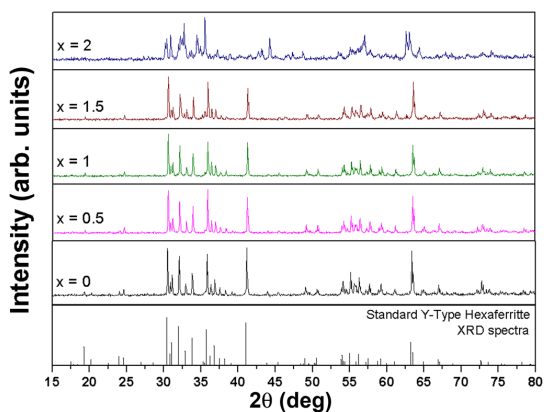


FIG. 2. X-ray diffraction patterns of  $\text{Ba}_{2-x}\text{Sr}_x\text{Mg}_2\text{Fe}_{12}\text{O}_{22}$  powder samples.

TABLE I. Lattice parameters for different Sr concentration in the  $Ba_{2-x}Sr_xMg_2Fe_{12}O_{22}$  samples (with estimated errors).

Value of x in $Ba_{2-x}Sr_xMg_2Fe_{12}O_{22}$	a (Å) (1%)	c (Å) (0.5%)	c/a
0	5.866	43.2683	7.376
0.5	5.8548	43.3514	7.404
1	5.8436	43.2799	7.406
1.5	5.8436	43.2799	7.406

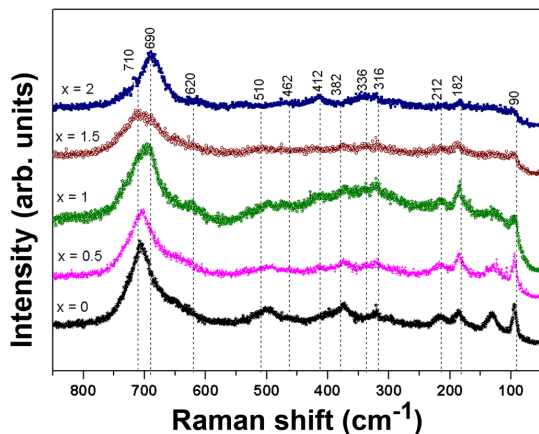


FIG. 3. Raman spectra of  $Ba_{2-x}Sr_xMg_2Fe_{12}O_{22}$  bulk samples.

peak broadening may be related to changes in magnetic structure on strontium substitution.

## B. Magnetic studies

The magnetic phase transition temperatures in  $Ba_{2-x}Sr_xMg_2Fe_{12}O_{22}$  for different strontium content ( $x=0$ ,

0.5, 1, 1.5) were determined from the temperature dependence of magnetic susceptibility measured in an applied magnetic field of 0.1 T (Fig. 4). The ferrimagnetic-paramagnetic transition (Curie temperature,  $T_C$ ) was identified as the temperature where the magnetic susceptibility significantly dropped. The two visible susceptibility peaks in correspondence of temperatures  $T_I$  and  $T_{II}$  (Fig. 4) are associated with the consecutive magnetic spin transitions. Decreasing the temperature, the magnetic order changes from collinear ferrimagnetic to a proper-screw spin phase at transition temperature II, and from screw spin phase to a longitudinal conical spin phase around transition temperature I (see also Fig. 1), as recently suggested for  $Ba_2Mg_2Fe_{12}O_{22}$  ( $x=0$ ) based on neutron diffraction.<sup>28,30</sup> The magnetic transition temperatures of different samples of  $Ba_{2-x}Sr_xMg_2Fe_{12}O_{22}$  are given in Table II. It can be seen that all the magnetic transition temperatures increase with increasing Sr content.

Figure 5 shows the magnetic hysteresis loops of  $Ba_{2-x}Sr_xMg_2Fe_{12}O_{22}$  measured at 300 K for different strontium content ( $x=0, 0.5, 1, 1.5$ ). Coercivity was found to be increased with strontium concentration (for  $x=1.5$ , the coercivity is two times larger than in case of  $x=0$ ). Similar behaviour in coercivity was also found by other research groups on Sr substitution in Y-type hexaferrites.<sup>19,29</sup> The ground state magnetic structure of these hexaferrites  $\{(BaSr)_2Mg_2Fe_{12}O_{22}, (BaSr)_2Zn_2Fe_{12}O_{22}\}$  is composed of alternating stacking of the L and S blocks along the c axis.<sup>31</sup> The magnetic moments of Fe sites lying in the ab plane are in collinear ferrimagnetic structures, within these blocks. The Sr-free sample shows the collinear ferrimagnetic order at room temperature, whereas the antiferromagnetic order increased with the increase in Sr content. The enhancement in antiferromagnetic order for higher concentration ( $x=1.5$ ) results in increased coercivity, whereas the composition  $x=1$  shows slight decrease in coercivity, possibly due to an

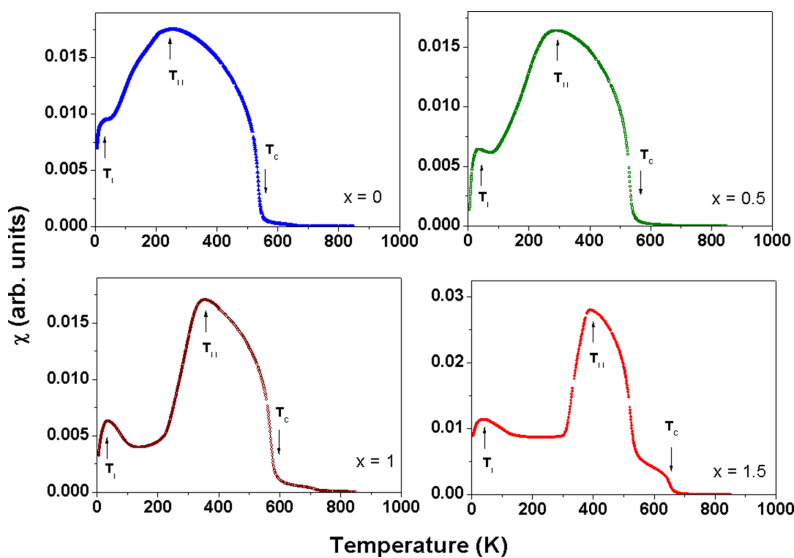


FIG. 4. Temperature dependence of susceptibility for  $Ba_{2-x}Sr_xMg_2Fe_{12}O_{22}$  samples.

TABLE II. Coercivities and magnetic transition temperatures (with average estimated errors) of the powder samples of  $\text{Ba}_{2-x}\text{Sr}_x\text{Mg}_2\text{Fe}_{12}\text{O}_{22}$ .

Value of $x$ in $\text{Ba}_{2-x}\text{Sr}_x\text{Mg}_2\text{Fe}_{12}\text{O}_{22}$	Coercivity $H_c$ (Oe)	Transition temperatures (K)		
		$T_1$ ( $\pm 5$ K)	$T_{11}$ ( $\pm 10$ K)	$T_c$ (K) ( $\pm 5$ K)
0	100	20	260	550
0.5	150	30	290	550
1	100	35	355	590
1.5	200	40	390	670

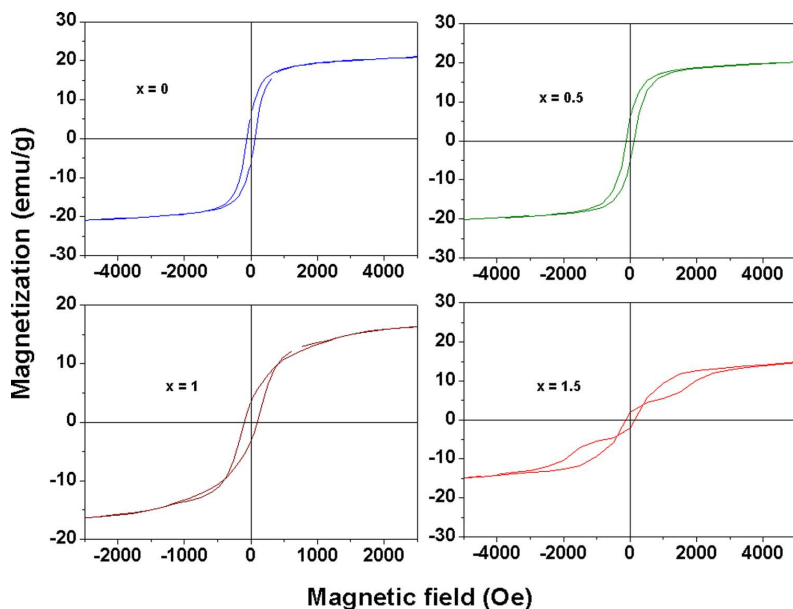
intermediate phase (between proper-screw and conical spin phase) and magnetic frustrations existing at this composition. Enhancement in coercivity in antiferromagnetic phase is understandable, because it needs higher demagnetizing fields as compared to ferrimagnetic material. At room temperature,  $\text{Ba}_{2-x}\text{Sr}_x\text{Mg}_2\text{Fe}_{12}\text{O}_{22}$  samples with compositions  $x=0$  and  $x=0.5$  are still in collinear ferrimagnetic phase (show single ferrimagnetic loop), while samples with  $x=1$  and  $x=1.5$  have entered already in the screw spin phase (showed triple loops). The abnormal triple loops are related to the changes in the magnetic phases and intermediate phases produced by strontium substitution in  $\text{Ba}_{2-x}\text{Sr}_x\text{Mg}_2\text{Fe}_{12}\text{O}_{22}$  samples. Kimura *et al.* had also observed the phase change from collinear ferrimagnetic to antiferromagnetic state, with other intermediate phases, depending on Sr substitution for barium ions in  $\text{Zn}_2\text{Y}$  hexaferrites.<sup>9</sup> Our  $\text{Ba}_{2-x}\text{Sr}_x\text{Mg}_2\text{Fe}_{12}\text{O}_{22}$  samples with higher strontium concentration ( $x=1$  and  $1.5$ ) exhibit an intermediate magnetic phase in between proper screw spin phase and conical spin phase at room temperature. This intermediate phase could be responsible for multi-stage abnormal hysteresis loop. This kind of loops has been observed in  $\text{Ba}_2\text{Mg}_2\text{Fe}_{12}\text{O}_{22}$  samples (at 10 K) by Sagayama *et al.*,<sup>30</sup> and they attributed it to the phase transition of the

magnetic structure, which was supported by neutron diffraction studies at low temperatures.<sup>30</sup>

In order to study the magnetic behaviour of the different magnetic phases, magnetic hysteresis loops of  $\text{Ba}_{0.5}\text{Sr}_{1.5}\text{Mg}_2\text{Fe}_{12}\text{O}_{22}$  were measured at selected representative temperatures in the range 10–400 K (Fig. 6). Figs. 6(a) and 6(b) show the magnetic hysteresis at 10 and 30 K, respectively, where the conical spin phase is exhibited. In the range 200–350 K, the sample has a screw spin phase and it shows triple M-H loops (Figs. 6(c)–6(e)). At 400 K,  $\text{Ba}_{0.5}\text{Sr}_{1.5}\text{Mg}_2\text{Fe}_{12}\text{O}_{22}$  sample has collinear ferrimagnetic order and the magnetic hysteresis curve shows the typical ferrimagnetic behaviour (Fig. 6(f)).

### C. NMR measurements on $\text{Ba}_2\text{Mg}_2\text{Fe}_{12}\text{O}_{22}$

The  $^{57}\text{Fe}$  NMR spectrum of  $\text{Ba}_2\text{Mg}_2\text{Fe}_{12}\text{O}_{22}$  measured at 5 K in zero applied magnetic field is shown in Fig. 7. The NMR spectrum is noisy and broad, consistent with previous NMR measurements on Y-type hexaferrites.<sup>32</sup> Y-type hexaferrites have six sublattice sites ( $6c_{IV}$ ,  $3a_{VI}$ ,  $18h_{VI}$ ,  $6c_{VI}$ ,  $6c_{IV^*}$ , and  $3b_{VI}$ ),<sup>32</sup> which could not be distinguished in our NMR spectrum. In case of M-type<sup>33</sup> and U-type<sup>34</sup> barium hexaferrites, the NMR

FIG. 5. Hysteresis loops measured at 300 K of  $\text{Ba}_{2-x}\text{Sr}_x\text{Mg}_2\text{Fe}_{12}\text{O}_{22}$  samples.

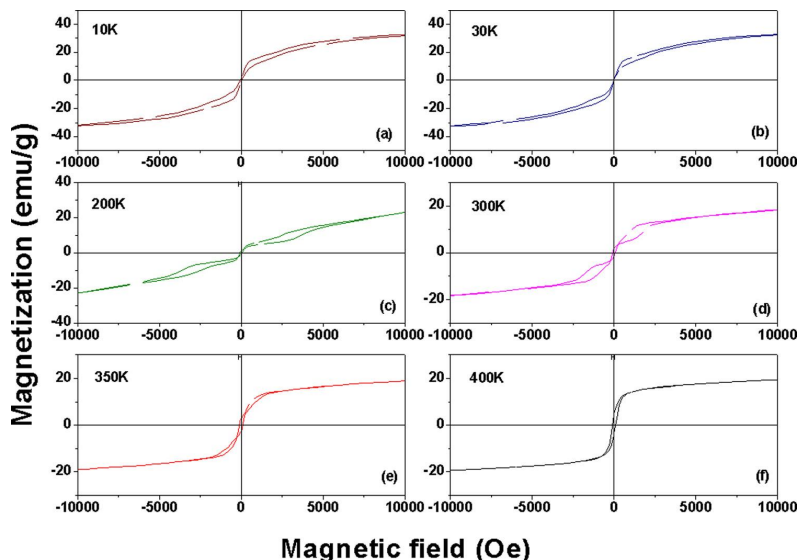


FIG. 6. Hysteresis loops of the powder samples of  $\text{Ba}_{0.5}\text{Sr}_{1.5}\text{Mg}_2\text{Fe}_{12}\text{O}_{22}$  measured at (a) 10 K, (b) 30 K, (c) 200 K, (d) 300 K, (e) 350 K, and (f) 400 K.

spectra consist of five peaks relative to the different lattice iron sites (12 k,  $4f_{IV}$ , 2a,  $4f_{VI}$ , and 2b in M-type and 12 k,  $8f_{IV}$ , 4a,  $4f_{VI}$ , and 2b in U-type hexaferrites). This unresolved spectrum is probably due to a number of different crystallographic (tetrahedral and octahedral) iron sites in the Y-type structure (see Fig. 1). The other reason of broadening may be related to its different magnetic order, because our Y-type hexaferrite samples are in conical spin order at this temperature (5 K), whereas M- and U-type hexaferrites are usually in collinear ferrimagnetic states at that temperature resulting in well resolved NMR spectra.

#### D. Dielectric studies

Figure 8 shows the temperature and frequency dependence of the dielectric permittivity  $\epsilon_r$  and loss ( $\tan\delta$ ) of

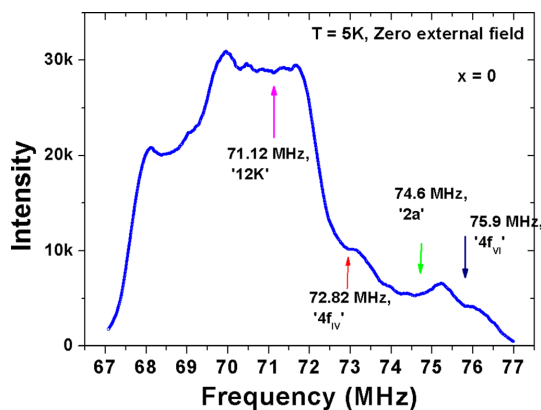


FIG. 7.  $^{57}\text{Fe}$  NMR spectrum of  $\text{Ba}_2\text{Mg}_2\text{Fe}_{12}\text{O}_{22}$  ( $x=0$ ) powder sample measured in zero field at 5 K. The expected lines of different iron sites as observed in M-type spectra are indicated by arrows at different frequencies.

$\text{Ba}_{2-x}\text{Sr}_x\text{Mg}_2\text{Fe}_{12}\text{O}_{22}$ . High dielectric loss is consistent with previous dielectric characterization on Y-type hexaferrites.<sup>35</sup> The dielectric permittivity exhibits very broad peaks in the range 430–680 K (Figs. 8(a)–8(d)). The broadness and position of the peaks changed with strontium content, but no clear trend could be assigned. It is likely that these peaks are associated with the Curie (ferrimagnetic-paramagnetic) transition in the range 550–670 K as previously identified from our magnetic susceptibility data (see Table II). In addition, these peaks showed pronounced frequency dispersion, with the maximum shifting to higher temperature with increasing frequency. Frequency dependent peaks in the dielectric permittivity around the magnetic transition temperatures were also observed in other magnetic systems, such as bilayer manganite ( $\text{Pr}(\text{Sr}_{0.1}\text{Ca}_{0.9})_2\text{Mn}_2\text{O}_7$ )<sup>36</sup> and hexagonal  $\text{ABX}_3$ -type antiferromagnets.<sup>37</sup> In the bilayer manganite, it was observed that the broad anomaly around the Curie temperature had an intrinsic capacitive nature, which was also responsible for the frequency dispersion in the dielectric permittivity.<sup>36</sup> For the hexagonal  $\text{ABX}_3$ -type antiferromagnets, the dielectric anomalies and the strong frequency dispersion observed in  $\text{CsCoBr}_3$  and the weaker dispersion in  $\text{RbCoBr}_3$  were attributed to spin-lattice interaction.<sup>37</sup> Our results suggest that in Y-type hexaferrite too, the perturbation of the magnetic order during heating produces frequency dependent broad peaks in the dielectric constant. This indicates that the dielectric properties are influenced by the magnetic state. The dielectric loss peaks shown in Figs. 8(a)–8(d), also attributed to the transformation of the magnetic order.

An additional anomaly in the dielectric permittivity was observed at higher temperatures in the range 820–890 K, represented by broad or narrower peaks (see out-set of Figs. 8(a)–8(d)). The broadness and position of the peaks did not show any clear trend with strontium content. The position of the permittivity peaks at high temperatures (above 820 K) did not change with varying the frequency. This normally

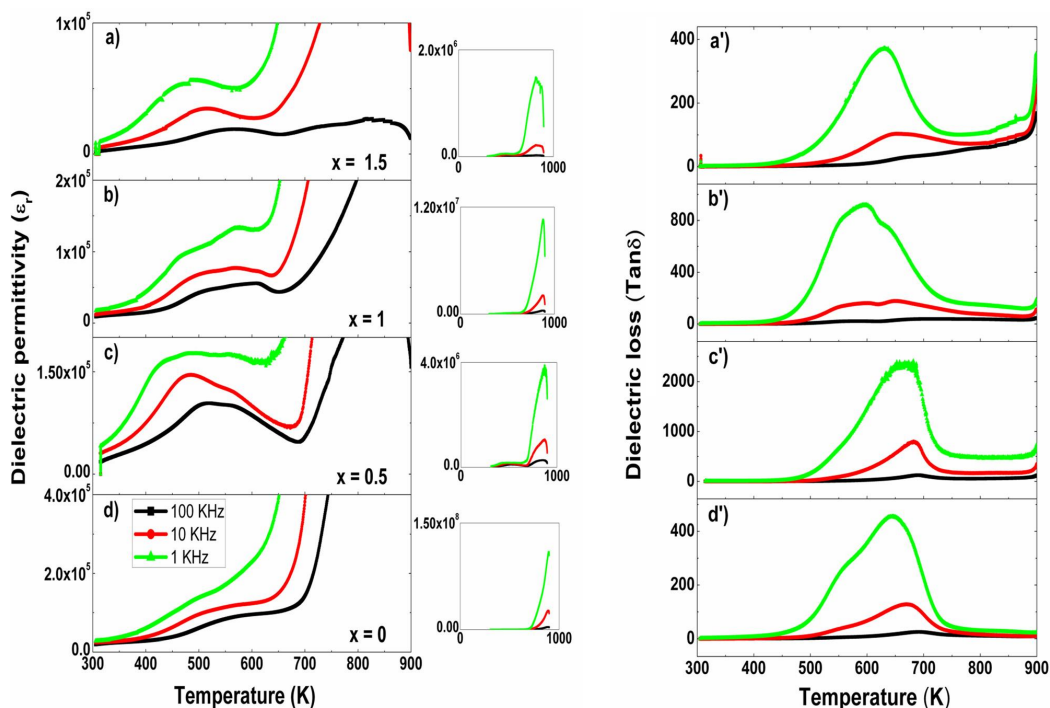


FIG. 8. Temperature dependence of the dielectric permittivity  $\epsilon_r$  and dielectric loss ( $\tan\delta$ ) of  $\text{Ba}_{2-x}\text{Sr}_x\text{Mg}_2\text{Fe}_{12}\text{O}_{22}$  samples measured at different frequencies.

occurs in correspondence of structural modifications, suggesting that the dielectric constant peaks observed probably indicate a phase transition.

#### IV. SUMMARY AND CONCLUSION

$\text{Ba}_{2-x}\text{Sr}_x\text{Mg}_2\text{Fe}_{12}\text{O}_{22}$  samples synthesized by chemical citrate method have single phase Y-type hexaferrite structure in the compositional range  $0 \leq x \leq 1.5$ . Strontium substitution alters the magnetic phase transition temperatures and magnetic hysteresis behaviour. Intermediate spin phase transition temperatures and the Curie temperature (ferrimagnetic-paramagnetic phase transition) shifted to higher temperatures with increasing strontium content. Saturation magnetization decreases and coercivity increases with increasing Sr substitution for Ba ions.  $^{57}\text{Fe}$  NMR spectrum measured at 5 K and in zero magnetic field was found to be broad for the  $\text{Ba}_2\text{Mg}_2\text{Fe}_{12}\text{O}_{22}$  hexaferrite due to a more complex structure when compared to the well resolved NMR spectra for M-type hexaferrites. Broad and frequency dependent peaks were observed in the dielectric permittivity around the Curie temperature, evidencing that a change in the magnetic order affects the dielectric properties.

#### ACKNOWLEDGMENTS

This work was financially supported by the Estonian Science Foundation (Grant Nos.: ETF 8440, MJD 65), and the Estonian targeted financial Grant Nos. SF0690029s09 and SF0690034s09. One of the authors, Himani Khanduri

thanks the DORA program (Estonian Science Foundation) for her doctoral fellowship.

- <sup>1</sup>V. R. K. Murthy, S. Sundaram, and B. Vishwanathan, *Microwave Materials* (Narosa Publishing House, New Delhi, 1993).
- <sup>2</sup>A. Ghasemi, A. Hossienpour, A. Morisako, A. Saatchi, and M. Salehi, *J. Magn. Magn. Mater.* **302**, 429 (2006).
- <sup>3</sup>C. Wang, L. Li, J. Zhou, X. Qi, and Z. Yue, *J. Mater. Sci.: Mater. Electron.* **13**, 713 (2002).
- <sup>4</sup>H.-S. Cho and S.-S. Kim, *IEEE Trans. Magn.* **35**, 3151 (1999).
- <sup>5</sup>S. Sugimoto, S. Kondo, K. Okayama, H. Nakamura, D. Book, T. Kagotani, M. Homma, H. Ota, M. Kimura, and R. Sato, *IEEE Trans. Magn.* **35**, 3154 (1999).
- <sup>6</sup>J. P. Jakubovics, "Magnetism and Magnetic Materials," 2nd Ed. (Institute of Materials, London, 1994).
- <sup>7</sup>J. Smith and H. P. J. Wijn, *Ferrites* (Philips Technical Library, Eindhoven, The Netherlands, 1959), pp. 177–190, 285.
- <sup>8</sup>U. Ozgur, Y. Alivov, and H. Morkoc, *J. Mater. Sci.: Mater. Electron.* **20**, 789 (2009).
- <sup>9</sup>T. Kimura, G. Lawes, and A. P. Ramirez, *Phys. Rev. Lett.* **94**, 137201 (2005).
- <sup>10</sup>S. Ishiwata, Y. Taguchi, H. Murakawa, Y. Onose, and Y. Tokura, *Science* **319**, 1643 (2008).
- <sup>11</sup>S. Ishiwata, Y. Taguchi, Y. Tokunaga, H. Murakawa, Y. Onose, and Y. Tokura, *Phys. Rev. B* **79**, 180408(R) (2009).
- <sup>12</sup>N. Kida, S. Kumakura, S. Ishiwata, Y. Taguchi, and Y. Tokura, *Phys. Rev. B* **83**, 064422 (2011).
- <sup>13</sup>N. Kida, D. Okuyama, S. Ishiwata, Y. Taguchi, R. Shimano, K. Iwasa, T. Arima, and Y. Tokura, *Phys. Rev. B* **80**, 220406(R) (2009).
- <sup>14</sup>Y. Bai, J. Zhou, Z. Gui, and L. Li, *Mater. Chem. Phys.* **98**, 66 (2006).
- <sup>15</sup>Y. Kitagawa, Y. Hiraoka, T. Honda, T. Ishikura, H. Nakamura, and T. Kimura, *Nature Mater.* **9**, 797 (2010).
- <sup>16</sup>N. Momozawa, Y. Yamaguchi, H. Takei, and M. Mita, *J. Phys. Soc. Jpn.* **54**, 3895 (1985).

- <sup>17</sup>S. Utsumi, D. Yoshiba, and N. Momozawa, *J. Phys. Soc. Jpn.* **76**, 034704 (2007).
- <sup>18</sup>S. H. Chun, Y. S. Chai, Y. S. Oh, D. Jaiswal-Nagar, S. Y. Haam, I. Kim, B. Lee, D. H. Nam, K.-T. Ko, J.-H. Park, J.-H. Park, J.-H. Chung, and K. H. Kim, *Phys. Rev. Lett.* **104**, 037204 (2010).
- <sup>19</sup>Y. Bai, J. Zhou, Z. Gui, and L. Li, *J. Am. Ceram. Soc.* **88**(2), 318 (2005).
- <sup>20</sup>M. C. Dimri, R. Stern, S. C. Kashyap, K. P. Bhatti, and D. C. Dube, *Phys. Status Solidi A* **206**(2), 270 (2009).
- <sup>21</sup>M. C. Dimri, S. C. Kashyap, and D. C. Dube, *Ceram. Int.* **30**, 1623 (2004).
- <sup>22</sup>W. Y. Zhao, P. Wei, W. Wang, and Q. J. Zhang, *J. Appl. Phys.* **103**, 063902 (2008).
- <sup>23</sup>P. B. Braun, *Philips Res. Rep.* **12**, 491 (1957).
- <sup>24</sup>M. S. Chen, Z. X. Shen, X. Y. Liu, and J. Wang, *J. Mater. Res.* **15**, 483 (2000).
- <sup>25</sup>J. Kreisel, G. Lucazeau, and H. Vincent, *J. Solid State Chem.* **137**, 127 (1998).
- <sup>26</sup>S. Kamba, V. Goian, M. Savinov, E. Buixaderas, D. Nuzhnyy *et al.*, *J. Appl. Phys.* **107**, 104109 (2010).
- <sup>27</sup>J. Kreisel, G. Lucazeau, and H. Vincent, *J. Raman Spectrosc.* **30**(2), 115 (1999).
- <sup>28</sup>S. Ishiwata, D. Okuyama, K. Kakurai, M. Nishi, Y. Taguchi, and Y. Tokura, *Phys. Rev. B* **81**, 174418 (2010).
- <sup>29</sup>X. Fang, B. Yang, A. Fen, and Q. Li-Jie, *Chin. Phys. B* **17**(12), 4652 (2008).
- <sup>30</sup>H. Sagayama, K. Taniguchi, N. Abe, T. H. Arima, Y. Nishikawa, S. I. Yano, Y. Kousaka, J. Akimitsu, M. Matsuura, and K. Hirota, *Phys. Rev. B* **80**, 180419(R) (2009).
- <sup>31</sup>T. Kimura, *Annu. Rev. Condens. Matter Phys.* **3**, 93 (2012).
- <sup>32</sup>G. Albanese, *J. Phys. Colloq.* **38**, C1–85 (1977).
- <sup>33</sup>R. L. Streever, *Phys. Rev.* **186**(2), 285 (1969).
- <sup>34</sup>M. C. Dimri, H. Khanduri, H. Kooskora, E. Joon, I. Heinmaa, and R. Stern, *J. Magn. Magn. Mater.* **323**(16), 2210 (2011).
- <sup>35</sup>A. M. Abo El Atta and S. M. Attia, *J. Magn. Magn. Mater.* **257**, 165 (2003).
- <sup>36</sup>B. Ghosh, D. Bhattacharya, A. K. Raychaudhuri, and S. Arumugam, *J. Appl. Phys.* **105**, 123914, (2009).
- <sup>37</sup>K. Morishita, K. Iio, T. Mitsui, and T. Kato, *J. Magn. Magn. Mater.* **226**, 579 (2001).



## **PUBLICATION II**

Dimri, M Chandra; **Khanduri, H.**; Kooskora, H.; Kodu, M.; Jaaniso, R.; Heinmaa, I.; Mere, A.; Krustok, J.; Stern, R. 2012. Room-temperature ferromagnetism in Ca and Mg stabilized cubic zirconia bulk samples and thin films prepared by pulsed laser deposition. *J. Phys. D: Appl. Phys.* 45, 475003.



# Room-temperature ferromagnetism in Ca and Mg stabilized cubic zirconia bulk samples and thin films prepared by pulsed laser deposition

M Chandra Dimri<sup>1</sup>, H Khanduri<sup>1,2</sup>, H Kooskora<sup>1</sup>, M Kodu<sup>3</sup>, R Jaaniso<sup>3</sup>, I Heinmaa<sup>1</sup>, A Mere<sup>2</sup>, J Krustok<sup>2</sup> and R Stern<sup>1</sup>

<sup>1</sup> National Institute of Chemical Physics and Biophysics, Tallinn-12618, Estonia

<sup>2</sup> Department of Physics, Faculty of Science, Tallinn University of Technology, Tallinn-19086, Estonia

<sup>3</sup> Institute of Physics, Faculty of Science and Technology, University of Tartu, EE-51014, Tartu, Estonia

E-mail: [mukeshdimri@yahoo.com](mailto:mukeshdimri@yahoo.com)

Received 20 June 2012, in final form 2 October 2012

Published 1 November 2012

Online at [stacks.iop.org/JPhysD/45/475003](http://stacks.iop.org/JPhysD/45/475003)

## Abstract

We report room-temperature ferromagnetism in Ca and Mg stabilized zirconia bulk samples and thin films. Powders were prepared by the citrate-combustion route, and thin films grown on silicon substrates by the pulsed laser deposition technique. X-ray diffractograms and Raman spectra at room temperature reveal the formation of cubic phase zirconia. The observed ferromagnetism is robust at room temperature in both bulk as well as in thin film samples, although it is weaker in thin films. The origin of the ferromagnetism can be related to oxygen vacancies created due to divalent (calcium and magnesium) substitution for tetravalent zirconium ions.

(Some figures may appear in colour only in the online journal)

## 1. Introduction

Dilute magnetic semiconductors (DMS) have attracted vast interest in the last decade because of the possibility of assembling charge and spin degrees of freedom in a single substance. That makes them promising candidates for technological applications in spintronic devices, utilizing both the electronic charge as well as their spins [1–3]. With this hope to realize spintronic devices such as spin valves, spin transistors, spin light-emitting diodes (LEDs), ultrafast optical switches, etc, a significant amount of research effort has been focused on discovering materials suitable for these applications. A large number of transition metal (TM) doped oxides have been examined since the first prediction of ferromagnetism in Mn-doped ZnO by Dietl *et al* in 2000 [2]. A remarkable amount of research has been carried out to understand the nature of magnetism in TM-doped oxide systems, such as ZnO, TiO<sub>2</sub>, HfO<sub>2</sub>, CeO<sub>2</sub>, SnO<sub>2</sub> and In<sub>2</sub>O<sub>3</sub> [4–9]. However, the experimental search for

ferromagnetism in TM-doped oxide materials has not yet resulted in reproducible and homogeneous magnetic materials.

Interestingly, ferromagnetism has been suggested to be possible even in systems that do not contain magnetic impurities, materials often referred to as  $d^0$  or intrinsic ferromagnets [10, 11]. Experimentally, it has been shown that thin films of HfO<sub>2</sub> and ZnO [12, 13] exhibit such type of ferromagnetism with a rather high Curie temperature ( $T_C$ ). The ferromagnetism with high Curie temperature was also proposed by substitution of the four-valent cation  $A^{4+}$  in dioxides such as AO<sub>2</sub> ( $A = \text{Ti, Zr, or Hf}$ ) by a monovalent cation of group IA of the periodic table [11]. HfO<sub>2</sub> and ZrO<sub>2</sub> are both wide-band insulating materials with a high dielectric constant; the possibility of making them ferromagnetic could widen their possible application in the emerging field of spintronics.

Recent theoretical studies also predicted high-temperature ferromagnetism in TM-doped cubic zirconia [14] and K-doped ZrO<sub>2</sub> [11]. However, doping with Cu [15], Cr [14] or Ca

[11] in  $ZrO_2$  can result in paramagnetism, antiferromagnetic or non-magnetic ground states, respectively. According to these theories, single oxygen vacancy induces local magnetic moments on the neighbouring oxygen atoms, which then interact with extended exchange coupling. Motivated by these promising theoretical predictions of ferromagnetism in doped  $ZrO_2$ , a few experimental works have been carried out to confirm the room-temperature ferromagnetism in  $Zr_{1-x}Mn_xO_2$  [16–18] and  $Zr_{1-x}Fe_xO_2$  [19]. However, experimental results were controversial in these studies, and ferromagnetism was not shown up to the level, which has been predicted. Our recent experimental study on Mn-doped  $ZrO_2$  [17] suggested that an undesired secondary phase like  $Mn_3O_4$  segregates on high-temperature heat treatments. To overcome the problems related to secondary phases, we study further the possibility of ferromagnetism in  $ZrO_2$  stabilized with non-magnetic elements such as Ca or Mg, as they are well soluble in the zirconia matrix and their magnetic properties have not yet been investigated experimentally.

In this paper, we report the ferromagnetic properties observed in cubic zirconia stabilized with non-magnetic dopants (Ca, Mg and Y). Accordingly, we synthesized bulk and thin films of Ca, Y and Mg stabilized cubic zirconia, and studied their structural and magnetic properties to understand the dopant effects. Optimum dopant concentrations (16 at% Ca and 14 at% Mg in  $ZrO_2$ ) were selected from the phase diagrams reported in the literature to get the cubic crystalline phase at room temperature [20, 21]. Y-stabilized cubic zirconia (YSZ) samples were found to be paramagnetic, so the results are not discussed in this paper.

## 2. Experimental

Polycrystalline powders of  $Zr_{1-x}Ca_xO_2$  ( $x = 0$  and 0.16) and  $Zr_{0.86}Mg_{0.14}O_2$  were prepared by the chemical citrate-combustion route [17]. Zirconyl oxychloride ( $ZrOCl_2 \cdot 8H_2O$ ), CaO and MgO were used as starting materials. 0.5M solutions were prepared in deionized water for zirconium salt, whereas CaO and MgO were dissolved in excess of nitric acid and peroxide. Citric acid was added in 3 : 2 proportions for every cation. The resulting solution after mixing was first heated at 60 °C for 2 h and later at 80 °C till the complete evaporation of solvents. All our as-prepared powders were calcined at 800 °C in air for 5 h. To see the effects of annealing in other environments than air, the as-prepared powder samples were alternatively calcined in argon/hydrogen environments at 800 °C/5 h. The calcined powders were pressed to disc-shaped pellets and sintered in air at either 1200 or 1500 °C for 3 h, to investigate the dependence of structural and magnetic properties on sintering temperatures.

Thin films of 16 at% calcium-doped  $ZrO_2$  were deposited on  $10 \times 10$  mm Si (1 0 0)/SiO<sub>2</sub> (25 nm thermal oxide) substrates by the pulsed laser deposition (PLD) technique. The substrates were ultrasonically cleaned in an acetone bath prior to the deposition process. Pellets that were used as PLD targets were sintered at 1200 °C for 5 h. A KrF excimer laser (COMPexPro 205, Coherent, wavelength 248 nm, pulse width 25 ns) was used for ablation. The deposition conditions of the

$Zr_{1-x}Ca_xO_2$  films were as follows: laser pulse energy density on the target  $2 J cm^{-2}$ , repetition rate of laser 5 Hz, substrate temperature 800 °C, the distance between the substrate and the target 7.5 cm. Ca-doped  $ZrO_2$  thin films were deposited at three different oxygen pressures in the chamber during the film growth:  $10^{-2}$ ,  $10^{-3}$  and  $10^{-4}$  mbar. The number of laser impulses for growing each film were 30 000 and the resulting thicknesses of the films were  $\sim 150$  nm.

The x-ray diffraction technique (Rigaku Ultima IV) and Raman spectroscopy (Horiba Jobin Yvon LabRAM HR 800) were used for structural identification at room temperature, whereas magnetic measurements were performed using a vibrating sample magnetometer (14 T PPM-Quantum Design). Scanning electron micrographs (SEM) for microstructure and energy dispersive spectroscopic (EDS) measurements for stoichiometry were also made for those samples using a Zeiss EVO-MA15 apparatus.

## 3. Results and discussion

X-ray diffraction patterns for the undoped as well as Ca- and Mg-doped  $ZrO_2$  bulk samples, heated at different temperatures are shown in figure 1(a). From these diffractograms we see that 16 at% Ca- and 14 at% Mg-doped  $ZrO_2$  samples sintered at 1500 °C exhibit a pure cubic (C) zirconia phase. The undoped sample sintered at 800 °C shows a monoclinic structure with an extra peak of tetragonal zirconia, whereas a single-phase monoclinic structure is exhibited by the sample sintered at 1500 °C. The lower, 10 at% Ca-doped zirconia sample shows a mixed cubic and tetragonal (T) structure; the presence of the tetragonal structure in this sample is also confirmed by the Raman spectra (figure not included). Figure 1(b) shows the diffractograms for the PLD thin films of the 16 at% Ca-doped  $ZrO_2$ , grown at different oxygen partial pressures. The films show one XRD peak for cubic zirconia (1 1 1) and other intense peaks from the silicon substrate. Raman spectra (see figure 2(b)) also confirm the cubic phase formation for thin films showing a characteristic cubic XRD pattern.

Raman spectra measured at room temperature for the bulk and thin film samples of doped zirconia are shown in figures 2(a) and (b). The spectrum for 16 at% Ca-doped  $ZrO_2$  sintered sample at 1500 °C (figure 2(a)) validates the cubic phase formation (Raman peaks around 275, 410, 520 and  $580 cm^{-1}$ ) [22], whereas the peaks are not separable for both Ca and Mg stabilized zirconia samples heated at 800 °C. These broad and flat spectra may be related to the mixed zirconia phases at 800 °C, although XRD could show single phase for those powders. Usually, the strongest Raman peak position is around  $615 cm^{-1}$  for yttria-stabilized zirconia samples [22], but for Ca-stabilized zirconia this shifts towards lower values, and it is around  $580 cm^{-1}$  in our sample. This shift may be because of the difference in sizes and mass of Ca and Zr, as compared with Y and Zr [22]. Raman spectra for the PLD thin films of 16% Ca-doped  $ZrO_2$  demonstrate characteristic peaks of cubic zirconia ( $155, 425, 620 cm^{-1}$ ); the strong peaks due to the silicon substrate (near 300 and  $530 cm^{-1}$ ) can also be seen in the spectra that suppress the

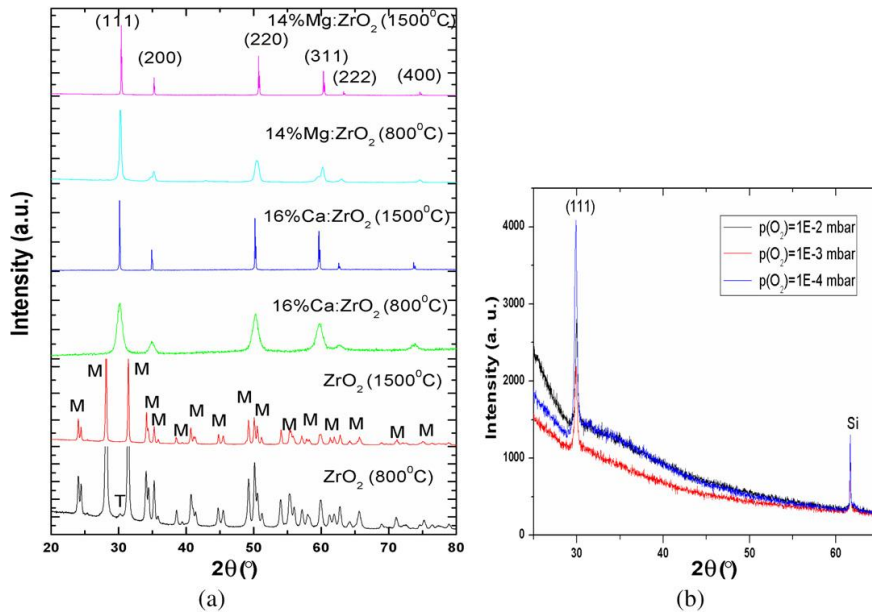


**Figure 1.** XRD patterns of (a) bulk powders heat-treated at different temperatures, (b) 16% Ca-doped ZrO<sub>2</sub> thin films deposited at various oxygen partial pressures.

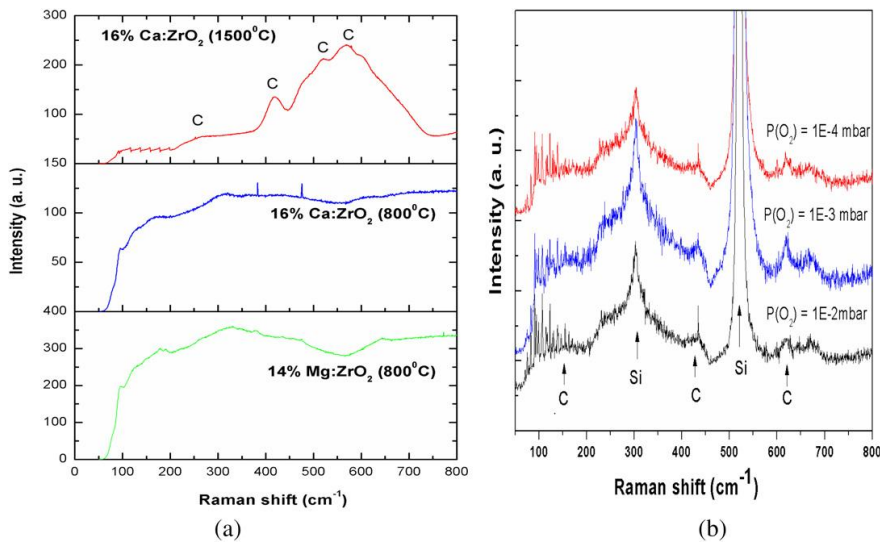


**Figure 2.** Room-temperature Raman spectra of (a) bulk samples of doped ZrO<sub>2</sub>; (b) Zr<sub>0.84</sub>Ca<sub>0.16</sub>O<sub>2</sub> thin films.

intensity of zirconia modes. Our results are consistent with another Raman study by Gazzoli *et al* [23], which showed that above 14% calcium doping stabilizes the cubic zirconia phase and below this doping concentration it results in a tetragonal structure; we have also observed the Raman spectra resembling the tetragonal structure for 10 at% Ca<sup>2+</sup> in ZrO<sub>2</sub> (figure not included).

SEM micrographs and EDX spectra of the undoped and doped zirconia samples sintered at different temperatures

are shown in figure 3. The EDX spectra reveal that the chemical compositions are in good agreement with the desired stoichiometry, and there are no impurities in the prepared samples. From the SEM images we can visualize that all those samples have grains in the micrometre ( $\mu\text{m}$ ) range; however, the grains are smaller ( $\sim 2\text{--}5\ \mu\text{m}$ ) for the samples treated at 800 °C and the undoped sintered sample at 1500 °C, whereas the grains are in the range 3–8  $\mu\text{m}$  for the doped sintered samples at 1500 °C.

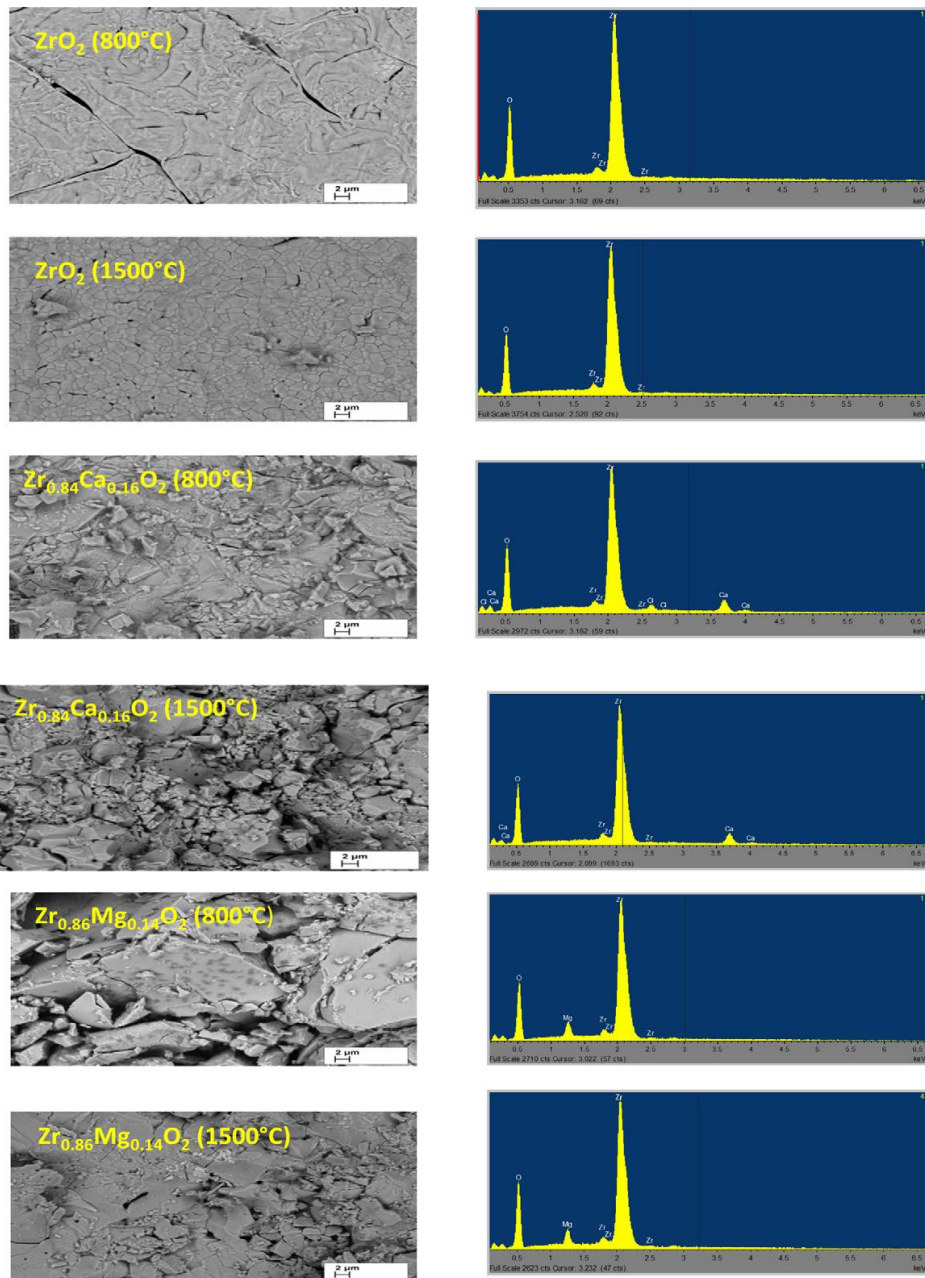


**Figure 3.** SEM micrographs and EDX spectra of the undoped and doped zirconia samples.

Hysteresis loops measured at room temperature (300 K) for the Ca- and Mg-doped and undoped  $ZrO_2$  samples heated at 800 and 1500 °C are shown in figure 4.  $M-H$  loops of the doped zirconia samples appear like a good ferromagnet for the powders heated at 800 °C, whereas the diamagnetism is enhanced in samples sintered at higher temperatures. The enhancement of the diamagnetic signal in the sintered samples

may be due to the decrease in the number of oxygen vacancies on high-temperature treatment in air. The coercivities and spontaneous magnetization (at 0.5 T) estimated from these curves are listed in table 1. There are no remarkable changes in coercivities, whereas the saturation magnetization decreases with the increase in sintering temperatures. The undoped  $ZrO_2$  samples also exhibit tiny ferromagnetic hysteresis, possibly

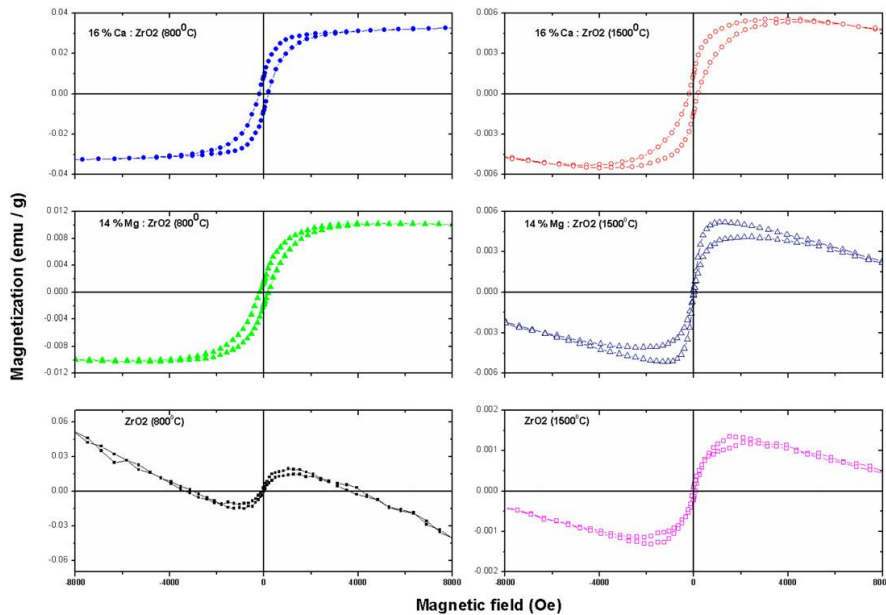


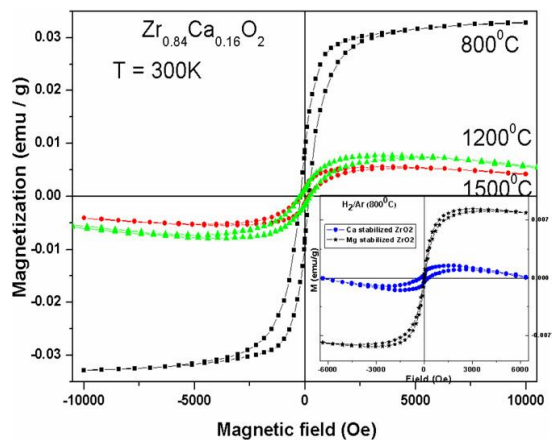
**Figure 4.** As-measured ( $T = 300$  K) hysteresis loops of Ca- and Mg-doped  $ZrO_2$  bulk samples heated at 800 and 1500 °C.

**Table 1.** Magnetic parameters for different Ca- and Mg-doped zirconia samples.

	$Zr_{0.84}Ca_{0.16}O_2$			$Zr_{0.86}Mg_{0.14}O_2$	
	800 °C	1200 °C	1500 °C	800 °C	1200 °C
$M_s$ in $emu\ g^{-1}$ (at 0.5 T)	0.0335	0.0076	0.0055	0.012	0.005
Coercivity (Oe)	200	200	200	185	25

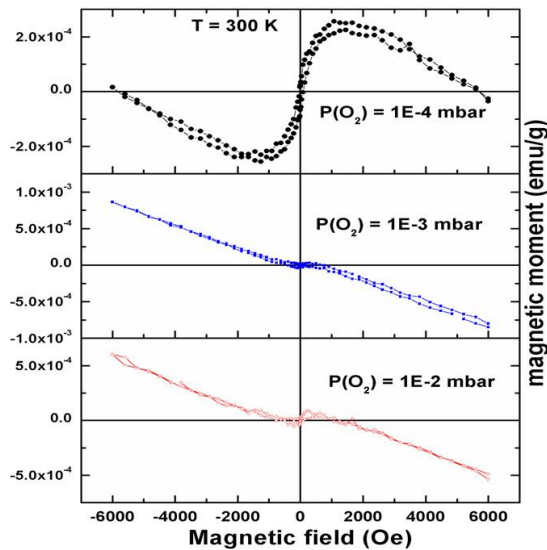
due to the presence of some oxygen vacancies in our samples. The density of oxygen vacancies is strongly dependent on the synthesis methods [24]. Zirconyl oxychloride was used as the zirconium precursor, so there is excess chlorine ( $Cl_2$ ) during the sintering process, which was reported in an old study [24], which showed that preparation by nitrate or oxychloride precursors leads to oxygen vacancies in zirconia; however the vacancies are lower in the samples prepared by oxychloride precursors. This is confirmed from the weak ferromagnetic signal in  $M-H$  measurements (figure 4) due to these oxygen vacancies; however, the oxygen vacancy concentration was not enough to result in long-range ferromagnetic ordering in these undoped samples.

Figure 5 shows the  $M-H$  curves measured at room temperature (300 K) for the  $Zr_{0.84}Ca_{0.16}O_2$  bulk samples annealed at 800, 1200 and 1500 °C/3 h in air. The magnetization decreases with increase in the sintering temperature, whereas the coercivity does not change noticeably. Saturation magnetization is six times larger for the sample annealed at 800 °C, as compared with the sample treated at 1500 °C. These results suggest that vacancies present at lower temperatures enhance the ferromagnetism, which



**Figure 5.** Hysteresis loops (measured at room temperature) of the  $Zr_{0.84}Ca_{0.16}O_2$  bulk samples sintered at different temperatures in air.

diminishes on high-temperature treatments. The decrease in oxygen vacancies on high-temperature treatments results in the lowering of the ferromagnetic order and magnetic moment. There are more vacancies at 800 °C, due to the mixed phase (tetragonal phase as an additional phase), also reported in another study [25]. The decrease in oxygen vacancies on high-temperature treatments are also observed in other studies conducted for photoluminescence [26, 27]. The inset shows the  $M-H$  loops of the Ca- and Mg-doped  $ZrO_2$  samples annealed in a  $H_2$ /argon environment. In order to examine the defect nature of magnetism, annealing in different environments was performed, but even annealing in  $H_2$ /Ar



**Figure 6.**  $M$ - $H$  loops measured (room temperature) for the thin films of  $Zr_{0.84}Ca_{0.16}O_2$  samples grown at different oxygen pressures.

environment could not enhance the long-range ferromagnetic ordering at high temperatures, as expected due to the increasing number of oxygen vacancies. The temperature dependence of magnetization for these samples was also measured in the temperature range 10–350 K (figures not included); it was almost constant and did not show any transition in this temperature range.

Figure 6 shows the dependence of magnetization on the magnetic field at room temperature for  $Zr_{0.84}Ca_{0.16}O_2$  thin films, grown on silicon substrates with different oxygen pressures. The ferromagnetic ordering is quite weak for samples grown at oxygen partial pressures of  $10^{-2}$  and  $10^{-3}$  mbar, whereas the film grown at an oxygen partial pressure of  $10^{-4}$  mbar shows ferromagnetic character. This indicates that the film grown at lower oxygen partial pressures has more oxygen vacancies, available for ferromagnetic ordering. This type of oxygen partial pressure dependence was also observed in doped ZnO and SnO<sub>2</sub> oxide thin films by Hong *et al.*, and in CeO<sub>2</sub> by Singhal *et al.* [28, 29]. There are often significant differences between the properties of bulk samples and thin films due to the effects of the substrate; the magnetic moments are quite low in the thin film samples, as expected. The magnetization does not saturate due to the dominating diamagnetic signal from the silicon substrate, but the value of spontaneous magnetization ( $M$ )  $\sim 2 \times 10^{-4}$  emu g<sup>-1</sup> (at 2000 Oe) and the coercivity is around 80 Oe, and those values are quite low as compared with bulk values (see table 1).

Usually, bulk ZrO<sub>2</sub> is diamagnetic at room temperature. When Ca<sup>2+</sup> or Mg<sup>2+</sup> ions are substituted for zirconium ion (Zr<sup>4+</sup>) sites, compensating anionic vacancies are created in the O<sup>2-</sup> sublattice. These anionic vacancies could be the origin of ferromagnetism in non-magnetic divalent ion doped ZrO<sub>2</sub>. This type of defect induced magnetism has already been observed in thin films of undoped HfO<sub>2</sub>, TiO<sub>2</sub> [12, 30]

and many other nanoparticles [31, 32], usually found in thin films and nanoparticles due to surface effects. However, this type of ferromagnetism in our bulk samples is robust and repeatable (even after months), because the samples are highly crystalline cubic zirconia, obtained on heating at very high temperatures. High-temperature treatments and larger grains ruled out the possibilities of hygroscopic nature and ageing, which have been observed in our recent study on Mn-doped zirconia powders due to low-temperature treatments and nano-sized grains [17].

#### 4. Conclusions

In conclusion, we have observed room-temperature ferromagnetism in Ca and Mg stabilized zirconia bulk samples and similar thin film oriented in [111] direction. X-ray diffraction studies and Raman spectra measured at room temperature reveal the formation of cubic phase zirconia. Bulk powders show good ferromagnetic hysteresis loops, whereas it is weaker in thin films. The origin of the ferromagnetism can be related to oxygen vacancies created due to divalent calcium and magnesium ion substitution for tetravalent zirconium ions.

#### Acknowledgments

This work was financially supported by the Estonian Science Foundation (grant numbers: MJD 65 and ETF 8440), and the Estonian targeted financial grants SF0690029s09 and SF0690034s09. Part of this study was also supported by the European Union through the European Regional Development Fund (Centre of Excellence ‘Mesosystems: Theory and Applications’, TK114).

#### References

- [1] Ohno H 1998 *Science* **281** 951
- [2] Dietl T, Ohno H, Matsukura F, Cibert J and Ferrand D 2000 *Science* **287** 1019
- [3] Matsumoto Y, Murakami M, Shono T, Hasegawa T, Fukumura T, Kawasaki M, Ahmet P, Chikyow T, Koshihara S and Koinuma H 2001 *Science* **291** 854
- [4] Sharma P, Gupta A, Rao K V, Owens F J, Sharma R, Ahuja R, Osorio Guillen J M, Johansson B and Gehring G A 2003 *Nature Mater.* **2** 673
- [5] Bryan J D, Heald S M, Chambers S A and Gamelin D R 2004 *J. Am. Chem. Soc.* **126** 11640
- [6] Coey J M D, Venkatesan M, Stamenov P, Fitzgerald C B and Dorneles L S 2005 *Phys. Rev. B* **72** 024450
- [7] Wen Q Y, Zhang H W, Song Y Q, Qing-Hui Yang, Hao Zhu and John Q Xiao 2007 *J. Phys.: Condens. Matter.* **19** 246205
- [8] Ogale S B *et al* 2003 *Phys. Rev. Lett.* **91** 077205
- [9] Philip J, Theodoropoulou N, Berera G, Moodera J S and Satpati B 2004 *Appl. Phys. Lett.* **85** 777
- [10] Bouzerar G and Ziman T 2006 *Phys. Rev. Lett.* **96** 207602
- [11] Máca F, Kudrnovský J, Drchal V and Bouzerar G 2008 *Appl. Phys. Lett.* **92** 212503
- [12] Venkatesan M, Fitzgerald C B and Coey J M D 2004 *Nature* **430** 630
- [13] Venkatesan M, Fitzgerald C B, Lunney J G and Coey J M D 2004 *Phys. Rev. Lett.* **93** 177206

- [14] Ostanin S, Ernst A, Sandratskii L M, Bruno P, Dane M, Hughes I D, Staunton J B, Hergert W, Mertig I and Kudrnovsky J 2007 *Phys. Rev. Lett.* **98** 016101
- [15] Dutta P, Seehra M, Zhang Y and Wender I 2008 *J. Appl. Phys.* **103** 07D104
- [16] Yu J, Duan L B, Yang Y C and Rao G H 2008 *Physica B* **403** 4264
- [17] Dimri M C, Kooskora H, Pahapill J, Joon E, Heinmaa I, Subbi J and Stern R 2011 *Phys. Status Solidi a* **208** 172
- [18] Hong N H, Park C K, Raghavender A T, Ciftja O, Bingham N S, Phan M H and Srikanth H 2012 *J. Appl. Phys.* **111** 07C302
- [19] Clavel G, Willinger M G, Zioun D and Pinna N 2008 *Eur. J. Inorg. Chem.* **6** 863–8
- [20] Serena S, Sainz M A, Aza S D and Caballero A 2005 *J. Eur. Ceram. Soc.* **25** 681
- [21] Stubican V S and Ray S P 1977 *J. Am. Ceram. Soc.* **60** 534
- [22] Morell G, Katiyar R S, Torres D, Paje S E and Llopis J 1997 *J. Appl. Phys.* **81** 2830
- [23] Gazzoli D, Mattei G and Valigi M 2007 *J. Raman Spectrosc.* **38** 824
- [24] Karapetrova E, Platzer R, Gardner J A, Schutfort E, Sommers J A and Evenson W E 2001 *J. Am. Ceram. Soc.* **84** 65
- [25] Lu X, Liang K, Gu S, Zheng Y and Fang H 1997 *J. Mater. Sci.* **32** 6653
- [26] Xie Y, Ma Z, Liu L, Su Y, Zhao H, Liu Y, Zhang Z, Duan H, Li J and Xie E 2010 *Appl. Phys. Lett.* **97** 141916
- [27] Cong Y, Li B, Yue S M, Fan D and Wang X J 2009 *J. Phys. Chem. C* **113** 13974
- [28] Hong N H, Sakai J, Huong N T, Poirot N and Ruyter A 2005 *Phys. Rev. B* **72** 045336
- [29] Singhal R K, Kumari P, Kumar S, Dolia S N, Xing Y T, Alzamora M, Deshpande U P, Shripathi T and Saitovitch E 2011 *J. Phys. D: Appl. Phys.* **44** 165002
- [30] Kim D, Hong J, Park Y R and Kim K J 2009 *J. Phys.: Condens. Matter* **21** 195405
- [31] Sundaresan A and Rao C N R 2009 *Nano Today* **4** 96
- [32] Coey J M D, Wongsaprom K, Alaria J and Venkatesan M 2008 *J. Phys. D: Appl. Phys.* **41** 134012



## **PUBLICATION III**

**Khanduri, H.;** Dimri, M. Chandra; Vasala, S.; Leinberg, S.; Lohmus, R.; Ashworth, T. V.; Mere, A.; Krustok, J.; Karppinen, M.; Stern, R. 2013. Magnetic and structural studies of LaMnO<sub>3</sub> thin films prepared by atomic layer deposition. *J. Phys. D: Appl. Phys.* 46, 175003.



# Magnetic and structural studies of $\text{LaMnO}_3$ thin films prepared by atomic layer deposition

H Khanduri<sup>1,2,6</sup>, M Chandra Dimri<sup>1</sup>, S Vasala<sup>3</sup>, S Leinberg<sup>4</sup>, R Lõhmus<sup>4</sup>, T V Ashworth<sup>5</sup>, A Mere<sup>2</sup>, J Krustok<sup>2</sup>, M Karppinen<sup>3</sup> and R Stern<sup>1,6</sup>

<sup>1</sup> National Institute of Chemical Physics and Biophysics, Akadeemia tee 23, Tallinn-12618, Estonia

<sup>2</sup> Department of Physics, Faculty of Science, Tallinn University of Technology, Tallinn-19086, Estonia

<sup>3</sup> Department of Chemistry, School of Chemical Technology, Aalto University, FI-00076 Aalto, Finland

<sup>4</sup> Institute of Physics, Faculty of Science and Technology, University of Tartu-51014, Tartu, Estonia

<sup>5</sup> NanoScan AG, Überlandstrasse 129, 8600 Dübendorf, Switzerland

E-mail: [himani.khanduri@gmail.com](mailto:himani.khanduri@gmail.com) and [raivo.stern@kbf.ee](mailto:raivo.stern@kbf.ee)

Received 18 November 2012, in final form 19 February 2013

Published 5 April 2013

Online at [stacks.iop.org/JPhysD/46/175003](http://stacks.iop.org/JPhysD/46/175003)

## Abstract

Here we report the results of structural, microstructural and magnetic property characterizations of both thin films and bulk samples of  $\text{LaMnO}_3$  (LMO). Thin films were deposited by the atomic layer deposition technique on silicon (1 0 0) substrates, whereas bulk samples were prepared by a citrate combustion route. Effects of varying thickness, annealing atmosphere and temperature were studied on both LMO sample classes. Single-phase perovskite crystal structure was confirmed by x-ray diffraction and Raman spectroscopy, in thin films annealed at 700 and 800 °C as well as in bulk samples. Thin films annealed in  $\text{N}_2$  or  $\text{O}_2$  atmosphere do not vary in the crystal structure, but differ by the oxygen stoichiometry, microstructure and magnetic properties. The Curie temperature in all LMO thin films annealed in  $\text{N}_2$  was found to be around 200 K, while it was around 250 K for the films annealed in  $\text{O}_2$  as well as for the bulk samples.

(Some figures may appear in colour only in the online journal)

## 1. Introduction

Lanthanum manganite ( $\text{LaMnO}_3$  or LMO) materials with perovskite structure have gained considerable attention over the last two decades due to their complex magnetic behaviour and colossal magnetoresistance (CMR) effect [1–5]. These exciting properties are due to strong coupling of the charge, lattice and spin degrees of freedom. Stoichiometric  $\text{LaMnO}_3$  is an A-type antiferromagnetic insulator ( $T_N = 139.5$  K), where the orbital ordering is established due to cooperative Jahn–Teller (JT) interactions. Thin films of LMO are used in many devices such as magnetic field sensors, electric field devices, etc. For device applications the films should be of high quality, homogeneous and have smooth surface morphology. Defects, doping and electronic stabilities play a

crucial role in determining the material properties [6, 7]. Even without external cationic doping, LMO has a very rich phase diagram due to its oxygen non-stoichiometry [8, 9]. Particular synthesis methods result in samples with different metal-to-oxygen ratios, and also affect the structural and magnetic properties. LMO thin films typically exhibit ferromagnetic behaviour due to non-stoichiometry [10–12]. Self-doping due to cation vacancies causes mixed Mn valency ( $\text{Mn}^{3+}$ ,  $\text{Mn}^{4+}$ ) to fulfil charge neutrality, which gives rise to the co-existence of ferromagnetic double-exchange (DE) and antiferromagnetic super-exchange (SE) interactions [13]. Many creative techniques have been employed to synthesize LMO thin films such as sol–gel, pulsed laser deposition, molecular beam epitaxy (MBE), spray pyrolysis, etc [7, 14–17]. However, very few studies have focused on atomic layer deposited thin films of LMO [18]. Atomic layer deposition (ALD) is a well-established technique for depositing high-quality thin films for

<sup>6</sup> Authors to whom any correspondence should be addressed.

gate dielectrics and thin layers of other oxides used in solar cells and other electronic devices [19–21].

Our aim was to deposit thin films of LMO on silicon substrates using the ALD technique, and to investigate their structural, microstructural and magnetic properties. The oxygen-to-cation ratio and the resultant Mn valence states are crucial in these films, so the as-deposited films were annealed in nitrogen and oxygen atmospheres to see the effects of oxygen non-stoichiometry on physical properties. Bulk samples of LMO were also prepared by a citrate combustion route to allow a comparative study. The effects of various synthesis parameters and annealing conditions on sample properties are discussed in this paper.

## 2. Experimental

Thin films of LMO were grown in a commercial flow-type ALD reactor (F-120 by ASM Microchemistry Ltd) under a pressure of 2–3 mbar, following the experimental details described in an earlier study [18]. Freshly synthesized La(thd)<sub>3</sub> and Mn(thd)<sub>3</sub> (thd=2,2,6,6-tetramethylheptane-3,5-dionate) were used as precursors. The precursors were prepared by the method described in [22, 23], and then purified by a sublimation process. Ozone (O<sub>3</sub>), used as the oxidizer, was generated from oxygen (>99.999%) in an ozone generator (Fischer model 502). Nitrogen (>99.999%) was used as a carrier and purging gas. The pulsing period for the lanthanum and manganese precursors was 2 s, whereas the N<sub>2</sub> purging period was 2.5 s. Ozone was pulsed for 1.2 s followed by N<sub>2</sub> purging for 2.5 s. For the deposition of films, each ALD cycle had the following pulsing sequence: first La(thd)<sub>3</sub>, then O<sub>3</sub>, followed by Mn(thd)<sub>3</sub> and finally O<sub>3</sub> again. These films were deposited on single-crystal substrates of Si (1 0 0) at the deposition temperature 330 °C with different numbers of deposition cycles, and were labelled LM1300 (for 1300 deposition cycles), LM1000 (for 1000 deposition cycles) and LM900 (for 900 deposition cycles).

The as-deposited films were annealed in a rapid thermal annealing (RTA) furnace PEO 601 (ATV Technologie GmbH) in N<sub>2</sub> and/or O<sub>2</sub> atmosphere at temperatures ranging between 600 and 900 °C. The thicknesses of the LMO films were determined by x-ray reflectivity (XRR) using a Panalytical X'Pert Pro MPD Alpha-1 powder diffractometer with Cu K $\alpha$  radiation.

Polycrystalline bulk samples of LMO were synthesized by a chemical citrate solution method. La<sub>2</sub>O<sub>3</sub> and MnO<sub>2</sub> were used as starting materials, and their aqueous solutions (0.5M) with nitric acid and deionized (DI) water were prepared separately. Citric acid solution (0.5M) was also prepared using DI water. The oxides were taken in the targeted stoichiometric ratio, whereas the citric acid-to-cation ratio was 3 : 2. The pH of different solutions before mixing was around 2 (acidic). These solutions were mixed, and the pH of the resulting solution was made neutral or slightly alkaline (pH = 7–8) by adding ammonia solution. The amount of the mixed solution depends on the weight (stoichiometry) of precursors, being approximately 100–150 ml. The mixed solution was heated on a hot plate at around 80 °C with constant stirring, until

auto-combustion. The resulting fluffy powder was calcined at 600 °C for 2 h for LMO crystalline phase formation and to remove the organic impurities. The calcined powder was uniaxially pressed into disc-shaped pellets and sintered at 1300 °C for 3 h in air.

X-ray diffraction (XRD) was carried out using a Philips x-ray diffractometer for the bulk powder samples and Panalytical X'Pert Pro diffractometer with Cu K $\alpha$  radiation for the thin films. Raman spectroscopy (Horiba Jobin Yvon Labram HR 800) was performed at room temperature on these samples. The thin films' morphologies were evaluated by a scanning atomic force microscope (AFM, Veeco DIMENSION edge) in an area of 0.5 × 0.5  $\mu\text{m}^2$  with a resolution of 1024 lines. NanoScan PPMS-AFM was used for magnetic force microscopy (MFM). Vibrating sample magnetometer (VSM, Quantum Design's 14T-PPMS) was used to measure the magnetization and hysteresis loops of the powder samples and thin films. The temperature dependence of magnetization was measured in a broad temperature range (10–350 K) using zero field cooling (ZFC), and normalized to the total mass of the sample (including the mass of the substrate for films). Magnetic hysteresis loops from –6 to +6 kOe were measured at selected temperatures in the range 10–300 K.

## 3. Results and discussion

### 3.1. XRR–XRD studies

XRR results reveal that the thicknesses of our as-deposited LMO thin films with 1300 (LM1300), 1000 (LM1000) and 900 (LM900) deposition cycles were about 104 nm, 95 nm and 78 nm, respectively, with experimental errors around  $\pm 5\%$ . The thicknesses are correlated with the number of deposition cycles as expected, increasing with increasing number of deposition cycles such that growth per cycle (GPC) could be calculated to be roughly 0.9 Å/cycle. The small deviation from the perfectly linear dependence of the film thickness on the number of cycles is most probably due to minor changes in the reactor configuration.

The dependence of crystal structure on the annealing temperature is illustrated in figure 1(a) where XRD patterns for variously annealed LM1300 thin films are shown. These XRD patterns indicate that the as-deposited films and the films annealed at 600 °C are amorphous, films annealed at 700 and 800 °C have a single-phase perovskite structure, whereas the films annealed at 900 °C are not of single phase anymore. In further sections we will only discuss the results for single-phase crystalline films (i.e. thin films treated at 700 and 800 °C).

Figure 1(b) shows the XRD patterns for thin films LM1300, LM1000 and LM900 annealed at 700 and 800 °C in different atmospheres (N<sub>2</sub> and O<sub>2</sub>). It can be seen that all these films exhibit a single-phase perovskite-type lanthanum manganite structure [24]. The crystal structure is rhombohedral with space group *R*-3c. Even though determination of small variations in lattice parameters for thin-film samples is somewhat ambiguous we could see that the unit-cell volume for the LM1300 thin films increased (from 344.81 to 349.75 Å<sup>3</sup>) with annealing temperature increasing

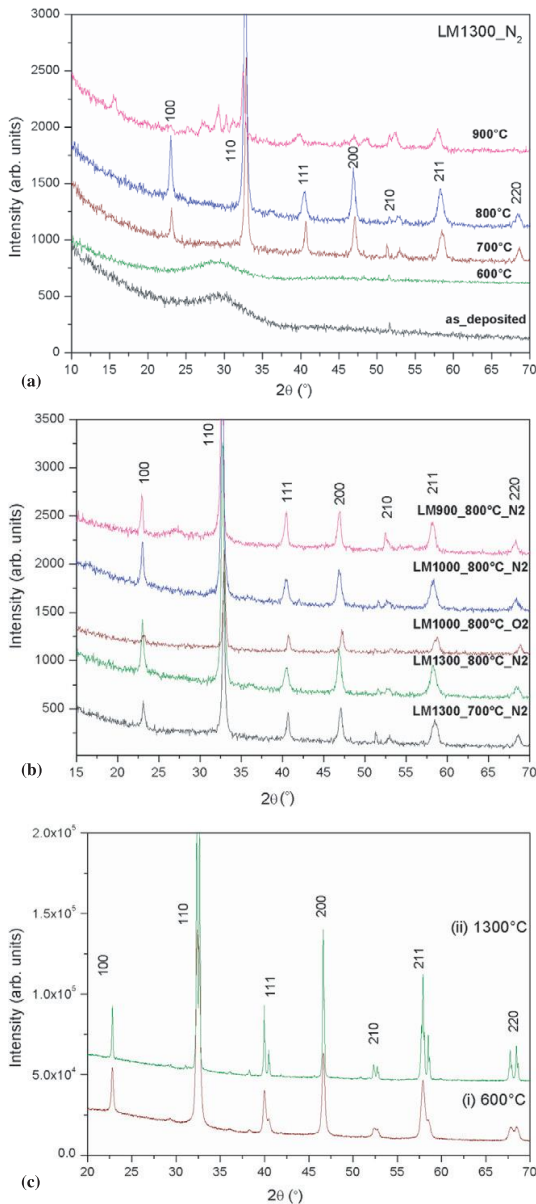


**Figure 1.** (a) XRD patterns of the LM1300 thin films (as-deposited and annealed at different temperatures in N<sub>2</sub> atmosphere). (b) XRD patterns of the LMO thin films (LM1300, LM1000 and LM900) annealed at different temperatures in N<sub>2</sub> and O<sub>2</sub> atmospheres. (c) XRD patterns of the LMO bulk powder samples annealed at 600 °C/2 h and 1300 °C/3 h in air.

from 700 to 800 °C in N<sub>2</sub>, apparently due to decreasing oxygen content (or oxygen-to-cation ratio). It was also seen that the unit-cell volume for the LM1000 thin films annealed at 800 °C depended on the annealing atmosphere (N<sub>2</sub> or O<sub>2</sub>), being larger in the case of N<sub>2</sub> (349.91 Å<sup>3</sup>) than in O<sub>2</sub> (342.69 Å<sup>3</sup>) as expected (listed in table 1).

**Table 1.** Unit cell volume, strain and crystallite sizes of the LMO thin films and bulk samples calculated from XRD.

Sample	Strain (%)	Average crystallite size (nm)	Unit-cell volume (Å <sup>3</sup> )
LM1300_700 °C_N <sub>2</sub>	0.394	27	344.81
LM1300_800 °C_N <sub>2</sub>	0.023	34	349.75
LM1000_800 °C_O <sub>2</sub>	0.150	25	342.69
LM1000_800 °C_N <sub>2</sub>	0.164	22	349.91
LM900_800 °C_N <sub>2</sub>	0.132	17	348.23
LaMnO <sub>3</sub> _Bulk_600 °C	0.237	40	354.64
LaMnO <sub>3</sub> _Bulk_1300 °C	0.044	1000	353.67

XRD patterns of the bulk LMO samples sintered at 600 and 1300 °C in air are shown in figure 1(c). These samples also exhibit the single-phase perovskite crystal structure with rhombohedral symmetry. The unit-cell volume (table 1) decreased with increase in annealing temperature (600 to 1300 °C), which could be the effect of change in oxygen content (decrease in oxygen deficiencies) at higher temperatures [25] and increase in non-stoichiometry. The XRD peaks become sharper and more intense with the increase in the annealing temperature, which indicates the increase in grain size and better crystallinity [26].

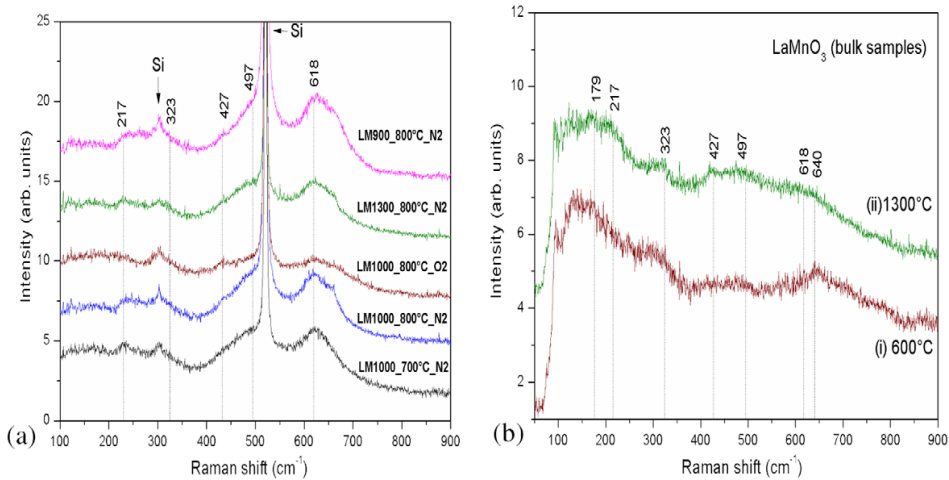
### 3.2. Raman studies

Figure 2(a) shows the Raman spectra of the LMO thin films (LM1300, LM1000 and LM900) annealed at 800 °C in N<sub>2</sub> and O<sub>2</sub> atmospheres. All spectra closely resemble those previously reported for rhombohedral LaMnO<sub>3</sub> at room temperature [27], showing peaks around 217, 323, 427, 497 and 618 cm<sup>-1</sup>, although the peaks around 323 and 497 cm<sup>-1</sup> are not very clear because of the strong signals from the silicon substrate around 300 and 520 cm<sup>-1</sup>. The exact positions of the peaks at 217, 497 and 618 cm<sup>-1</sup> are sample-sensitive and vary within 15–20 cm<sup>-1</sup> in the spectra of polycrystalline samples [28, 29]. The peaks around 500 and 600 cm<sup>-1</sup> are consistent with other studies, being usually ascribed to bending (B) and stretching (S) modes of the MnO<sub>6</sub> octahedron, respectively [14, 27]. The spectra of the LM1000 films annealed at 800 °C in N<sub>2</sub> and O<sub>2</sub> (see figure 2(a)) confirm their rhombohedral structure; however, the peaks are broader for the film annealed in O<sub>2</sub>, which also indicates the more stoichiometric oxygen-to-cation ratio in the case of the film annealed in N<sub>2</sub> atmosphere.

The Raman spectra of the bulk LMO samples sintered at 600 and 1300 °C are shown in figure 2(b). Although the peaks are broader due to rough surfaces of the bulk samples, they are observable around 179, 217, 323, 427, 497, 618 and 640 cm<sup>-1</sup>, also confirming the rhombohedral structure in these samples [25, 26].

### 3.3. AFM and MFM studies

AFM images in figures 3(a)–(f) show the uniform surface topography and microstructure of our annealed LMO thin films. Dense films are obtained by ALD as expected [30]. The samples annealed at 800 °C have larger grains (due to



**Figure 2.** Raman spectra measured at room temperature: (a) LM1300, LM1000 and LM900 thin films annealed at different temperatures in N<sub>2</sub> and O<sub>2</sub> atmospheres, (b) bulk LMO sample annealed at 600 and 1300 °C in air.

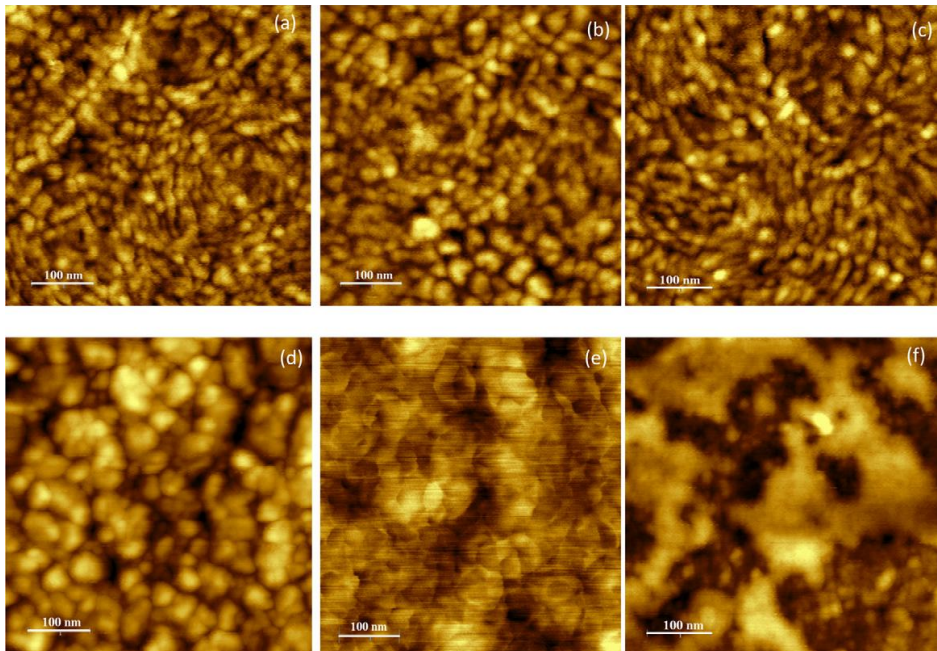


**Figure 3.** AFM images (scan area  $0.5 \times 0.5 \mu\text{m}^2$ ) measured under ambient conditions: (a) LM900 annealed at 800 °C in N<sub>2</sub>, (b) LM1000 annealed at 700 °C in N<sub>2</sub>, (c) LM1000 annealed at 800 °C in N<sub>2</sub>, (d) LM1000 annealed at 800 °C in O<sub>2</sub>, (e) LM1300 annealed at 700 °C in N<sub>2</sub> and (f) LM1300 annealed at 800 °C in N<sub>2</sub>.

coalescence of small grains) than those annealed at 700 °C by grain boundary diffusion, which usually causes major grain growth at high-temperature heat treatments. The grain sizes estimated from AFM images are given in table 2, which shows that the grain size increases also with increasing film thickness. The surface roughness of the films was calculated from the AFM results. The values listed in table 2 reveal that the films are extremely smooth in general. Results for the LM1300

and LM1000 films annealed at different temperatures (700 and 800 °C in N<sub>2</sub>) show that the root mean square (RMS) roughness value is slightly larger for the films annealed at 800 °C presumably due to growth of large grains [31–33, 36]. The results shown in table 2, moreover, suggest that the annealing atmosphere may also affect the surface morphology, as the LM1000 film annealed at 800 °C in N<sub>2</sub> atmosphere exhibits lower roughness and smaller grains compared with

**Table 2.** Grain sizes and RMS roughness values for the LMO films as determined by AFM.

Thin-film sample	RMS roughness (nm) (with scanned area of $7 \times 7 \mu\text{m}^2$ )	Grain size (nm) (approx. range)
LM900 annealed at 800 °C in N <sub>2</sub>	1.05	10–50
LM1000 annealed at 700 °C in N <sub>2</sub>	0.66	15–40
LM1000 annealed at 800 °C in N <sub>2</sub>	0.68	30–80
LM1000 annealed at 800 °C in O <sub>2</sub>	1.91	50–90
LM1300 annealed at 700 °C in N <sub>2</sub>	0.37	50–70
LM1300 annealed at 800 °C in N <sub>2</sub>	0.59	200–800

the same film after being annealed in O<sub>2</sub> atmosphere, which could be the result of the increase in oxygen non-stoichiometry in the film annealed in O<sub>2</sub>. Our AFM results and the effect of the annealing atmosphere on the microstructure are consistent with other studies [34, 35].

MFM images were taken at 65 K and zero magnetic fields for the LM1000 films annealed in N<sub>2</sub> and O<sub>2</sub> atmospheres. The images were taken at constant average height in dynamic mode. The contrast observed in the images of figure 4 corresponds to the detected shift of the centre frequency due to the interaction of the tip magnetic field with the stray field of the surface. Both images were taken at the same height and with the same cantilever amplitude, enabling a comparison to be made between the two films. Figure 4 shows the magnetic domain structure at 65 K to have a domain size of 50–100 nm for the film annealed in N<sub>2</sub> and 150–200 nm for the film annealed in O<sub>2</sub>. These domain sizes correspond well with the grain sizes of the films as measured by AFM (figures 3(c) and (d)), suggesting that the magnetic domains are pinned due to the topology of the surface.

### 3.4. Magnetic properties

To see the effects of film thickness on the magnetic properties, hysteresis curves and temperature dependence of magnetization were measured for the films. Figures 5(a)–(c) show the hysteresis curves at 100 K for the LM1300, LM1000 and LM900 thin films annealed at 800 °C in N<sub>2</sub>. The saturation magnetization does not show any noticeable change with thickness, whereas the coercivity changes to some extent with thickness presumably due to lattice disorder and strain present in the films. The hysteresis loops at room temperature (300 K) were almost diamagnetic (figures not included). However, below the transition temperature, the films show strong ferromagnetic behaviour, which is clear from figure 5.

The temperature dependence of magnetization (ZFC at 0.1 T or 1000 Oe) is shown in figures 5(d)–(f) for the films LM1300, LM1000 and LM900 annealed at 800 °C in N<sub>2</sub>. LM1300 exhibits broad anomalies at 44 and 211 K (figure 5(d)); this is consistent with the results of another study [36]. These anomalies for LM1000 and LM900 were found to be around 46 K and 196 K, and 45 K and 200 K, respectively. The small shift in transition temperatures for different films of varying thicknesses might be the result of the presence of lattice

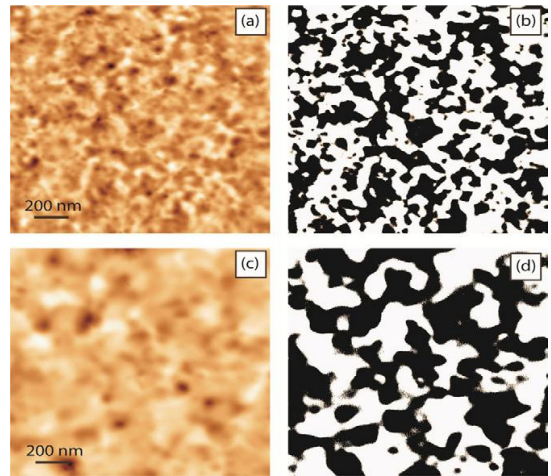


**Figure 4.** MFM images taken at constant average height ( $T = 65$  K,  $H = 0$ ) of the LM1000 film annealed at 800 °C: (a) N<sub>2</sub> atmosphere, (b) domain pattern derived from (a), domain size 50–100 nm; (c) O<sub>2</sub> atmosphere, (d) domain pattern derived from (c), domain size 150–200 nm.

disorder and/or strain in the films. The lower temperature anomaly at around 45 K in the magnetization curves might be associated with rearrangements of ferromagnetic domains, whereas the higher temperature anomaly is likely associated with the paramagnetic–ferromagnetic phase transition ( $T_C$ ), usually occurring at 140 K in high-quality single crystals and ceramics [6]. The noticeable increase in the Curie temperature in our thin films ( $T_C$  around 200 K) may be due to the non-stoichiometry (increased oxygen-to-cation ratio).

Figures 6(a) and (b) show the magnetization and hysteresis curves of the LM1000 thin films annealed at 800 °C in N<sub>2</sub> and O<sub>2</sub> atmospheres. The film annealed in O<sub>2</sub> atmosphere has  $T_C$  around 250 K, whereas the one annealed in N<sub>2</sub> has a clearly lower  $T_C$  of around 200 K (figure 6(a)). The high  $T_C$  value for our O<sub>2</sub>-annealed LM1000 thin film is consistent with the enhanced  $T_C$  observed in another study on LMO thin films grown in pure oxygen atmosphere by pulsed laser deposition [7]. The larger saturation magnetization suggests the enhanced ferromagnetism for the O<sub>2</sub>-annealed film as compared with that annealed in N<sub>2</sub> atmosphere; however, the coercivity is lower (figure 6(b)) for this film due to the larger grains (see the AFM image in figure 3). Our XRD and magnetic property characterization results are in good agreement with other studies on LMO thin films [7, 37], and we hence conclude that upon O<sub>2</sub> annealing the concentration of the smaller Mn<sup>4+</sup> ions increases on the expense of the larger Mn<sup>3+</sup> ions which enhances the exchange coupling between Mn<sup>3+</sup> and Mn<sup>4+</sup> ions, resulting in improved ferromagnetism and the higher  $T_C$  value [38].

Annealing in O<sub>2</sub> atmosphere induces cation vacancies in LMO, which results in an up-shift of the magnetic transition temperatures and enhanced ferromagnetic character arising from the canting of the antiferromagnetic arrangement of spins [39, 40]. The magnetization curves of the LM1300

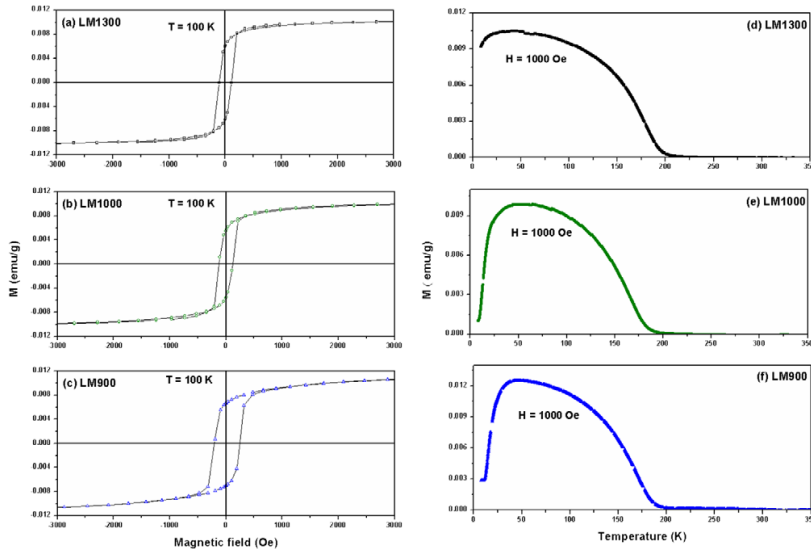


**Figure 5.** (a)–(c) Hysteresis ( $T = 100$  K) and (d)–(f) magnetization curves (ZFC) of the LM1300, LM1000 and LM900 thin films annealed at  $800^\circ\text{C}$  in  $\text{N}_2$  atmosphere.

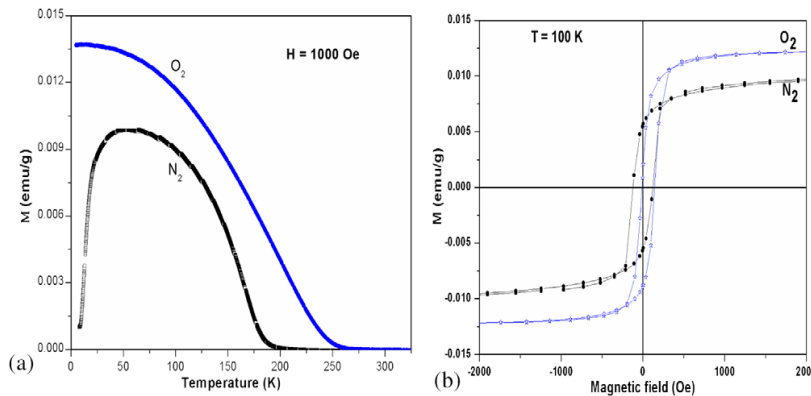
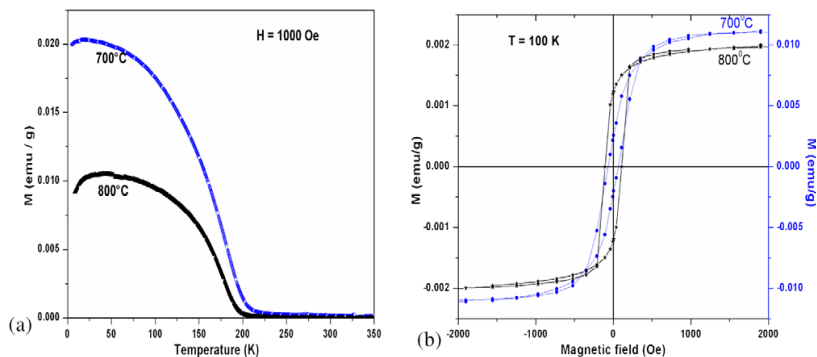


**Figure 6.** (a) Magnetization and (b) hysteresis ( $T = 100$  K) curves of the LM1000 thin films annealed at  $800^\circ\text{C}$  in  $\text{N}_2$  and  $\text{O}_2$  atmospheres.

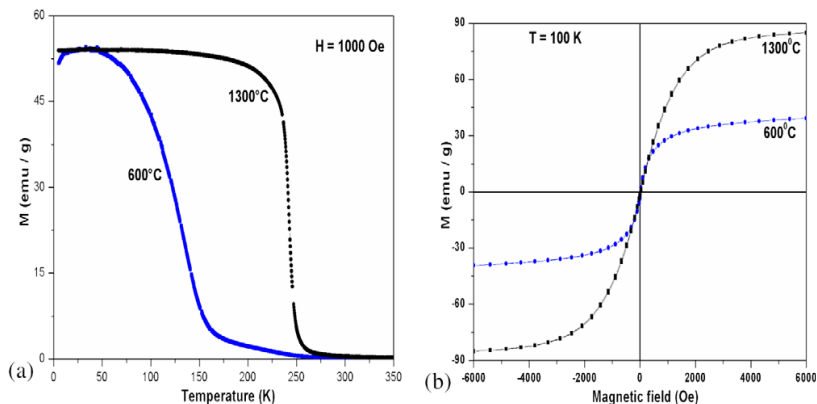
thin films annealed in  $\text{N}_2$  atmosphere at  $700$  and  $800^\circ\text{C}$  are shown in figure 7(a), revealing a decrease in  $T_C$  from  $210$  to  $195$  K with an increase in the annealing temperature from  $700$  to  $800^\circ\text{C}$ , apparently due to an increase in the cation-to-oxygen ratio and a reduction in ferromagnetism. A decrease in the  $\text{Mn}^{4+}$  content at higher temperatures may also be the reason for the depression of ferromagnetism and thus the lowering of  $T_C$ . Figure 7(b) shows the hysteresis curve of the LM1300 thin films (annealed at  $700$  and  $800^\circ\text{C}$  in  $\text{N}_2$ ) measured at  $100$  K. There is an increase in the coercivity for the sample annealed at  $800^\circ\text{C}$ , which can be related to the enhanced antiferromagnetism (at the measurement temperature of  $100$  K) for this film.

Figure 8(a) shows the temperature dependence of magnetization of the bulk LMO samples sintered at  $600$  and  $1300^\circ\text{C}$  in air. Here  $T_C$  is increased (from  $220$  to  $250$  K) with increasing annealing temperature from  $600$  to  $1300^\circ\text{C}$  in air

indicating that the higher temperature annealing in air results in an increased oxygen content (or higher  $\text{Mn}^{4+}$ -ion content) and formation of cation vacancies, which enhances the  $T_C$  [6, 41]. Hysteresis loops measured at  $100$  K for the two bulk samples are shown in figure 8(b) revealing remarkably high values of saturation magnetization. Sankar and Joy [37] obtained similar values of magnetization in self-doped LMO prepared by the solid-state reaction method, through which the samples trap more La vacancies. Since Mn is smaller than La, Mn species can be incorporated into vacant La sites and consequently the valence state of Mn changes ( $\text{Mn}^{3+} \rightarrow \text{Mn}^{4+}$ ), the total concentration of  $\text{Mn}^{4+}$  ions increases and  $\text{Mn}^{3+}-\text{O}-\text{Mn}^{4+}$  interactions are enhanced [42] resulting in better ferromagnetic properties. It is clear from figure 8(b) that the LMO bulk sample sintered at the lower temperature ( $600^\circ\text{C}$ ) exhibits lower saturation magnetization and coercivity compared with the sample sintered at the higher temperature ( $1300^\circ\text{C}$ ). We



**Figure 7.** (a) Magnetization and (b) hysteresis curves ( $T = 100$  K) of the LM1300 thin film annealed at 700 and 800 °C in  $N_2$ .



**Figure 8.** (a) Magnetization and (b) hysteresis curves ( $T = 100$  K) of the LMO bulk samples annealed at 600 and 1300 °C in air.

suggest that in the present case also sintering at 1300 °C in air induces La vacancies, which then results in higher  $Mn^{4+}$ -ion concentration and enhanced ferromagnetic properties.

It is important to emphasize that the annealing atmosphere affects the magnetic properties significantly. Annealing in  $N_2$  atmosphere at higher temperatures leads to more stoichiometric samples and causes reduction in ferromagnetism, whereas the high-temperature treatment in air/ $O_2$  atmosphere leads to non-stoichiometry and enhancement in ferromagnetism in  $LaMnO_3$  bulk and thin-film samples. The structural and microstructural properties of LMO thin films deposited by the ALD method are found to be good and can be improved by changing the substrates and deposition temperatures. Following this study, future work may be the continuation of deposition and study of quaternary thin films such as LSMO and LCMO, which are quite complex to deposit as a single phase by the ALD method.

#### 4. Conclusions

We have synthesized high-quality perovskite-structured LMO thin films on silicon substrates by the ALD technique and also bulk LMO samples by a citrate combustion method. All thin films annealed at 700–800 °C and bulk samples (synthesized at

600 and 1300 °C) exhibited the single-phase perovskite-type lanthanum manganite structure, as confirmed from both XRD and Raman spectroscopy data. Variations in film thickness, annealing atmosphere ( $N_2$  or  $O_2$ ) and temperature did not affect the crystal structure but changed the microstructure, surface morphology, oxygen-to-cation ratio and magnetic transition temperatures in our LMO thin films. The oxygen non-stoichiometry (i.e. cation vacancies) and thereby the  $Mn^{4+}/Mn^{3+}$  ratio tuned by the processing parameters caused the variation in magnetic properties of our ALD-grown LMO thin films as well as the bulk samples. Annealing in  $N_2$  atmosphere enhanced the antiferromagnetism and better stoichiometry, whereas the air/ $O_2$  annealing enhanced the ferromagnetism and non-stoichiometry in the LMO samples. The Curie transition temperatures in our LMO film and bulk samples were found to be higher from the ideal value ( $\sim 140$  K), which also could be related to non-stoichiometry.

#### Acknowledgments

This work was financially supported by the Estonian Research Council (ETF 8440, MJD 65, TK114, SF0690029s09 and SF0690034s09) and also by the Academy of Finland (No 255562). HK thanks the DORA program for her doctoral

fellowship. SL and RL were supported by ETF 9007, the Estonian Nanotechnology Competence Centre (EU29996), and various ERDF grants.

## References

- [1] Tokura Y, Tomioka Y, Kuwahara H, Asamitsu A, Morimoto Y and Kasai M 1996 *J. Appl. Phys.* **79** 5288
- [2] Mills A J 1998 *Nature* **392** 147
- [3] De K, Ray R, Panda R N, Giri S, Nakamura H and Kohara T 2005 *J. Magn. Magn. Mater.* **288** 339
- [4] Nakayama S, Okasaki M, Aung Y L and Sakamoto M 2003 *Solid State Ion.* **158** 133
- [5] Siwach P K, Singh H K and Srivastava O N 2008 *J. Phys.: Condens. Matter* **20** 273201
- [6] Ritter C, Ibarra M R, De Teresa J M, Algarabel P A, Marquina C, Blasco J, García J, Oseroff S and Cheong S-W 1997 *Phys. Rev. B* **56** 8902
- [7] Kim H S and Christen H M 2010 *J. Phys.: Condens. Matter* **22** 146007
- [8] Salamon M B and Jaime M 2001 *Rev. Mod. Phys.* **73** 583
- [9] Topfer J and Goodenough J B 1997 *J. Solid State Chem.* **130** 117
- [10] Murugavel P, Lee J H, Yoon J-G and Noh T W 2003 *Appl. Phys. Lett.* **82** 1908
- [11] Choi W S *et al* 2009 *J. Phys. D: Appl. Phys.* **42** 165401
- [12] Gupta A, McGuiere T R, Duncombe P R, Rupp M, Sun J Z, Gallagher W J and Xiao G 1995 *Appl. Phys. Lett.* **67** 3494
- [13] Kleine A, Luo Y and Samwer K 2006 *Europhys. Lett.* **76** 135
- [14] Aruta C *et al* 2006 *J. Appl. Phys.* **100** 023910
- [15] Kartopu G and Es-Souni M 2006 *J. Appl. Phys.* **99** 033501
- [16] Orgaini P, Aruta C, Ciancio R, Galdi A and Maritato L 2009 *Appl. Phys. Lett.* **95** 013510
- [17] Todorovska R, Petrova N, Todorovsky D and Groudeva-Zotova S 2006 *Appl. Surf. Sci.* **252** 3441
- [18] Uusi-Esko K and Karppinen M 2011 *Chem. Mater.* **23** 1835
- [19] Ritala M, Leskelä M and Nalwa H S (ed) 2001 *Handbook of Thin Film Materials* vol 1 (San Diego, CA: Academic) p 103 chapter 2
- [20] Pore V 2010 Atomic layer deposition and photocatalytic properties of titanium dioxide thin films *PhD Thesis* ([www.doria.fi/bitstream/handle/10024/62220/atomicla.pdf](http://www.doria.fi/bitstream/handle/10024/62220/atomicla.pdf))
- [21] Putkonen M, Niinistö J, Kukli K, Sajavaara T, Karppinen M, Yamauchi H and Niinistö L 2003 *Chem. Vapor Depos.* **9** 207
- [22] Eisentraut K J and Sievers R E 1956 *J. Am. Chem. Soc.* **87** 5254
- [23] Hammond G S, Nonhebel D C and Wu C H S 1963 *Inorg. Chem.* **2** 73
- [24] Shimizu Y and Murata T 1997 *J. Am. Ceram. Soc.* **80** 2702
- [25] Ni H, Yu D, Zhao K, Kong Y C, Wong H K, Zhao S Q and Zhang W S 2011 *J. Appl. Phys.* **110** 033112
- [26] Wang X L, Li D, Shi C X, Li B, T.Y.Cui T Y and Zhang Z D 2010 *Physica B* **405** 1362
- [27] Iliiev M N and Abrashev M V 2001 *J. Raman Spectrosc.* **32** 805
- [28] Abrashev M V *et al* 1999 *Phys. Rev. B* **59** 4146
- [29] Zhizhin G N, Mavrin B N and Shabanov V F 1984 *Optical Vibrational Spectra of Crystals* (Moscow: Nauka) p 212
- [30] Choi W S 2009 *Trans. Electr. Electron. Mater.* **10** 200
- [31] Youssef S, Combette P, Podlecki J, Asmar R A and Foucaran A 2009 *Cryst. Growth Des.* **9** 1088
- [32] Sengupta J, Sahoo R K, Bardhan K K and Mukherjee C D 2011 *Mater. Lett.* **65** 2572
- [33] Liu Y C, Tung S K and Hsieh J H 2006 *J. Cryst. Growth* **287** 105
- [34] Simoes A Z, Riccardi C S, Dos Santos M L, Gonzalez Garcia F, Longo E and Varela J A 2009 *Mater. Res. Bull.* **44** 1747
- [35] Tsang C F and Woo J 2000 *Mater. Charact.* **45** 187
- [36] Romaguera-Barcelay Y, Agostinho Moreira J, Gonzalez-Aguilar G, Almeida A, Araujo J P and Perez de la Cruz J 2011 *J. Electroceram.* **26** 44
- [37] Raj Sankar C and Joy P A 2005 *Phys. Rev. B* **72** 02440
- [38] Coey J M D, Viret M and von Molnar S 1999 *Adv. Phys.* **48** 167
- [39] Krishnamoorthy C, Sethupathi C K, Sankaranarayanan V, Nirmala R and Malik S K 2007 *J. Alloys Compounds* **438** 1
- [40] Raychaudhuri P and Mitra C 2003 *J. Appl. Phys.* **93** 8328
- [41] Joy P A, Raj Sankar C and Date S K 2002 *J. Phys.: Condens. Matter* **14** 4985
- [42] Brankovic Z, Duris K, Radojkovic A, Bernik S, Jaglicic Z, Jagodic M, Vojisavljevic K and Brankovic G 2010 *J. Sol-Gel Sci. Technol.* **55** 311

**DISSERTATIONS DEFENDED AT  
TALLINN UNIVERSITY OF TECHNOLOGY ON  
NATURAL AND EXACT SCIENCES**

1. **Olav Kongas**. Nonlinear Dynamics in Modeling Cardiac Arrhythmias. 1998.
2. **Kalju Vanatalu**. Optimization of Processes of Microbial Biosynthesis of Isotopically Labeled Biomolecules and Their Complexes. 1999.
3. **Ahto Buldas**. An Algebraic Approach to the Structure of Graphs. 1999.
4. **Monika Drews**. A Metabolic Study of Insect Cells in Batch and Continuous Culture: Application of Chemostat and Turbidostat to the Production of Recombinant Proteins. 1999.
5. **Eola Valdre**. Endothelial-Specific Regulation of Vessel Formation: Role of Receptor Tyrosine Kinases. 2000.
6. **Kalju Lott**. Doping and Defect Thermodynamic Equilibrium in ZnS. 2000.
7. **Reet Koljak**. Novel Fatty Acid Dioxygenases from the Corals *Plexaura homomalla* and *Gersemia fruticosa*. 2001.
8. **Anne Paju**. Asymmetric oxidation of Prochiral and Racemic Ketones by Using Sharpless Catalyst. 2001.
9. **Marko Vendelin**. Cardiac Mechanoenergetics *in silico*. 2001.
10. **Pearu Peterson**. Multi-Soliton Interactions and the Inverse Problem of Wave Crest. 2001.
11. **Anne Menert**. Microcalorimetry of Anaerobic Digestion. 2001.
12. **Toomas Tiivel**. The Role of the Mitochondrial Outer Membrane in *in vivo* Regulation of Respiration in Normal Heart and Skeletal Muscle Cell. 2002.
13. **Olle Hints**. Ordovician Scolecodonts of Estonia and Neighbouring Areas: Taxonomy, Distribution, Palaeoecology, and Application. 2002.
14. **Jaak Nõlvak**. Chitinozoan Biostratigraphy in the Ordovician of Baltoscandia. 2002.
15. **Liivi Kluge**. On Algebraic Structure of Pre-Operad. 2002.
16. **Jaanus Lass**. Biosignal Interpretation: Study of Cardiac Arrhythmias and Electromagnetic Field Effects on Human Nervous System. 2002.
17. **Janek Peterson**. Synthesis, Structural Characterization and Modification of PAMAM Dendrimers. 2002.
18. **Merike Vaher**. Room Temperature Ionic Liquids as Background Electrolyte Additives in Capillary Electrophoresis. 2002.
19. **Valdek Mikli**. Electron Microscopy and Image Analysis Study of Powdered Hardmetal Materials and Optoelectronic Thin Films. 2003.
20. **Mart Viljus**. The Microstructure and Properties of Fine-Grained Cermets. 2003.
21. **Signe Kask**. Identification and Characterization of Dairy-Related *Lactobacillus*. 2003.
22. **Tiiu-Mai Laht**. Influence of Microstructure of the Curd on Enzymatic and Microbiological Processes in Swiss-Type Cheese. 2003.
23. **Anne Kuusksalu**. 2–5A Synthetase in the Marine Sponge *Geodia cydonium*. 2003.
24. **Sergei Bereznev**. Solar Cells Based on Polycrystalline Copper-Indium Chalcogenides and Conductive Polymers. 2003.

25. **Kadri Kriis.** Asymmetric Synthesis of C<sub>2</sub>-Symmetric Bimorpholines and Their Application as Chiral Ligands in the Transfer Hydrogenation of Aromatic Ketones. 2004.
26. **Jekaterina Reut.** Polypyrrole Coatings on Conducting and Insulating Substrates. 2004.
27. **Sven Nõmm.** Realization and Identification of Discrete-Time Nonlinear Systems. 2004.
28. **Olga Kijatkina.** Deposition of Copper Indium Disulphide Films by Chemical Spray Pyrolysis. 2004.
29. **Gert Tamberg.** On Sampling Operators Defined by Rogosinski, Hann and Blackman Windows. 2004.
30. **Monika Übner.** Interaction of Humic Substances with Metal Cations. 2004.
31. **Kaarel Adamberg.** Growth Characteristics of Non-Starter Lactic Acid Bacteria from Cheese. 2004.
32. **Imre Vallikivi.** Lipase-Catalysed Reactions of Prostaglandins. 2004.
33. **Merike Peld.** Substituted Apatites as Sorbents for Heavy Metals. 2005.
34. **Vitali Syritski.** Study of Synthesis and Redox Switching of Polypyrrole and Poly(3,4-ethylenedioxythiophene) by Using *in-situ* Techniques. 2004.
35. **Lee Põllumaa.** Evaluation of Ecotoxicological Effects Related to Oil Shale Industry. 2004.
36. **Riina Aav.** Synthesis of 9,11-Secosterols Intermediates. 2005.
37. **Andres Braunbrück.** Wave Interaction in Weakly Inhomogeneous Materials. 2005.
38. **Robert Kitt.** Generalised Scale-Invariance in Financial Time Series. 2005.
39. **Juss Pavelson.** Mesoscale Physical Processes and the Related Impact on the Summer Nutrient Fields and Phytoplankton Blooms in the Western Gulf of Finland. 2005.
40. **Olari Ilison.** Solitons and Solitary Waves in Media with Higher Order Dispersive and Nonlinear Effects. 2005.
41. **Maksim Säkki.** Intermittency and Long-Range Structurization of Heart Rate. 2005.
42. **Enli Kiipli.** Modelling Seawater Chemistry of the East Baltic Basin in the Late Ordovician–Early Silurian. 2005.
43. **Igor Golovtsov.** Modification of Conductive Properties and Processability of Polyparaphenylene, Polypyrrole and polyaniline. 2005.
44. **Katrin Laos.** Interaction Between Furcellaran and the Globular Proteins (Bovine Serum Albumin  $\beta$ -Lactoglobulin). 2005.
45. **Arvo Mere.** Structural and Electrical Properties of Spray Deposited Copper Indium Disulphide Films for Solar Cells. 2006.
46. **Sille Ehala.** Development and Application of Various On- and Off-Line Analytical Methods for the Analysis of Bioactive Compounds. 2006.
47. **Maria Kulp.** Capillary Electrophoretic Monitoring of Biochemical Reaction Kinetics. 2006.
48. **Anu Aaspõllu.** Proteinases from *Vipera lebetina* Snake Venom Affecting Hemostasis. 2006.
49. **Lyudmila Chekulayeva.** Photosensitized Inactivation of Tumor Cells by Porphyrins and Chlorins. 2006.

50. **Merle Uudsemaa.** Quantum-Chemical Modeling of Solvated First Row Transition Metal Ions. 2006.
51. **Tagli Pitsi.** Nutrition Situation of Pre-School Children in Estonia from 1995 to 2004. 2006.
52. **Angela Ivask.** Luminescent Recombinant Sensor Bacteria for the Analysis of Bioavailable Heavy Metals. 2006.
53. **Tiina Lõugas.** Study on Physico-Chemical Properties and Some Bioactive Compounds of Sea Buckthorn (*Hippophae rhamnoides* L.). 2006.
54. **Kaja Kasemets.** Effect of Changing Environmental Conditions on the Fermentative Growth of *Saccharomyces cerevisiae* S288C: Auxo-accelerostat Study. 2006.
55. **Ildar Nisamedtinov.** Application of <sup>13</sup>C and Fluorescence Labeling in Metabolic Studies of *Saccharomyces* spp. 2006.
56. **Alar Leibak.** On Additive Generalisation of Voronoi's Theory of Perfect Forms over Algebraic Number Fields. 2006.
57. **Andri Jagomägi.** Photoluminescence of Chalcopyrite Tellurides. 2006.
58. **Tõnu Martma.** Application of Carbon Isotopes to the Study of the Ordovician and Silurian of the Baltic. 2006.
59. **Marit Kauk.** Chemical Composition of CuInSe<sub>2</sub> Monograin Powders for Solar Cell Application. 2006.
60. **Julia Kois.** Electrochemical Deposition of CuInSe<sub>2</sub> Thin Films for Photovoltaic Applications. 2006.
61. **Iлона Oja Açıık.** Sol-Gel Deposition of Titanium Dioxide Films. 2007.
62. **Tiia Anmann.** Integrated and Organized Cellular Bioenergetic Systems in Heart and Brain. 2007.
63. **Katrin Trummal.** Purification, Characterization and Specificity Studies of Metalloproteinases from *Vipera lebetina* Snake Venom. 2007.
64. **Gennadi Lessin.** Biochemical Definition of Coastal Zone Using Numerical Modeling and Measurement Data. 2007.
65. **Enno Pais.** Inverse problems to determine non-homogeneous degenerate memory kernels in heat flow. 2007.
66. **Maria Borissova.** Capillary Electrophoresis on Alkylimidazolium Salts. 2007.
67. **Karin Valmsen.** Prostaglandin Synthesis in the Coral *Plexaura homomalla*: Control of Prostaglandin Stereochemistry at Carbon 15 by Cyclooxygenases. 2007.
68. **Kristjan Piirimäe.** Long-Term Changes of Nutrient Fluxes in the Drainage Basin of the Gulf of Finland – Application of the PolFlow Model. 2007.
69. **Tatjana Dedova.** Chemical Spray Pyrolysis Deposition of Zinc Sulfide Thin Films and Zinc Oxide Nanostructured Layers. 2007.
70. **Katrin Tomson.** Production of Labelled Recombinant Proteins in Fed-Batch Systems in *Escherichia coli*. 2007.
71. **Cecilia Sarmiento.** Suppressors of RNA Silencing in Plants. 2008.
72. **Vilja Mardla.** Inhibition of Platelet Aggregation with Combination of Antiplatelet Agents. 2008.
73. **Maie Bachmann.** Effect of Modulated Microwave Radiation on Human Resting Electroencephalographic Signal. 2008.
74. **Dan Hüvonen.** Terahertz Spectroscopy of Low-Dimensional Spin Systems. 2008.

75. **Ly Villo.** Stereoselective Chemoenzymatic Synthesis of Deoxy Sugar Esters Involving *Candida antarctica* Lipase B. 2008.
76. **Johan Anton.** Technology of Integrated Photoelasticity for Residual Stress Measurement in Glass Articles of Axisymmetric Shape. 2008.
77. **Olga Volobujeva.** SEM Study of Selenization of Different Thin Metallic Films. 2008.
78. **Artur Jõgi.** Synthesis of 4'-Substituted 2,3'-dideoxynucleoside Analogues. 2008.
79. **Mario Kadastik.** Doubly Charged Higgs Boson Decays and Implications on Neutrino Physics. 2008.
80. **Fernando Pérez-Caballero.** Carbon Aerogels from 5-Methylresorcinol-Formaldehyde Gels. 2008.
81. **Sirje Vaask.** The Comparability, Reproducibility and Validity of Estonian Food Consumption Surveys. 2008.
82. **Anna Menaker.** Electrosynthesized Conducting Polymers, Polypyrrole and Poly(3,4-ethylenedioxythiophene), for Molecular Imprinting. 2009.
83. **Lauri Ilison.** Solitons and Solitary Waves in Hierarchical Korteweg-de Vries Type Systems. 2009.
84. **Kaia Ernits.** Study of In<sub>2</sub>S<sub>3</sub> and ZnS Thin Films Deposited by Ultrasonic Spray Pyrolysis and Chemical Deposition. 2009.
85. **Veljo Sinivee.** Portable Spectrometer for Ionizing Radiation "Gammamapper". 2009.
86. **Jüri Virkepu.** On Lagrange Formalism for Lie Theory and Operadic Harmonic Oscillator in Low Dimensions. 2009.
87. **Marko Piirsoo.** Deciphering Molecular Basis of Schwann Cell Development. 2009.
88. **Kati Helmja.** Determination of Phenolic Compounds and Their Antioxidative Capability in Plant Extracts. 2010.
89. **Merike Sõmera.** Sobemoviruses: Genomic Organization, Potential for Recombination and Necessity of P1 in Systemic Infection. 2010.
90. **Kristjan Laes.** Preparation and Impedance Spectroscopy of Hybrid Structures Based on CuIn<sub>3</sub>Se<sub>5</sub> Photoabsorber. 2010.
91. **Kristin Lippur.** Asymmetric Synthesis of 2,2'-Bimorpholine and its 5,5'-Substituted Derivatives. 2010.
92. **Merike Luman.** Dialysis Dose and Nutrition Assessment by an Optical Method. 2010.
93. **Mihhail Berezovski.** Numerical Simulation of Wave Propagation in Heterogeneous and Microstructured Materials. 2010.
94. **Tamara Aid-Pavlidis.** Structure and Regulation of BDNF Gene. 2010.
95. **Olga Bragina.** The Role of Sonic Hedgehog Pathway in Neuro- and Tumorigenesis. 2010.
96. **Merle Randrüüt.** Wave Propagation in Microstructured Solids: Solitary and Periodic Waves. 2010.
97. **Marju Laars.** Asymmetric Organocatalytic Michael and Aldol Reactions Mediated by Cyclic Amines. 2010.
98. **Maarja Grossberg.** Optical Properties of Multinary Semiconductor Compounds for Photovoltaic Applications. 2010.

99. **Alla Maloverjan.** Vertebrate Homologues of Drosophila Fused Kinase and Their Role in Sonic Hedgehog Signalling Pathway. 2010.
100. **Priit Pruunsild.** Neuronal Activity-Dependent Transcription Factors and Regulation of Human *BDNF* Gene. 2010.
101. **Tatjana Knjazeva.** New Approaches in Capillary Electrophoresis for Separation and Study of Proteins. 2011.
102. **Atanas Katerski.** Chemical Composition of Sprayed Copper Indium Disulfide Films for Nanostructured Solar Cells. 2011.
103. **Kristi Timmo.** Formation of Properties of  $\text{CuInSe}_2$  and  $\text{Cu}_2\text{ZnSn}(\text{S,Se})_4$  Monograin Powders Synthesized in Molten KI. 2011.
104. **Kert Tamm.** Wave Propagation and Interaction in Mindlin-Type Microstructured Solids: Numerical Simulation. 2011.
105. **Adrian Popp.** Ordovician Proetid Trilobites in Baltoscandia and Germany. 2011.
106. **Ove Pärn.** Sea Ice Deformation Events in the Gulf of Finland and This Impact on Shipping. 2011.
107. **Germo Väli.** Numerical Experiments on Matter Transport in the Baltic Sea. 2011.
108. **Andrus Seiman.** Point-of-Care Analyser Based on Capillary Electrophoresis. 2011.
109. **Olga Katargina.** Tick-Borne Pathogens Circulating in Estonia (Tick-Borne Encephalitis Virus, *Anaplasma phagocytophilum*, *Babesia* Species): Their Prevalence and Genetic Characterization. 2011.
110. **Ingrid Sumeri.** The Study of Probiotic Bacteria in Human Gastrointestinal Tract Simulator. 2011.
111. **Kairit Zovo.** Functional Characterization of Cellular Copper Proteome. 2011.
112. **Natalja Makarytsheva.** Analysis of Organic Species in Sediments and Soil by High Performance Separation Methods. 2011.
113. **Monika Mortimer.** Evaluation of the Biological Effects of Engineered Nanoparticles on Unicellular Pro- and Eukaryotic Organisms. 2011.
114. **Kersti Tepp.** Molecular System Bioenergetics of Cardiac Cells: Quantitative Analysis of Structure-Function Relationship. 2011.
115. **Anna-Liisa Peikolainen.** Organic Aerogels Based on 5-Methylresorcinol. 2011.
116. **Leeli Amon.** Palaeoecological Reconstruction of Late-Glacial Vegetation Dynamics in Eastern Baltic Area: A View Based on Plant Macrofossil Analysis. 2011.
117. **Tanel Peets.** Dispersion Analysis of Wave Motion in Microstructured Solids. 2011.
118. **Liina Kaupmees.** Selenization of Molybdenum as Contact Material in Solar Cells. 2011.
119. **Allan Olsper.** Properties of VPg and Coat Protein of Sobemoviruses. 2011.
120. **Kadri Koppel.** Food Category Appraisal Using Sensory Methods. 2011.
121. **Jelena Gorbatšova.** Development of Methods for CE Analysis of Plant Phenolics and Vitamins. 2011.
122. **Karin Viipsi.** Impact of EDTA and Humic Substances on the Removal of Cd and Zn from Aqueous Solutions by Apatite. 2012.

123. **David Schryer**. Metabolic Flux Analysis of Compartmentalized Systems Using Dynamic Isotopologue Modeling. 2012.
124. **Ardo Illaste**. Analysis of Molecular Movements in Cardiac Myocytes. 2012.
125. **Indrek Reile**. 3-Alkylcyclopentane-1,2-Diones in Asymmetric Oxidation and Alkylation Reactions. 2012.
126. **Tatjana Tamberg**. Some Classes of Finite 2-Groups and Their Endomorphism Semigroups. 2012.
127. **Taavi Liblik**. Variability of Thermohaline Structure in the Gulf of Finland in Summer. 2012.
128. **Priidik Lagemaa**. Operational Forecasting in Estonian Marine Waters. 2012.
129. **Andrei Errapart**. Photoelastic Tomography in Linear and Non-linear Approximation. 2012.
130. **Külliki Krabbi**. Biochemical Diagnosis of Classical Galactosemia and Mucopolysaccharidoses in Estonia. 2012.
131. **Kristel Kaseleht**. Identification of Aroma Compounds in Food using SPME-GC/MS and GC-Olfactometry. 2012.
132. **Kristel Kodar**. Immunoglobulin G Glycosylation Profiling in Patients with Gastric Cancer. 2012.
133. **Kai Rosin**. Solar Radiation and Wind as Agents of the Formation of the Radiation Regime in Water Bodies. 2012.
134. **Ann Tiiman**. Interactions of Alzheimer's Amyloid-Beta Peptides with Zn(II) and Cu(II) Ions. 2012.
135. **Olga Gavrilova**. Application and Elaboration of Accounting Approaches for Sustainable Development. 2012.
136. **Olesja Bondarenko**. Development of Bacterial Biosensors and Human Stem Cell-Based *In Vitro* Assays for the Toxicological Profiling of Synthetic Nanoparticles. 2012.
137. **Katri Muska**. Study of Composition and Thermal Treatments of Quaternary Compounds for Monocrystalline Layer Solar Cells. 2012.
138. **Ranno Nahku**. Validation of Critical Factors for the Quantitative Characterization of Bacterial Physiology in Accelerostat Cultures. 2012.
139. **Petri-Jaan Lahtvee**. Quantitative Omics-level Analysis of Growth Rate Dependent Energy Metabolism in *Lactococcus lactis*. 2012.
140. **Kerti Orumets**. Molecular Mechanisms Controlling Intracellular Glutathione Levels in Baker's Yeast *Saccharomyces cerevisiae* and its Random Mutagenized Glutathione Over-Accumulating Isolate. 2012.
141. **Loreida Timberg**. Spice-Cured Sprats Ripening, Sensory Parameters Development, and Quality Indicators. 2012.
142. **Anna Mihhalevski**. Rye Sourdough Fermentation and Bread Stability. 2012.
143. **Liisa Arike**. Quantitative Proteomics of *Escherichia coli*: From Relative to Absolute Scale. 2012.
144. **Kairi Otto**. Deposition of In<sub>2</sub>S<sub>3</sub> Thin Films by Chemical Spray Pyrolysis. 2012.
145. **Mari Sepp**. Functions of the Basic Helix-Loop-Helix Transcription Factor TCF4 in Health and Disease. 2012.
146. **Anna Suhhova**. Detection of the Effect of Weak Stressors on Human Resting Electroencephalographic Signal. 2012.

147. **Aram Kazarjan**. Development and Production of Extruded Food and Feed Products Containing Probiotic Microorganisms. 2012.
148. **Rivo Uiboupin**. Application of Remote Sensing Methods for the Investigation of Spatio-Temporal Variability of Sea Surface Temperature and Chlorophyll Fields in the Gulf of Finland. 2013.
149. **Tiina Kriščiunaite**. A Study of Milk Coagulability. 2013.
150. **Tuuli Levandi**. Comparative Study of Cereal Varieties by Analytical Separation Methods and Chemometrics. 2013.
151. **Natalja Kabanova**. Development of a Microcalorimetric Method for the Study of Fermentation Processes. 2013.